

A Dissertation
entitled

Molecular Gas in Galactic Nuclei
and its Role in Supermassive Black Hole Accretion Physics

by
James L. Agostino

Submitted to the Graduate Faculty as partial fulfillment of the requirements for the
Doctor of Philosophy Degree in Physics

Dr. Anne M. Medling, Committee Chair

Dr. Loreto Barcos-Muñoz, Committee Member

Dr. J.D. Smith, Committee Member

Dr. Eli Visbal, Committee Member

Dr. Richard E. Irving, Committee Member

Dr. Daniel Hammel,
College of Graduate Studies

The University of Toledo
May 2025

Copyright 2025, James L. Agostino

This document is copyrighted material. Under copyright law, no parts of this document may be reproduced without the expressed permission of the author.

An Abstract of
Molecular Gas in Galactic Nuclei
and its Role in Supermassive Black Hole Accretion Physics
by
James L. Agostino

Submitted to the Graduate Faculty as partial fulfillment of the requirements for the
Doctor of Philosophy Degree in Physics

The University of Toledo
May 2025

Dedication - work in progress

Acknowledgments

Acknowledgements - work in progress

Contents

Abstract	iii
Acknowledgments	v
Contents	vi
List of Tables	ix
List of Figures	xi
1 Introduction: SMBHs and their Host Galaxies	1
1.1 Galaxies; A Very Brief History	2
1.2 Theoretical and Observational evidence of SMBHs	3
1.3 The Role of Supermassive Black Holes in Galaxy Evolution	5
1.3.1 Black Hole Scaling Relations	5
1.3.2 Observations of AGN fueling and feedback	5
1.3.3 Theoretical models of AGN fueling and feedback	9
1.4 Thesis outline	10
2 Constraining Nuclear Molecular Gas Content with High-resolution CO Imaging of GOALS Galaxies	12
2.1 Introduction	12
2.2 Measurements and Imaging	16
2.3 Morphology	19

2.3.1	III Zw 035	19
2.3.2	IRAS F01364-1042	21
2.4	Computing Nuclear Gas Mass	22
2.4.1	Gas mass via CO(2-1)	22
2.4.2	Gas mass via dust continuum	25
2.4.3	Spectral index mapping	30
2.5	Independent enclosed mass measurements	34
2.5.1	Tilted ring modeling	34
2.5.2	Comparison to warm gas M_{enc}	35
2.6	Discussion	37
2.6.1	Black hole masses in context	37
2.6.2	Uncertain Dust Temperature	38
2.6.3	Implications for physics in nuclei of gas-rich mergers	39
2.7	Conclusions	41
3	Direct Tests of Black Hole Accretion Rate Prescriptions: I. Bondi Accretion at Different Scales	43
3.1	Introduction	43
3.2	Nuclear structure of NGC 1068	50
3.3	NGC 1068 observations	52
3.3.1	Keck/OSIRIS K-band Integral Field Spectroscopy	53
3.3.2	ALMA Band 6 Long-baseline Interferometry	54
3.4	Prescription parameters	55
3.4.1	Parameter 1: black hole mass	55
3.4.2	Parameter 2: gas density	56
3.4.2.1	Choice of volume element	56
3.4.2.2	Cold gas mass	57

3.4.2.3	Warm H ₂ gas mass	59
3.4.3	Parameter 3: sound speed of the gas	61
3.4.3.1	CO-derived c _s	61
3.4.3.2	H ₂ -derived c _s	62
3.5	Results: \dot{M}_{Bondi} vs. $\dot{M}_{\text{X-ray}}$	64
3.5.1	Calculating \dot{M}_{Bondi}	64
3.5.2	Calculating X-ray accretion rates	64
3.6	Discussion: results in the context of simulations	67
3.7	Conclusions	69
4	Summary & Future Expansion of Tests of Black Hole Accretion Rate Prescriptions	71
4.1	Nuclear Molecular Gas Content in LIRGs	71
4.2	Direct Tests of Black Hole Accretion Rate Prescriptions	72
4.3	Future Expansion of Direct Tests of Black Hole Accretion Rate Prescriptions	73
A	Considerations for radio imaging	96
B	Kinematic Modeling	99

List of Tables

2.1 Galaxy and observational properties of III Zw 035 and IRAS F01364–1042	18
2.2 Summary of results for mass estimates via CO (α_{CO} method) and continuum. Percentages displayed are relative to the kinematically-derived enclosed masses found in Medling et al. (2015) and are computed as $M_{\text{gas}}/M_{\text{enc}}$. For III Zw 035 we compare to enclosed masses from stellar kinematics and in IRAS F01364–1042 we compare to enclosed masses from gas kinematics. *III Zw 035 gas-based dynamical masses exist in Medling et al. (2015), but we do not use them for comparison in this work due to likely contamination from a molecular outflow. (1): Enclosed masses from Medling et al. (2015). (2): Gas mass from CO(2-1) flux as calculated in Section 2.4.1. (3): Gas mass from continuum flux as calculated in Section 2.4.2.	29
2.3 Summary of results for mass estimates via CO (α_{CO} method) and continuum when subtracted from enclosed masses calculated in this work (see Section 2.5). Percentages displayed are relative to those enclosed masses and are calculated as $M_{\text{gas}}/M_{\text{enc}}$. All values in this table are measured at a radius equal to the beam size of the respective CO data. (1): Enclosed masses derived using CO(2-1) kinematics in Section 2.5. (2): Gas mass from CO(2-1) flux as calculated in Section 2.4.1. (3): Gas mass from continuum flux as calculated in Section 2.4.2.	32

3.1 X-ray and estimated Bondi accretion rates onto the SMBH of NGC 1068 at various radii	67
B.1 ^{3D} Barolo phase two best fit tilted ring model parameters for III Zw 035 and IRAS F01364–1042. The velocity dispersion modeling (column 4) should be taken with caution because of the likely dominance of it by the outflows in these galactic nuclei. The second and third columns, tilted ring radius and rotational velocity, are used to compute enclosed masses as found in Section 2.5.	100

List of Figures

1-1	M - σ relation; Fig. 1 from McConnell & Ma (2013a)	6
2-1	I-Band and ALMA images of III Zw 035 and IRAS F01364–1042	19
2-2	CO(2-1) Moment 0 and 1 maps of III Zw 035 and IRAS F01364–1042 . .	20
2-3	Integrated fluxes and masses for IRAS F01364–1042 and III Zw 035 . .	28
2-4	Spectral index maps for III Zw 035 and IRAS F01364–1042	31
2-5	Position-velocity diagrams of the CO emission in III Zw 035 and IRAS F01364–1042 with enclosed masses calculated using these rotation curves	33
2-6	Comparison of Medling et al. (2015) enclosed masses versus enclosed masses found in this work for III Zw 035 and IRAS F01364–1042	36
3-1	NGC 1068 morphology in CO(2-1), K-band continuum, and H ₂	54
3-2	Converting CO(2-1) flux in NGC 1068 to integrated molecular gas mass .	58
3-3	Method of deriving H ₂ temperature for NGC 1068 as a function of radius	63
3-4	X-ray and Bondi accretion rates as a function of radius, plotted against each other	65
A-1	Effects of different imaging strategies	98
B-1	Kinematic modeling for III Zw 035.	101
B-2	Kinematic modeling for IRAS F01364–1042.	102

Chapter 1

Introduction: SMBHs and their Host Galaxies

The existence of supermassive black holes (SMBHs) in the center of galaxies, including our Milky Way, is ubiquitous. SMBHs are the most massive single objects in our Universe, containing millions or billions times the mass of our Sun. Despite their mass, compared to the size scale of the baryon distribution in galaxies (on order $1\sim 10$ *kpc*), their gravitational influence is on small scales (on order $1\sim 100$ pc). Why then, have astronomers found that the mass of a galaxy's SMBH correlates closely with its global properties? These correlations are the so-called black hole mass scaling relations, and they point towards a physical connection between SMBHs and properties outside their radius of gravitational influence. The leading theory for the cause of this connection is the energy expelled by a SMBH's accretion disk as it is actively growing, a phenomenon referred to as active galactic nucleus (AGN) feedback. The mechanism and magnitude of AGN feedback is driven by the rate of mass accretion onto the SMBH.

Large-scale cosmological simulations have started to implement AGN feedback into their models of galaxy evolution. In these Mpc-scale simulations, the accretion rate onto the SMBH at $<<1$ pc cannot be directly calculated, and so theorists

use “sub-grid” prescriptions as proxies below the gridded resolution of their simulations. Unfortunately, there is no unified sub-grid accretion prescription, and each method produces different accretion rates. This thesis explores the connection between SMBHs and their host galaxies by examining the nuclear gas content around SMBHs and directly testing prescriptions for sub-grid SMBH accretion physics.

1.1 Galaxies; A Very Brief History

Galaxies are the mass hubs of our Universe. These kiloparsec (kpc) scale objects host dark matter, supermassive black holes at their centers, interstellar gas and dust, stars and their remnants (like white dwarfs, neutron stars, and stellar mass black holes), and planets like our Earth. Even though we live in the Milky Way, humans have not known about galaxies for very long. Philosophers and poets had mused about the nature of the Milky Way, and later the Andromeda galaxy, since the 9th century BCE (in terms of written history; in the Babylonian epic poem *Enūma Eliš*). Despite Andromeda and the Magellanic clouds (dwarf galaxies) catching our eyes for millennia, it was not until less than 100 years ago that Edwin Hubble (Hubble 1929) measured the distance to the Andromeda using Cepheid variables stars as standard candles, confirming that it is distinct from the Milky Way.

Since then, alongside technological advancements like the charge-coupled device (CCD) camera, astronomers have learned a great deal about galaxies and their place in the Universe. Part of that picture is that galaxies have different morphologies that can be categorized (Hubble 1926), and that those morphologies are dependent on their evolution, which depends on a number of factors like the environment around the galaxy and in-situ processes like star formation. These galaxy properties are directly observable, but other constituents of galaxies like dark matter (Rubin & Ford 1970) and black holes currently require indirect evidence to confirm their existence.

The gaseous nuclear environment ($r < 500$ pc) around the black holes at the centers of galaxies, SMBHs, is the primary focus of this thesis. This gas plays a major role in the interplay between SMBHs and the global contents of their host galaxies.

1.2 Theoretical and Observational evidence of SMBHs

Black holes are compact objects with such high masses that their gravity prevents light and baryonic matter from escaping their event horizons. Before indirect evidence of their existence was observed, BHs were theorized mathematically as a consequence of Einstein’s theory of general relativity (Einstein 1916). In Subrahmanyan Chandrasekhar’s work using special relativity, he found that a non-rotating object would collapse under its own gravity (e.g. for a white dwarf at $0.91 M_{\odot}$; Chandrasekhar 1931). Later, the Schwarzschild radius (the distance at which certain terms in Einstein’s equations become infinite; Schwarzschild 1916) was described as an event horizon – the radius from which nothing can escape a SMBH’s gravity (Finkelstein 1958). These mathematical theories were then supported by Jocelyn Bell Burnell’s discovery of the pulsar, a rotating neutron star whose radio emission is observable (Bell Burnell 1969). The existence of neutron stars showed that the collapse predicted by Chandrasekhar exists in nature.

Unlike pulsars, black holes and their supermassive counterparts are not directly observable. The first observational hints of SMBHs being real objects came soon after Einstein’s theory of general relativity with observations of M87 by Curtis (1918) at Lick Observatory. He noted the effects of a kpc-scale jet, calling it a “curious straight ray”. This “ray” originates in the center of M87, and we now know it is a relativistic radio jet powered by the central AGN. In Greenstein & Schmidt (1964), the authors report on the “quasi-stellar” (later named quasar) object 3C 273. They connected the large-scale radio jet driven by 3C 273’s quasar to an approximate volume from which

the bright central source was emitting. Through estimates of the electron density and emission lines of ionized gas, they found “...a mass of $6 \times 10^6 M_\odot$ within a radius of about 1 pc.” In Sargent et al. (1978), the authors found that in M87, the kinematics of gas inside a radius ≈ 110 pc “[implies] that M87 contains a central, dark mass of about $5 \times 10^9 M_\odot$ ”, which they then say “markedly implies to us that the presence of a central, supermassive black hole must be a serious possibility.”

Independent teams of researchers later studied orbits of the stars around Sgr A*, the Milky Way’s SMBH (Ghez et al. 2000; Eckart et al. 2002; Schödel et al. 2002; Ghez et al. 2003). They found that the orbits imply a SMBH mass of $\sim 4 \times 10^6$ inside 125 AU (6×10^{-4} pc). These orbits have since been studied for decades (Ghez et al. 2008; Gillessen et al. 2009), and their precision has improved following the advent of adaptive optics, an augment to telescopes that improves spatial resolution by correcting for the atmospheric disturbance of light. Further evidence for the existence of black holes came in the form of gravitational waves, which were predicted by general relativity. The predicted signal for a binary black hole merger inspiral and subsequent coalescence was detected by the Laser Interferometer Gravitational-Wave Observatory (Abbott et al. 2016). Most recently, the gas around both M87’s SMBH and Sgr A* was directly observed using very long baseline interferometry (VLBI), an observing technique that combines observations from around the world (Event Horizon Telescope Collaboration et al. 2019; Event Horizon Telescope Collaboration et al. 2022). Overwhelming evidence points towards the mathematical prediction of SMBHs being real objects in nature, but how do these objects fit into the story of galaxy evolution?

1.3 The Role of Supermassive Black Holes in Galaxy Evolution

Even though SMBHs are, as the name suggests, super massive ($\sim 10^6 - 10^{10} M_\odot$), their gravitational spheres of influence are on \sim 1-100 pc scales, smaller than the kpc scales of galactic disks. It comes as a surprise then, that astronomers have found an apparent connection between SMBHs and their global galaxy properties.

1.3.1 Black Hole Scaling Relations

The inferred connection between SMBH mass and global galaxy properties arises from comparing well-constrained observations of both. Some of the most well-studied relationships, called black hole mass scaling relations, plot black hole mass as a function of bulge luminosity (Kormendy 1993; Ho 1999; Marconi & Hunt 2003; McConnell & Ma 2013a), stellar mass (Silk & Rees 1998; Magorrian et al. 1998; Kormendy & Gebhardt 2001; McLure & Dunlop 2002; Häring & Rix 2004; Bennert et al. 2011; Cisternas et al. 2011a), and stellar velocity dispersion (Gebhardt et al. 2000; Merritt & Ferrarese 2001; Tremaine et al. 2002; Gültekin et al. 2009; Beifiori et al. 2012; McConnell & Ma 2013a, see Figure 1-1) (see Kormendy & Ho 2013 for a review). All of these studies show remarkably small scatter around their lines of best-fit. The question is, then: what is the physical driver of these relationships?

1.3.2 Observations of AGN fueling and feedback

AGN, which have been observed injecting energy into the interstellar medium (ISM) and even the circumgalactic medium (CGM) since more than a century ago (e.g. Curtis 1918 for M87), are a natural suspect for the physical connection between black hole mass (M_{BH}) and global galaxy properties found in black hole scaling rela-

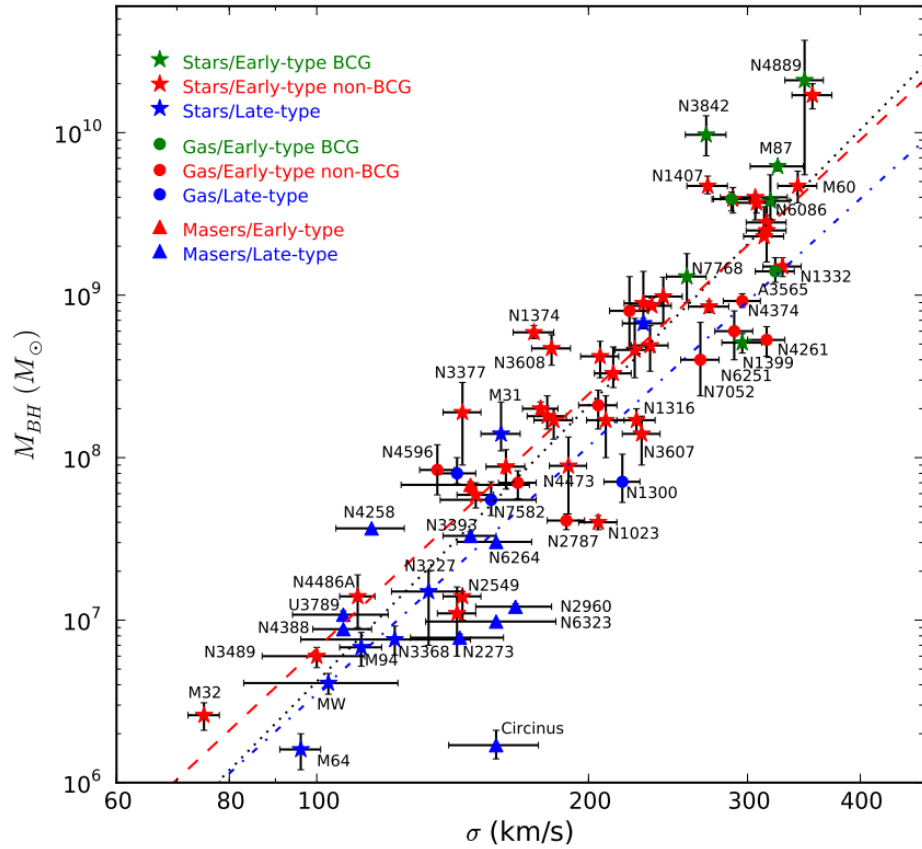


Figure 1-1 Correlation between black hole mass and stellar velocity dispersion (commonly referred to as the $M - \sigma$ relation), Figure 1 in McConnell & Ma (2013a). BH scaling relations like this imply a physical connection between the evolution of SMBH mass and global galaxy properties.

tions. AGNs apparent interactions with the ISM could limit star formation, which in turn would change global properties of the galaxies over time. Constraining exactly how AGN feedback affects galaxy evolution is important to accurately modeling that evolution, but doing so is observationally challenging due to the different size scales of galactic nuclei and disks.

Before black holes can grow via their accretion disks, some physical mechanism may occur to kickstart the inflows from the ISM that fuel the accretion disk. One option, as described in Hopkins et al. (2006), is that gas-rich mergers, often observed in the local universe as luminous or ultra-luminous infrared galaxies (LIRGs and ULIRGS; which have infrared luminosities $L_{\text{IR}} > 10^{11}$ and $10^{12} L_{\odot}$ respectively; Sanders & Mirabel 1996), drive gravitational torques to their shared center of gravity. The gravitational torques feed gas into the merged galaxy bulge, then the gas in the bulge falls onto the SMBH accretion disk. In support of this theory, many studies of galaxies that host AGN also find a higher incidence of a merger event (e.g. Koss et al. 2010, Ellison et al. 2011; Comerford et al. 2015; Ricci et al. 2017a; Goulding et al. 2018; Ellison et al. 2019). Others do not see this increase, a finding that supports growth modeled through more secular processes (e.g. Cisternas et al. 2011b; Kocevski et al. 2012; Schawinski et al. 2012; Villforth et al. 2014). Though these results contradict each other, they are consistent with a SMBH growth model where mergers drive the highest rates of accretion, and lower mass BHs and/or lower accretion rate AGN grow through secular processes like bar and disk instabilities (Hopkins & Quataert 2010; Hopkins & Quataert 2011; Goulding et al. 2018).

When any of these processes cause inflows of interstellar gas to fall into the galactic nucleus, that gas is accelerated to speeds of up to $> 0.1c$ in the accretion disk around a SMBH, and the disk can power radiative outflows. Observationally, AGN feedback can be classified as two mechanisms: radiative (quasar mode) or kinetic (radio mode) (Fabian 2012). In the quasar mode, occurring when the SMBH accretes mass quickly,

photons from the accretion disk couple to the ISM and transfer momentum in a powerful jet. In radio mode, accretion on to the disk is slower, and the primary feedback mechanism is in the form of collimated radio jets that appear narrower than quasar-mode jets. The effect of AGN-driven outflows on star formation, a critical component of galaxy evolution, is also often split into two categories: positive and negative feedback. Positive feedback describes when pressure induced by an AGN outflow enhances star formation. In this case, which is more common in higher redshift galaxies, “jets and or winds [driven by the AGN] flow back onto gas-rich disks”, fueling star formation (Fabian 2012; Silk 2013). Negative feedback describes when the AGN outflow disrupts (quenches) ongoing star-forming regions of the ISM. The quasar mode is thought to start the quenching process, then a radio-mode phase follows and maintains the quenched state (see Fabian 2012 and Morganti 2017 for reviews).

Extended emission of outflows originating from AGN have long been observed in radio wavelengths (e.g. Burns et al. 1983 in Cen. A; Cheung et al. 2016 in a quiescent galaxy; Baron et al. 2018 in a post-starburst galaxy). Molecular gas outflows, which transport the primary fuel for star formation, require more sensitive instruments to be detected because their emission is of lower energy. In Mrk 231, Feruglio et al. (2010) found an AGN-driven outflow that is depleting its molecular ISM in regions ~ 1 kpc in distance from the AGN at rates of $\sim 700 \text{ M}_\odot \text{ yr}^{-1}$. In a sample of mostly ULIRGs and quasar hosts, Veilleux et al. (2013) studied the kinematics and opening angle of AGN-driven molecular outflows. In another sample of local ULIRGs and quasar hosts, Cicone et al. (2014) found molecular outflows in four of their seven sources, and “measured outflow rates of several $100 \text{ M}_\odot \text{ yr}^{-1}$ ”. Fluetsch et al. (2019) studied 45 local star-forming and AGN-host galaxies and found an empirical function that closely relates outflow rate to star formation rate, AGN luminosity, and galaxy stellar mass (simultaneously). In NGC 1068, the galaxy of interest in Chapter 3,

its multiphase outflow has also been well-documented (e.g. Wilson & Ulvestad 1983; Müller-Sánchez et al. 2011; García-Burillo et al. 2014; Saito et al. 2022; Hviding et al. 2023; Holden & Tadhunter 2023; Gallimore & Impellizzeri 2023; Mutie et al. 2024; Hagiwara et al. 2024). Theorists, informed by observations like these, also attempt to model fueling and feedback of SMBH/AGN.

1.3.3 Theoretical models of AGN fueling and feedback

Observations of the direct and indirect influence of AGN feedback on their host galaxies have prompted theorists to include fueling and feedback within their simulations of galaxy evolution. Theorists estimate the impact of feedback on scales from kpc to sub-pc, studying topics like directionality of AGN-driven winds (Williamson et al. 2020), ISM/jet interaction (Meenakshi et al. 2022), and sub-pc scale dusty outflows (Wada et al. 2023) to name a few (see Section 3.1 for more details).

Large scale cosmological simulations that model galaxy evolution are used to survey estimated populations of a researcher’s choice. These simulation suites are becoming more and more commonly used as a comparison to real galaxy samples. They have large volumes, on order $(100 h^{-1} \text{ Mpc})^3$. The foremost limiting factor of these simulation suites with regards to SMBH accretion and feedback is that, because they are so large in size, the physics occurring on small scales cannot be resolved (typically under $\sim 100 \text{ pc}$, depending on the simulation) with current computing resources. For scales smaller than the gridded resolution of the simulation, pre-determined prescriptions must be applied. These prescriptions are commonly referred to as “sub-grid” prescriptions.

SMBH accretion and AGN feedback in large scale cosmological simulations are typically modeled using sub-grid prescriptions. Simulated feedback is dictated by SMBH accretion rate (\dot{M}_{BH}). Energy output by the AGN is coupled to nearby gas particles at a set efficiency, then the particles must cool before participating in star

formation (Vogelsberger et al. 2013 and references therein; Tremmel et al. 2017; Weinberger et al. 2018). Feedback prescriptions are not unified from study-to-study because parameters like the coupling efficiency of energy output by the AGN to the ISM is not well constrained observationally.

For simulated accretion, which is the focus of Chapter 3, the size scales of accretion are so small ($<< 1$ pc) that none of the physics are analytically calculated in large-scale cosmological simulations. For the same reason, like with feedback, different simulations apply different accretion prescriptions, whose accretion rates can vary by orders of magnitude (e.g. Hopkins et al. 2016). Broadly, accretion rates are estimated by assigning particles nearby enough to the SMBH a mechanism for accretion. Simulated accretion rates depend on factors like the distance from the SMBH and the radiative environment within the simulated timestep. Examples of modern large-scale cosmological simulation suites that apply sub-grid accretion prescriptions are described in detail within Section 3.1. Because SMBH accretion is the primary driver of AGN feedback, modeling accretion is critical.

Without a unified method of prescribing SMBH accretion on sub-grid scales in simulations, theorists cannot (in a robust manner) estimate AGN feedback. This puts into question the true state of gas and dust in the simulated ISM which are both crucial pieces of the galaxy evolution picture.

1.4 Thesis outline

The remainder of this thesis is organized as follows. In Chapter 2 we measure the nuclear molecular gas content as a function of radius inside two LIRG merger systems: III Zw 035 and IRAS F01364–1042. The black holes in these systems were shown to potentially be overmassive in Medling et al. (2015) with respect to scaling relations,

which if true, would challenge canonical avenues of black hole growth. We measure how much of the kinematically-derived Medling et al. (2015) mass measurements can be attributed to molecular gas rather than the SMBH and independently measure enclosed mass for comparison. In Chapter 3, we present a pilot study for directly testing black hole accretion rate prescriptions. We describe how we directly measure parameters for a popular SMBH accretion prescription at different aperture radii around the SMBH. We then plug those parameters into the accretion prescription, obtaining a radially-sampled estimate of accretion rate. Additionally, we estimate accretion rate using hard X-rays, then compare the two to test the prescription’s performance as a function of radius. Chapter 4 summarizes the contents of Chapters 2 and 3, then describes the prospects for the future expansion of direct tests of black hole accretion rate prescriptions. Finally, Appendix A makes recommendations for the reduction of high resolution radio data observed via long baseline interferometry.

Chapter 2

Constraining Nuclear Molecular Gas Content with High-resolution CO Imaging of GOALS Galaxies

2.1 Introduction

Every massive galaxy in our universe is thought to host a supermassive black hole (SMBH) in its center. These SMBHs typically contain masses millions or billions times the mass of our Sun. Their gravitational sphere of influence is tiny (of order \sim 1-100 pc, the radius of which can be defined as $r_{\text{SOI}} = GM_{\text{BH}}/\sigma_*^2$; see Yoon 2017) when compared to the typical kpc to hundreds of kpc scale sizes of galaxies. Despite this, a number of galaxy-wide properties correlate with the mass of the central SMBH. These are the so-called black hole mass scaling relations, where SMBH mass scales with host galaxy properties like bulge luminosity (Kormendy 1993; Ho 1999; Marconi & Hunt 2003; McConnell & Ma 2013a), stellar mass (Silk & Rees 1998; Magorrian et al. 1998; Kormendy & Gebhardt 2001; McLure & Dunlop 2002; Häring & Rix 2004; Bennert et al. 2011; Cisternas et al. 2011a), and stellar velocity dispersion (Gebhardt et al. 2000; Merritt & Ferrarese 2001; Tremaine et al. 2002; Gültekin et al. 2009;

Beifiori et al. 2012; McConnell & Ma 2013a). The mechanism driving these relations is not well understood and the search for a physically-motivated picture for the co-evolution is an active area of research (see Kormendy & Ho 2013 and Heckman & Best 2014 for reviews and Bennert et al. 2021 for a recent study on local galaxies).

One of the major uncertainties in placing galaxies on the SMBH-galaxy scaling relations is a precise measurement of the mass of the black hole. Even with very-long-baseline interferometry, the region near the event horizon can only be directly “observed” around the nearest, most massive SMBHs (Event Horizon Telescope Collaboration et al. 2019).

Depending on the target and data available, multiple approaches can be taken to tackle this task. The central point mass can be inferred by high-resolution kinematic maps of stars and/or gas where Keplerian rotation dominates. Reverberation mapping (Clavel et al. 1991; Horne et al. 2004; Vestergaard & Peterson 2006a; Cackett et al. 2021) utilizes emission of broad line region (BLR) gas that is excited by continuum radiation emanating from the accretion disk of the active galactic nucleus (AGN) accretion disk. The time delay between the accretion disk and the BLR, along with the virial theorem, can be used to infer a mass enclosed. Schwarzschild modeling (Schwarzschild 1979) takes observables like the luminosity and line of sight velocity distributions and matches a theoretical distribution of matter to what is seen (Faber & Jackson 1976; Lauer et al. 1995; Kormendy et al. 1997; Cretton et al. 1999; Gebhardt et al. 2000; van den Bosch et al. 2008; Walsh et al. 2012). Direct measurements of stellar orbits has been used to precisely measure the black hole mass at the center of the Milky Way (Ghez et al. 2008, Genzel et al. 2010). With next generation telescopes (>20 m class) that utilize adaptive optics and high resolution spectroscopy, those precise measurements will extend to the distance of the Virgo cluster (Do et al. 2014). Various kinds of dynamical modeling of stars and gas on the circumnuclear disk (>1 pc) or slightly larger scale can be used to determine black hole mass (Cappellari 2008,

Barth et al. 2009, Medling et al. 2011, U et al. 2013, Medling et al. 2014). Empirically-calibrated proxies such as the luminosity of H β , 5100Å continuum, the CIV line dispersion, accretion disk size, and other optical/UV tracers that are correlated with M_{BH} can be used in single-epoch studies (e.g. Vestergaard & Peterson 2006b; Morgan et al. 2010; Bentz et al. 2013; U et al. 2022). These relationships do not require complex, dedicated observations and are rooted in black hole mass scaling relations.

In this Chapter, we refer to a parent sample of nine SMBH $M_{\text{enclosed}} \leq 77$ mas masses within gas rich mergers derived via gas and stellar kinematics in Medling et al. (2015). These enclosed mass measurements use data from Keck/OSIRIS adaptive optics (AO) and target galaxies from the Great Observatory All-sky LIRG Survey (GOALS, Armus et al. 2009). In the K-band, these data use the CO (2-0) and (3-1) bandheads to trace kinematics of young stars along with emission from Br γ and H₂. LIRGs (luminous infrared galaxies) emit an excess of light in the infrared ($L_{IR} > 10^{11}$ L $_{\odot}$ by definition; Sanders & Mirabel, 1996) powered by vigorous activity from either star formation or AGN, or both. Based on dynamical (enclosed mass) measurements from Medling et al. (2015), the masses of these nine SMBHs lie above canonical black hole mass scaling relations: supermassive black hole mass (M_{BH}) vs. stellar velocity dispersion (σ_{\star}), total stellar mass (M $_{\star}$), and bulge luminosity (L_{H,bulge}). Non-LIRG spiral galaxies do not typically lie above scaling relations (Davis et al. 2018; Davis et al. 2019), and whether most LIRGs do remains in question. Overmassive black holes present a challenge to the canonical understanding of gas-rich mergers, which predicts that these black holes will grow more in an upcoming quasar phase — placing them in even greater conflict with scaling relations (Mirabel & Sanders 1988; Hopkins et al. 2008b; Hopkins et al. 2008a).

The results from Medling et al. (2015) were surprising but came with a caveat: the resolution of the Keck/OSIRIS+AO data does not probe all the way down to the SMBH event horizon. Those dynamically-derived SMBH mass measurements in

Medling et al. (2015) are a mass enclosed within the FWHM of the data, 77 mas, meaning they could include extended mass. This Chapter is focused on quantifying exactly how much molecular gas mass exists within that limit, then completing an independent enclosed mass measurement for comparison. Medling et al. (2019) performed a pilot study focused on measuring molecular gas mass in one of these galaxies that host double nuclei, NGC 6240. Using Atacama Millimeter/submillimeter Array (ALMA) Band 6 CO($J=2-1$) and continuum data to measure molecular gas mass, they found that in the northern nucleus, the black hole shifts down to scaling relations after the gas mass correction, as up to 89% of the previously measured enclosed mass could be attributed to gas rather than the black hole. In contrast, the dynamical mass of the southern nucleus consists of up to only 11% gas mass, leaving it above scaling relations. The following work estimates the amount of molecular gas mass in two other gas-rich, merging LIRGs with the purpose of understanding whether or not these galaxies host overmassive black holes. Such confirmation would be further evidence for an accretion paradigm in which the SMBH grows before the global galaxy properties in scaling relations, which is contrary to the timeline of accretion in typical systems (Hopkins 2012; Cen 2012; Anglés-Alcázar et al. 2017).

In this Chapter we determine whether the amount of gas present within the resolving limit of the original dynamical mass measurements accounts for the observed disagreement with scaling relations. We then measure an independent enclosed mass using the CO(2-1) kinematics. This Chapter is structured as follows. Section 2.2 details the CO(2-1) measurements obtained from the ALMA and how the imaging process of these measurements was conducted. Section 2.4 explains how we calculated molecular gas mass estimates via both CO(2-1) and ALMA Band 6 continuum. Section 2.5 describes independent enclosed mass measurements using the same CO(2-1) cubes and how they compare to the Medling et al. (2015) enclosed masses. Section 2.6 contextualizes these results within the picture of scaling relations and what those re-

sults mean for our current picture of the co-evolution of merging gas-rich galaxies and their SMBHs.

The two galaxy merger systems featured in this Chapter are III Zw 035 and IRAS F01364–1042. III Zw 035 is at $z = 0.02744$ and R.A. = 01h44m30.50 s, dec. = +17d06m05.0 s with a total infrared luminosity $\log(L_{\text{IR}}/L_{\odot}) = 11.64$. IRAS F01364–1042 is at $z = 0.04823$ and R.A. = 01h38m52.921 s, dec. = -10d27m11.42 s with a total infrared luminosity $\log(L_{\text{IR}}/L_{\odot}) = 11.85$ (Armus et al. 2009). Infrared luminosities of these galaxies and others in the GOALS survey can be found in Armus et al. (2009). If III Zw 035 or IRAS F01364–1042 host AGNs, they must be dust-obscured.

In this work, we use cosmological parameters of $H_0 = 70 \text{ km s}^{-1} \text{ Mpc}^{-1}$, $\Omega_m = 0.28$, and $\Omega_{\Lambda} = 0.72$ (Hinshaw et al. 2009). To calculate spatial scales and luminosity distances for III Zw 035 and IRAS F01364–1042 we use Ned Wright’s Cosmology Calculator (Wright 2006). III Zw 035 has a scale of $554 \text{ pc arcsec}^{-1}$ and IRAS F01364–1042 has a scale of $1012 \text{ pc arcsec}^{-1}$.

2.2 Measurements and Imaging

The nuclei of III Zw 035 and IRAS F01364–1042 were observed with Keck-OSIRIS+AO in 2010 and 2011 (Medling et al. 2014). This integral field spectroscopy was used to measure dynamical masses at a resolution of 77 mas (Medling et al. 2015). As our science goal is to resolve the inner-most molecular gas in these galactic nuclei, our Band 6 observations were taken in ALMA’s second-most extended configuration, C43-9 (PI Medling, project codes 2018.1.01123.S and 2019.1.00811.S). III Zw 035 was observed on 2019 June 20th for 4178 s (maximum recoverable scale [MRS] = 0.4’’) and IRAS F01364–1042 was observed on 2021 August 30th for 1689 s (MRS = 0.5’’) as well as in the C43-8 configuration on 2021 August 8th for 2541 s (MRS = 0.8’’).

For all measurement sets we follow the standard calibration pipeline and manually examined each measurement set to make sure flagging was complete. Then, for IRAS F01364–1042 we concatenated both measurement sets, checking for any inconsistencies in the relative weightings of each configuration. Compared to only using the configuration 9 measurement set the combined measurement sets give an rms that is a factor of $\sim\sqrt{2}$ lower and improves our signal by approximately the same value because of the increased effective exposure time and uv-sampling of the slightly more compact C43-8 configuration. Next, we imaged the line-free channels to produce continuum maps for each galaxy. This included avoiding not only the CO(2-1) line in both galaxies, but also lines like CS(5-4) and HC₃N which are prominent in the core of III Zw 035. We then perform continuum subtraction in the uv-plane and image the spectral window containing CO, producing a spectral cube for each galaxy. After imaging with Briggs weighting (Briggs 1995; **robust** = −0.5), our achieved synthesized beam resolutions (FWHMs) for the data sets used in our analysis for IRAS F01364–1042 and III Zw 035 respectively, are 41 and 30 mas for the spectral cubes and 29 and 26 mas for the continuum images. All of these data are firmly under the resolution used in the prior dynamical measurements. For III Zw 035, we achieved a root mean square (rms) of 1.11 mJy beam^{−1} in a channel width, Δv , of 10.4 km s^{−1} and a continuum rms of 0.033 mJy beam^{−1} while for IRAS F01364–1042 we achieved a rms of 0.43 mJy beam^{−1} in a channel width, Δv , of 11.2 km s^{−1} and a continuum rms of 0.029 mJy beam^{−1}. Table 2.1 lists relevant properties of these measurement sets and Figure 2-1 shows Hubble I-Band images (GO-10592; PI: Evans) of both of III Zw 035 and IRAS F01364–1042 overlaid with ALMA Band 6 CO(2-1) contours. These contours were made using CO(2-1) imaged at a slightly lower resolution (**robust** = 0.5) than the dataset we use for our analysis.

We use the Common Astronomy Software Applications (*CASA*, CASA Team et al. 2022) package developed by the NRAO, ESO, and NAOJ to do this imaging. `tclean`,

Galaxy	D _L (Mpc)	Merger Stage	Resolution (pc)	Freq. (GHz)	CO Flux (Jy km s ⁻¹)	Cont. Flux (mJy)
III Zw 035	110	Pre-Merger	13.62	224.38	1.617	5.042
IRAS F01364–1042	209.9	Late-Stage	19.23	219.84	8.791	2.796

Table 2.1 List of galaxy and observational properties used in this work. All data were taken in the long baseline ALMA 12m configuration. The frequency column shows the observed CO(2-1) frequencies. The merger stage definitions are from Stierwalt et al. (2013) where pre-merger is defined as galaxies prior to their first encounter and late-stage describes two nuclei in a common envelope (but that still show signs of a merger). Fluxes listed are integrated flux within the 77 mas aperture used throughout this work. Absolute flux uncertainties in ALMA Band 3 and Band 6 data are 5 and 10%, respectively (Cortes et al. 2023).

a routine within *CASA*, takes the measured visibilities and reconstructs a sky model. One of the `tclean` parameters that is part of the Briggs weighting scheme (Briggs 1995), `robust`, adjusts how different parts of the uv-plane (in Fourier space) are weighted. To test the impact of the `robust` parameter on our results, we performed our analysis on a range of values ($-0.5, 0, 0.5, 2$). For our galaxies using a `robust` parameter of -0.5 loses less than 10% of flux to diffuse CO emission compared to the default pipeline value of (0.5) and provides the benefit of producing an image with a narrower beam FWHM.

Achieving the highest available spatial resolution matches our science goal by probing gas mass as close to the black hole as possible and so we chose `robust = -0.5` as our default imaging for the analysis in this paper (both for CO and continuum).

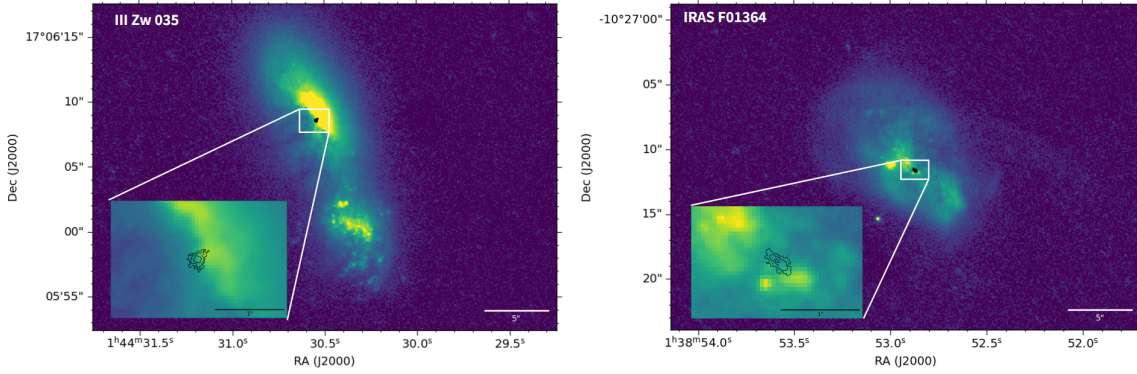


Figure 2-1 I-Band Hubble ACS images (GO-10592; PI: Evans) of III Zw 035 (left) and IRAS F01364–1042 (right) with CO(2-1) moment 0 contours overlaid in black. Moment 0 contours are from $10^{-0.4}$ to $10^{0.5}$ Jy beam $^{-1}$ km s $^{-1}$ for III Zw 035 and $10^{-0.8}$ to $10^{0.5}$ Jy beam $^{-1}$ km s $^{-1}$ for IRAS F01364–1042 in 7 logarithmically-spaced intervals. III Zw 035’s companion galaxy still retains much of its large-scale structure, while in IRAS F01364–1042 the two are in a later stage of the merger process.

2.3 Morphology

2.3.1 III Zw 035

As defined by the merger classification from Stierwalt et al. (2013) in optical wavelengths, III Zw 035 is a pre-merger. This means that this galaxy and its companion have not yet had their first encounter. Figure 2-2 shows ALMA Band 6 CO, and continuum, along with a moment 1 (velocity) map of CO(2-1) for III Zw 035 and IRAS F01364–1042. The high resolution \sim 26 mas molecular gas emission in III Zw 035 reveals a resolved core in CO with a peak integrated intensity that is slightly offset (5-10 pc) from the center of Band 6’s continuum emission (\sim 230 GHz). Continuum contours highlight several resolved clumpy substructures about 20-30 pc away from the central CO source. Previously, Pihlström et al. (2001) found clumps of OH maser and 18 cm continuum emission in similar positions around the central source.

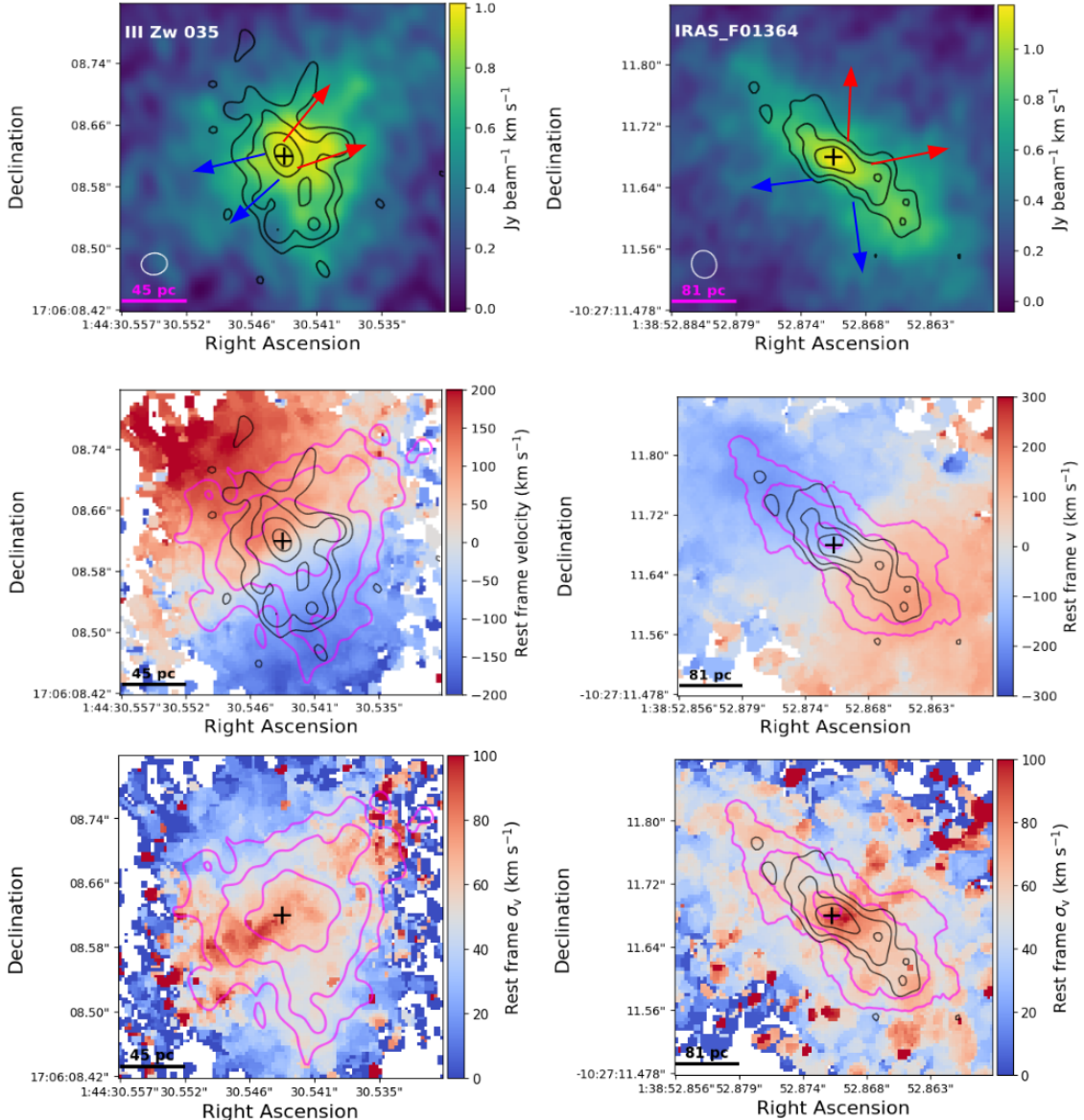


Figure 2-2 *Top:* CO(2-1) moment 0 (integrated intensity) maps for III Zw 035 (left) and IRAS F01364–1042 (right) with Band 6 continuum contours at 230 GHz for III Zw 035 and 228 GHz for IRAS F01364–1042 with levels at 3, 6, 12, 24, 48 × (rms) Jy beam^{-1} (rms values are $32.7 \times$ and $29.4 \times \mu\text{Jy beam}^{-1}$ for III Zw 035 and IRAS F01364–1042 respectively). White ellipses indicate the beam sizes of the CO images (33 x 28 for III Zw 035 and 43 x 40 mas for IRAS F01364–1042). *Middle; Middle:* CO(2-1) moments 1 (velocity) and 2 (velocity dispersion) maps. Black contours are the same as in the top two panels for continuum, while magenta contours are moment 0 contours from $10^{-0.4}$ to $10^{0.5}$ $\text{Jy beam}^{-1} \text{km s}^{-1}$ for III Zw 035 and $10^{-0.8}$ to $10^{0.5}$ $\text{Jy beam}^{-1} \text{km s}^{-1}$ for IRAS F01364–1042 in 7 logarithmically-spaced intervals. Velocity maps for both galaxies are clipped to a 3σ CO(2-1) detection. Continuum center,

Further inspection of the ALMA data cubes in these clumps shows the presence of CS(5-4), a good dense gas tracer (Wang et al. 2011). Moments 0, 1 and 2 of the CS(5-4) distribution can be found in Figure ?? in Appendix ???. The clumpy nature of this dense gas tracer and evidence from previous observations could indicate that there are star-forming clumps around III Zw 035’s core. These clumps may also be part of a forming or otherwise evolving torus or ring around III Zw 035’s nucleus, as distances of the clumps to the core are typical (10s of pc) for these sorts of structures (e.g. García-Burillo et al. 2021). CO(2-1) is not apparent in all of these clumps. Additional matched resolution data at other wavelengths, such as deeper ALMA Band 7 and Band 3 continuum, are necessary to further constrain the nature of this distribution of mass.

The CO moment 1 maps (Figure 2-2, bottom left) show strong disk-like rotation across the major axis of the galaxy, similar to what is seen in H₂ and Br γ (Medling et al. 2014). III Zw 035 also show evidence of a molecular outflow along the minor axis seen in the H₂ and Br γ maps in U et al. (2019), as well as in CO(1-0) at lower resolution in Lutz et al. (2020). III Zw 035’s outflow can also be seen in CO(2-1) and it will be discussed in detail in a future work.

2.3.2 IRAS F01364-1042

Toward the opposite end of the merger spectrum, IRAS F01364–1042 is classified as a late-stage merger in Stierwalt et al. (2013). The two galaxies have their nuclei in the same envelope at the center of the system. As seen in Figure 2-2, compared to III Zw 035, the brightest CO(2-1) emission in IRAS F01364–1042 has an edge-on disk-like morphology that traces the continuum emission well, with a central source that seems to be marginally resolved. Similar to III Zw 035, it shows disk-like rotation in the high-resolution CO(2-1) imaging, with symmetrical velocity gradients on either side of the disk that match well to the H₂ and Pa α maps at \sim 2-3 \times coarser resolution

in Medling et al. (2014). The CO(2-1) data presented in this work show evidence of the presence of an outflow, along the minor axis, originating from the nucleus. This outflow is also supported by MIRI H₂ and ALMA CO(1-0) maps (Song et al in prep.)

2.4 Computing Nuclear Gas Mass

Our goal in this work is to calculate the amount of the nuclear molecular gas mass that falls within the resolution limit of Keck-OSIRIS+AO (~ 77 mas). Following Medling et al. (2019), in this section we describe our two main methods of calculating molecular gas mass. Additionally, we perform independent enclosed mass estimates, for comparison to Medling et al. (2015), through position-velocity (PV) diagrams in Section 2.5. We summarize and comment on the results of these analyses in Section 2.6.

As in Medling et al. (2019), we measure nuclear gas masses to compare with enclosed masses derived from stellar and gas kinematics from Medling et al. (2015). We include these original BH masses for III Zw 035 and IRAS F01364–1042 in the top row of Table 2.2. In this study we do not include comparisons to III Zw 035’s enclosed warm gas mass because of high uncertainties attributed to the H₂ and Br γ outflow seen along its minor axis U et al. (2019). For IRAS F01364–1042, we use the enclosed masses derived via gas kinematics, which could be impacted by the potential outflowing component; however, no stellar dynamics-based mass is available.

2.4.1 Gas mass via CO(2-1)

Although most interstellar gas is in the form of H₂ in LIRG nuclei, its net-zero dipole moment makes it difficult to observe directly in luminous galaxies. Carbon monoxide is often used as a tracer molecule in its place (Solomon et al. 1972; Wilson et al. 1974; Scoville & Solomon 1975; Burton et al. 1975).

To calculate a molecular gas mass from our spectral cube we start with the full, 1.875 (in GHz) wide cube, then, in python, integrate across the channels with CO emission in each pixel. To determine if a channel has CO emission in it, we use a combination of visual inspection of the individual channel maps and integrated spectra in a rectangular region made in *CASA*. This produces a moment 0, or flux map of CO(2-1). Then, to calculate radial, integrated values we step outward in a box shape. Each radial step expands the box in two pixels in each x(± 1) and y(± 1) direction. The same radial stepping method is used in Section 2.4.2. To convert to mass we must first translate the CO line flux to CO line luminosity $L'_{\text{CO}(2-1)}$. For this we apply the equation from Solomon & Vanden Bout (2005):

$$L'_{\text{CO}(2-1)} = (3.25 \times 10^7) S_{\text{CO}} \Delta v (\nu_{\text{obs}}^{-2} D_L^2 (1+z)^{-3}) \text{K km s}^{-1} \text{pc}^2 \quad (2.1)$$

where $f_\nu d\nu$ is the flux of the CO(2-1) emission (Jy km s^{-1}), ν_{obs} is the observed frequency (in GHz), and D_L is the luminosity distance (Mpc).

To convert from this line luminosity to mass we use the conversion factor α_{CO} . This conversion factor varies depending on where it is being applied, and the inclination angle of the galaxy. For example, on >600 pc scales, Sandstrom et al. (2013) find mean $\alpha_{\text{CO}_{(1-0)}}$ values ranging from 2.9 to 8.2. In NGC 3351, using ~ 100 pc resolution ALMA data, Teng et al. (2022) find intensity-weighted values between 1.11 and 1.79 on 2 kpc scale, and find that the conversion factor is lower in inflow regions. Medling et al. (2019) used an $\alpha_{\text{CO}(2-1)}$ conversion factor calibrated spatially by Cicone et al. (2018) for the nuclear regions of NGC 6240. NGC 6240 is a local, merging LIRG like our systems, but it does host X-ray detected AGN and a clear double nucleus, unlike our systems.

In this work, we use the $\alpha_{\text{CO}_{(1-0)}} = 2.3 \pm 1.2$ from Cicone et al. (2018) and scale it to $\alpha_{\text{CO}(2-1)}$ by independently measuring r_{21} ($r_{21} = L'_{\text{CO}(2-1)} / L'_{\text{CO}_{(1-0)}}$) at 100 mas

resolution in both III Zw 035 and IRAS F01364–1042 (57 and 98 pc, respectively). To measure this new r_{21} we created beam-matched images by first smoothing the CO(2-1) data to the CO(1-0) data (project code 2017.1.01235.S; PI: Barcos-Muñoz) by using *CASA*'s **imsSmooth** task, which performs a Fourier-based convolution to the CO(1-0) beam in which we used a Gaussian kernel. We then used the smoothed image to measure the line luminosities in the same 154×154 mas box used in our analysis. The new $\alpha_{\text{CO}(2-1)}$ value for III Zw 035 is calculated as:

$$\alpha_{\text{CO}(2-1)} = \frac{\alpha_{\text{CO}(1-0)}}{r_{21}} = \frac{2.3 \pm 1.2}{0.762 \pm 0.1} = 3.017 \pm 1.23 \text{ M}_\odot (\text{K km s}^{-1} \text{ pc}^2)^{-1}. \quad (2.2)$$

and the same calculations are done for IRAS F01364–1042 which has a $r_{21} = 0.772 \pm 0.09$ and $\alpha_{\text{CO}(2-1)} = 2.98 \pm 1.25 \text{ M}_\odot (\text{K km s}^{-1} \text{ pc}^2)^{-1}$. Uncertainties on r_{21} are attributed to the ALMA Band 3 and 6 flux uncertainties of 5 and 10% respectively (Diaz Trigo et al. 2019). Using these $\alpha_{\text{CO}(2-1)}$ estimates rather than adopting the value from Cicone et al. (2018) increases the final gas (H₂ and helium) masses calculated in III Zw 035 and IRAS F01364–1042 by factors of 1.31 and 1.30, respectively.

The use of low-J CO lines as tracers of molecular gas has been explored for decades; α_{CO} or similar conversion factors have been calibrated for both the Milky Way and other galaxies (e.g. as reviewed by Dickman 1978, Combes 1991, and Bolatto et al. 2013). Montoya Arroyave et al. (2023) measure a median $\alpha_{\text{CO}(1-0)} = 1.7 \pm 0.5 \text{ M}_\odot$ in 37 ULIRGs (ultra-luminous infrared galaxies, $L_{\text{IR}} > 10^{12} \text{ L}_\odot$) and 3 LIRGs (see also Herrero-Illana et al. 2019). Sandstrom et al. (2013) found that in the central kpc of 26 starburst galaxies, $\alpha_{\text{CO}(1-0)}$ is a factor of ~ 2 smaller than in the larger scale disk. Each of these studies found median $\alpha_{\text{CO}(1-0)}$ values lower than the typical global value for the Milky Way ($4.4 \text{ M}_\odot (\text{K km s}^{-1} \text{ pc}^2)^{-1}$; Bolatto et al. 2013). These measurements were done on larger scales than the ones we make our enclosed mass measurements in, but suggest that globally-calibrated $\alpha_{\text{CO}(1-0)}$ values cannot be trusted for analysis

on nuclear scales. The $\alpha_{\text{CO}(2-1)}$ we adopt here is therefore uncertain particularly compared to larger scale estimates of $\alpha_{\text{CO}(1-0)}$, because of the lack of studies which robustly calibrate these nuclear conversion factors on < 50 pc scales in LIRGs. In this work we attempt to mitigate for these uncertainties by using the highest resolution calibrated $\alpha_{\text{CO}(1-0)}$ from Cicone et al. (2018) for NGC 6240, a merging (U)LIRG.

The $\alpha_{\text{CO}(2-1)}$ we adopt here is therefore uncertain, particularly compared to larger scale estimates of $\alpha_{\text{CO}(1-0)}$. Sandstrom et al. (2013) found that in the central kpc of 26 starburst galaxies, $\alpha_{\text{CO}(1-0)}$ is a factor of ~ 2 smaller than in the larger scale disk. Montoya Arroyave et al. (2023) measure a median $\alpha_{\text{CO}(1-0)} = 1.7 \pm 0.5 M_\odot$ in 37 ULIRGs (ultra-luminous infrared galaxies, $L_{\text{IR}} > 10^{12} L_\odot$) and 3 LIRGs (see also Herrero-Illana et al. 2019). These measurements were done on much larger scale than our estimates, but suggest that global $\alpha_{\text{CO}(1-0)}$ values cannot be trusted for analysis on nuclear scales.

The CO(2-1) flux profiles, which are multiplied by $\alpha_{\text{CO}(2-1)}$ to obtain a mass profile, are shown in the top two rows of Figure 2-3. Inside the 77 mas Keck-OSIRIS resolution limit achieved in Medling et al. (2015) we find $(4.23 \pm 2.12) \times 10^7 M_\odot$ of molecular gas mass for III Zw 035 and $(6.68 \pm 3.49) \times 10^8 M_\odot$ of molecular gas mass for IRAS F01364–1042 within 43.7 and 76.9 pc, respectively. Fractionally these values account for between ~ 1 and $\sim 52\%$ (including 1σ errors) of the previously determined enclosed masses (see Table 2.2 for details).

2.4.2 Gas mass via dust continuum

Another way of estimating the central molecular gas mass is by measuring the cospatial dust mass using our mm-wavelength continuum imaging. For LIRGs, the mm/sub-mm continuum flux densities are typically dominated by thermal dust emission (U et al. 2012). Continuum measurements start with the same aperture as in Section 2.4.1 (a 154 x 154 mas square), integrating flux density as the box grows

outward. We then use the calibrated dust continuum flux density ratio to H₂ from Scoville et al. (2016). This calibration improves on the Scoville et al. (2015) relation used for Arp 220, but it assumes a globally-derived, mass weighted dust temperature of 25 K. In the sample of ULIRGs from U et al. (2012), the average global T_D was found to be moderate at \sim 25-45 K. Other recent studies have shown that luminosity-weighted nuclear dust temperatures can be much higher than this (e.g. Sakamoto et al. 2021), and so we explore a range of temperatures from 100-500 K for our primary analysis.

As our continuum-based measurements use a relation that assumes the emission is from dust, for them to be accurate we have to ensure that any contaminants to that emission are removed. Some of the continuum flux density at \sim 230 GHz may be due to synchrotron radiation (**originating from obscured AGN and/or supernova remnants**) and free-free emission (Condon & Ransom (2016)). We can predict the contributions of these phenomena to our continuum flux by utilizing previous observations of our galaxies at lower frequencies where synchrotron and free-free emission dominate the flux, extrapolating their spectra to our frequencies. To estimate the contribution of synchrotron and free-free emission to our measured continuum flux, we use 32.5 GHz integrated fluxes from Very Large array observations found in Barcos-Muñoz et al. (2017). Together with integrated ALMA Band 3 observations (project 2017.1.01235.S, PI Barcos-Muñoz), we can measure the spectral index of both synchrotron and free-free together between 32.5 and \sim 100 GHz, then extrapolate the 100 GHz flux to ALMA Band 6 using that spectral index. For III Zw 035 the spectral index $\alpha = -0.58 \pm 0.04$ and for IRAS F01364–1042 $\alpha = -0.39 \pm 0.04$. Uncertainties are calculated as a combination of image noise and errors in calibration flux uncertainties for ALMA and the VLA (Diaz Trigo et al. 2019; ?).

To estimate the contribution of these contaminants to the Band 6 continuum, we use the \sim 120 mas resolution, 32.5 GHz VLA data from Barcos-Muñoz et al. (2017)

and the spectral indices mentioned prior. We extrapolate the 32.5 GHz integrated flux to a Band 6 flux density value using:

$$f_{\text{extra}} = f_{\text{synch}} + f_{\text{free-free}} = f_{33\text{GHz}} \left(\frac{\nu_{\text{cont}}}{33\text{GHz}} \right)^\alpha \quad (2.3)$$

where ν_{cont} is the center of the continuum band for each galaxy in GHz, and the flux densities (f) are in Jy. The resulting contributions to our continuum flux by both synchrotron and free-free sources are 23% and 34% for III Zw 035 and IRAS F01364–1042 respectively.

These contributions are subtracted in the following equation, which adopts a modified blackbody spectral index $\beta = 1.8$, where we perform our gas mass conversion (Equation 3; Scoville et al. 2015):

$$\frac{0.868 \times (f_{\text{cont}} - f_{\text{extra}}) d_{\text{Mpc}}^2}{(1+z)^{4.8} T_{25} \nu_{350}^{3.8} \Gamma_{RJ} 10^3 \text{Mpc}} 10^{10} M_\odot \quad (2.4)$$

where the fluxes (f_{cont} is continuum flux density) are in mJy, luminosity distance, d , is in Mpc, T is normalized to 25 K, ν normalized to 350 GHz, and Γ_{RJ} is the correction for departure in the rest frame of the Planck function from Rayleigh-Jeans, which varies with temperature (Scoville et al. 2016).

Using two bracketing dust temperature cases, 100 K and 500 K, we find gas masses inside the 77 mas Keck-OSIRIS resolution (box) limit of $(1.00 \pm 4.29) \times 10^8 M_\odot$ to $(5.24 \pm 0.22) \times 10^8 M_\odot$ of mass for III Zw 035 and $(1.21 \pm 0.50) \times 10^8 M_\odot$ to $(6.36 \pm 2.63) \times 10^8 M_\odot$ of mass for IRAS F01364–1042 within 43.7 and 76.9 pc, respectively. Rows 3 and 4 of Figure 2-3 show the continuum flux density and molecular gas masses as a function of radius. Fractionally, in relation to the previously determined enclosed masses from Medling et al. (2015), these measured values account for as little as $\sim 5\%$ in the high dust temperature case to as much as $\sim 77\%$ in the low temperature case (see Table 2.2 for details). This wide range of gas masses and the

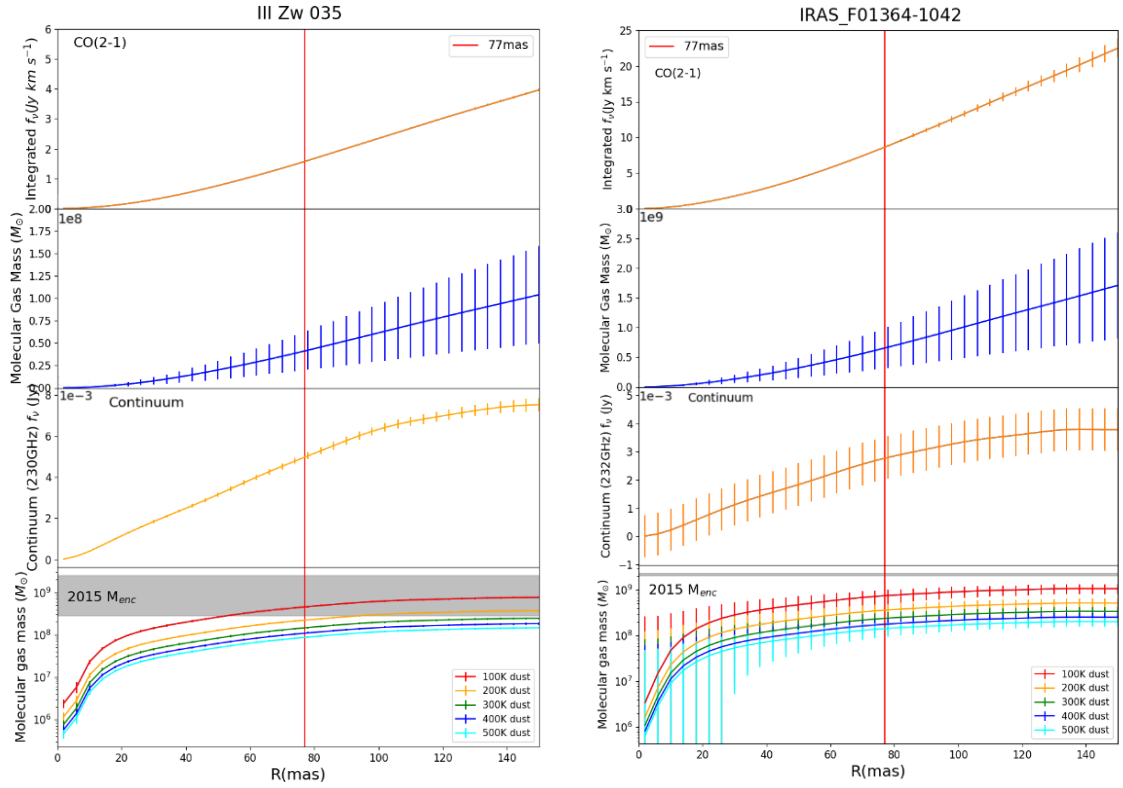


Figure 2-3 Integrated measurements and calculated masses within the boxed aperture for IRAS F01364–1042 and III Zw 035. *First row:* enclosed CO(2-1) flux from images described in Section 2.2. *Second row:* enclosed mass calculated from CO(2-1) fluxes shown in above panels using method described in Section 2.4.1. *Third row:* integrated continuum flux densities at 230 GHz (III Zw 035) and 228 GHz (IRAS F01364–1042) extracted from images described in Section 2.2. *Bottom row:* enclosed mass calculated from continuum fluxes shown in above panels using method described in Section 2.4.2. Grey regions are Medling et al. (2015) enclosed mass ranges. III Zw 035 requires a dust temperature above ~ 175 K to have a dust-derived gas mass lower than the previous enclosed mass while IRAS F01364–1042 requires a dust temperature of > 48 K.

Integrated gas masses compared to previous enclosed mass measurements

	III Zw 035	IRAS F01364–1042
Gas (H_2 , Br γ)	*	$(2.24^{+0.06}_{-0.17}) \times 10^9 M_{\odot}$
⁽¹⁾ M_{enc}	Stellar (disk) $(>6.80^{+1.10}_{-4.0}) \times 10^8 M_{\odot}$	-
	Stellar (JAM) $(<2.00^{+0.50}_{-0.70}) \times 10^9 M_{\odot}$	-
⁽²⁾ $M_{\text{gas,CO}}$	$(4.23 \pm 2.21) \times 10^7 M_{\odot}$	$(6.68 \pm 3.49) \times 10^8 M_{\odot}$
⁽⁴⁾ Gas fraction	$<6.22^{+1.7\%}_{-1.1\%}$ $>2.11^{+1.2\%}_{-1.3\%}$	$29.8^{+22.1\%}_{-22.2\%}$
⁽³⁾ $M_{\text{gas,cont}(100\text{K})}$	$(5.24 \pm 0.22) \times 10^8 M_{\odot}$	$(6.36 \pm 2.63) \times 10^8 M_{\odot}$
⁽⁴⁾ Gas fraction	$>26.2^{+9.2\%}_{-6.6\%}$ $<77.1^{+45.4\%}_{-3.4\%}$	$28.3^{+11.7\%}_{-11.9\%}$
⁽³⁾ $M_{\text{gas,cont}(500\text{K})}$	$(1.00 \pm 4.29) \times 10^8 M_{\odot}$	$(1.21 \pm 0.50) \times 10^8 M_{\odot}$
⁽⁴⁾ Gas fraction	$>5.0^{+1.3\%}_{-1.8\%}$ $<14.7^{+8.7\%}_{-0.7\%}$	$5.4^{+1.7\%}_{-1.2\%}$

Table 2.2 Summary of results for mass estimates via CO (α_{CO} method) and continuum. Percentages displayed are relative to the kinematically-derived enclosed masses found in Medling et al. (2015) and are computed as $M_{\text{gas}}/M_{\text{enc}}$. For III Zw 035 we compare to enclosed masses from stellar kinematics and in IRAS F01364–1042 we compare to enclosed masses from gas kinematics. *III Zw 035 gas-based dynamical masses exist in Medling et al. (2015), but we do not use them for comparison in this work due to likely contamination from a molecular outflow. (1): Enclosed masses from Medling et al. (2015). (2): Gas mass from CO(2-1) flux as calculated in Section 2.4.1. (3): Gas mass from continuum flux as calculated in Section 2.4.2.

topic of dust temperature are discussed within Section 2.6.2.

2.4.3 Spectral index mapping

To better understand the nature of the mm continuum emission in the nuclei of our galaxies, we create inter-band spectral index maps. To create such maps for our galaxies, we generate line-free continuum images for Band 3 (project 2017.1.01235.S, PI Barcos-Muñoz) and Band 6 (data presented here) with the same pixel and beam sizes and using a `robust = -0.5`. We then compute the spectral index per pixel defined as:

$$\alpha = \log\left(\frac{f_{B6}}{f_{B3}}\right) / \log\left(\frac{\nu_{B6}}{\nu_{B3}}\right) \quad (2.5)$$

where f is the flux density in Jy and ν is the frequency (GHz). B3 and B6 indicate the values of flux density and frequency of the images mentioned above. Data below rms of 3 is masked and not mapped. As a general rule, a positive mm spectral index favors dust emission (Planck Collaboration et al. 2016), while a steep negative mm spectral index indicates dominant synchrotron emission (see Section 2.4.2). We estimated the uncertainty of the spectral index via error propagation considering the uncertainty in the flux density due to noise in the image, plus 5 and $\sim 10\%$ errors due to the calibration flux uncertainties in ALMA Bands 3 and 6 respectively (Diaz Trigo et al. 2019).

In Figure 2-4, we show the spectral index maps and related error maps for both galaxies. Given the resolution restrictions of our spectral index maps, we don't have independent measurements of the spectral indices of the nuclei versus the clumpy torus-like structures in III Zw 035. In both cases, the integrated spectral index values are positive in these nuclei. Alongside the f_{extra} measurements in Section 2.4.2 that estimate contribution fractions of free-free and synchrotron emission of $< 50\%$, these spectral index maps suggest that thermal dust emission is a major contributor to the

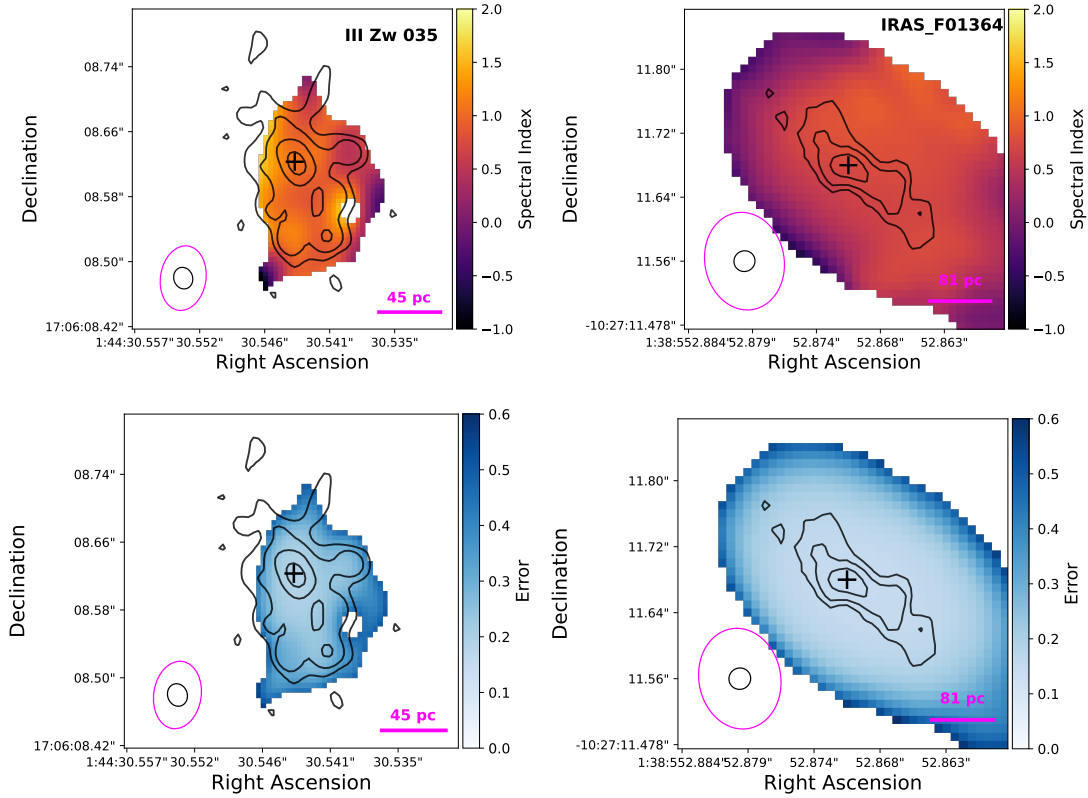


Figure 2-4 Spectral index (top) and uncertainty maps (bottom) for III Zw 035 (left) and IRAS F01364–1042 (right). The beam sizes of the continuum images used to create the spectral index maps ($0.075'' \times 0.052''$ for III Zw 035 and $0.134'' \times 0.110''$ for IRAS F01364–1042) are shown in the lower left corners in magenta. The black contours correspond to the Band 6 combined line-free continuum emission at 230 GHz for III Zw 035 and 228 GHz for IRAS F01364–1042 with levels at 3, 6, 12, 24, 48 \times (rms) Jy beam $^{-1}$ (rms values are 32.9e-6 and 38.3e-6 for III Zw 035 and IRAS F01364–1042 respectively). Their beam sizes are shown in the lower left corners in black (31 x 25 mas for III Zw 035 and 29 x 28 mas for IRAS F01364–1042)

Integrated gas masses compared to enclosed masses measured in this work

	III Zw 035	IRAS F01364–1042
⁽¹⁾ M _{enc,CO}	$(5.26^{+2.21}_{-2.10}) \times 10^7 M_{\odot}$	$(2.09^{+52}_{-63}) \times 10^8 M_{\odot}$
⁽²⁾ M _{gas,CO}	$(9.99 \pm 5.21) \times 10^6 M_{\odot}$	$(2.38 \pm 1.24) \times 10^8 M_{\odot}$
⁽⁴⁾ Gas fraction	$19.0^{+43.2\%}_{-41.1\%}$	$113.9^{+64.3\%}_{-66.5\%}$
⁽³⁾ M _{gas,cont(100K)}	$(2.00 \pm 0.98) \times 10^8 M_{\odot}$	$(3.22 \pm 2.63) \times 10^8 M_{\odot}$
⁽⁴⁾ Gas fraction	$380.2^{+191.0\%}_{-190.4\%}$	$154.1^{+128.3\%}_{-129.4\%}$
⁽³⁾ M _{gas,cont(500K)}	$(3.82 \pm 0.19) \times 10^7 M_{\odot}$	$(6.13 \pm 5.02) \times 10^7 M_{\odot}$
⁽⁴⁾ Gas fraction	$69.8^{+42.2\%}_{-40.0\%}$	$29.3^{+34.6\%}_{-38.5\%}$

Table 2.3 Summary of results for mass estimates via CO (α_{CO} method) and continuum when subtracted from enclosed masses calculated in this work (see Section 2.5). Percentages displayed are relative to those enclosed masses and are calculated as $M_{\text{gas}}/M_{\text{enc}}$. All values in this table are measured at a radius equal to the beam size of the respective CO data. (1): Enclosed masses derived using CO(2-1) kinematics in Section 2.5. (2): Gas mass from CO(2-1) flux as calculated in Section 2.4.1. (3): Gas mass from continuum flux as calculated in Section 2.4.2.

Band 6 continuum emission over other non-thermal or free-free contributions. Further observations at matched resolution to the Band 6 data are necessary to learn more about the radio SEDs of these cores and clumps to make a more direct comparison to our other results.

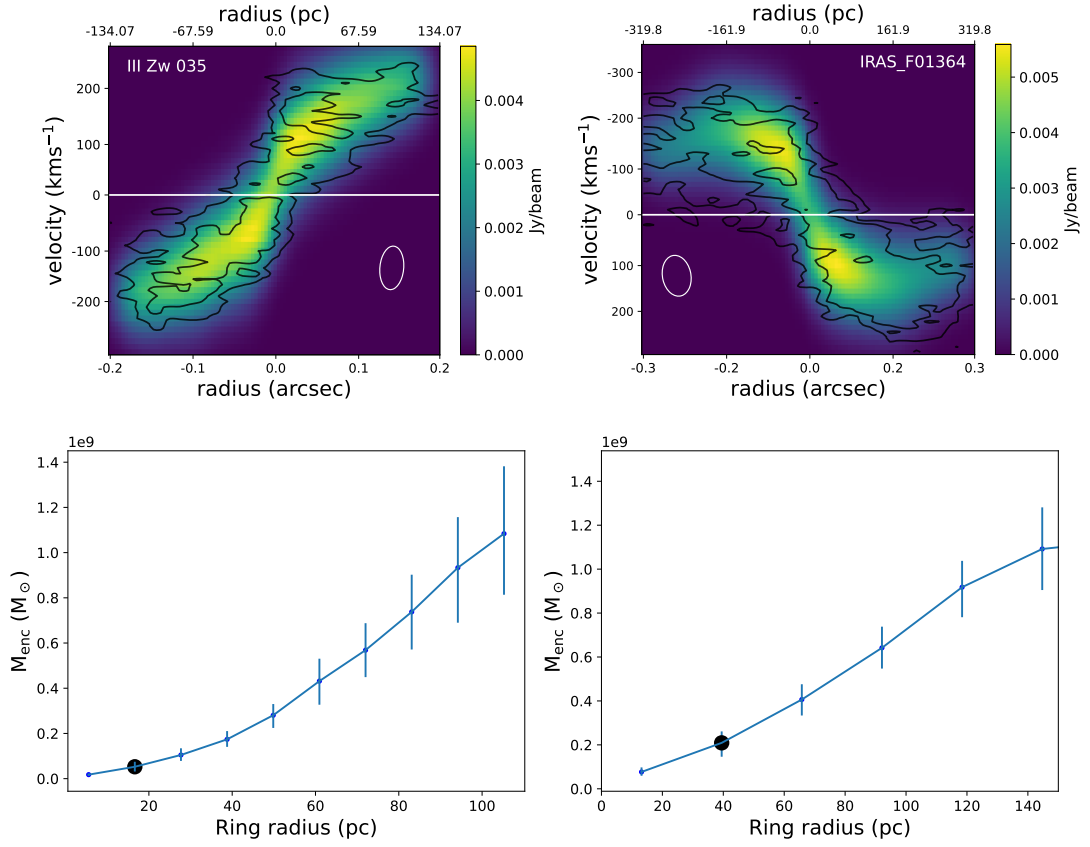


Figure 2-5 Position-velocity (PV) diagrams of the CO emission modeled across the major axis in III Zw 035 (left) & IRAS F01364–1042 (right). *Top:* PV models from ^{3D}Barolo outputs. Black contours correspond to 3, 6, 9, and 12 \times rms of high resolution PV diagrams made in CARTA at the same central position with the same high resolution input cubes described in Section 2.2. White ellipses represent the restoring beams of those data. The white, horizontal lines indicate the expected redshifted frequency of the CO(2-1) line with respect to the systemic velocities of the galaxies. *Bottom:* Inclination-corrected enclosed masses calculated using the methods described in Section 2.5. Enclosed masses were calculated on tilted-rings that were separated by their beam sizes. Both M_{enc} (at beam-sized radii indicated by the black circles) are about an order of magnitude lower than the measurements made in Medling et al. (2015).

2.5 Independent enclosed mass measurements

The results in Section 2.4 present corrected Medling et al. (2015) black hole masses for III Zw 035 and IRAS F01364–1042. With those corrections, the black holes remain overmassive except in the case of III Zw 035 with a sub~175 K dust temperature. In this subsection, we independently measure enclosed masses at the Band 6 beam resolution using the CO cubes presented in this work.

2.5.1 Tilted ring modeling

To calculate dynamical M_{enc} we model the CO kinematics using the tilted-ring modeling algorithm ${}^{3\text{D}}\text{Barolo}$ (Di Teodoro & Fraternali 2015). Using our high resolution CO(2-1) cubes, ${}^{3\text{D}}\text{Barolo}$ models tilted rings with inclination-corrected rotational velocities to the line emission at a range of distances from the center. This 3D modeling approach is preferred over a 2D method in large part due to the instrumental effect of beam smearing being effectively removed during the convolution step (Di Teodoro & Fraternali 2015). We provide initial guesses to ${}^{3\text{D}}\text{Barolo}$ ’s two-stage ${}^{3\text{DFIT}}$ task for parameters like inclination, PA, and redshift. We tested different methods of building the ${}^{3\text{D}}\text{Barolo}$ mask as well, using both SEARCH and SMOOTH&SEARCH. Models and residuals produced in this way are shown in Appendix B. In III Zw 035, the outflow likely dominates the velocity dispersion map. Position angles modeled by ${}^{3\text{D}}\text{Barolo}$ are about 15 degrees lower than those in Medling et al. (2014). This difference in PA may be due to the modeling in this work using kinematics of the cold gas rather than warm gas.

We then use the inclination-corrected, circular velocities and radii of the kinematic models computed by ${}^{3\text{D}}\text{Barolo}$ in our enclosed mass calculation, $M_{\text{enc}} = R_{v\text{max}} v^2 G^{-1}$, where M_{enc} is in kg, R is in m, v is m s^{-1} and G is the gravitational constant. This method assumes a spherical mass distribution. The enclosed mass profiles, along with

the position-velocity models from ^{3D}Barolo and contours of position-velocity diagrams manually made in CARTA (Cube Analysis and Rendering Tool for Astronomy, Comrie et al. 2021a), can be seen in Figure 2-5.

2.5.2 Comparison to warm gas M_{enc}

At 30 and 39 mas for III Zw 035 and IRAS F01364–1042 respectively, we find M_{enc} of $5.26^{+2.21}_{-2.10} \times 10^7$ and $2.09^{+0.52}_{-0.63} \times 10^8 M_{\odot}$ (see Table 2.2) which are between 93-91% lower than those found in Medling et al. (2015) at 77 mas resolution. In Table 2.3, we show new estimates for the central M_{BH} by subtracting matched-resolution molecular gas masses from those high-resolution M_{enc} . Corrected M_{BH} are also compared to BH-galaxy scaling relations in Figure 2-6.

The first main difference that may be leading to different enclosed mass results between the modeling here and in Medling et al. (2015) is the nature of the kinematic tracer. In this work, we use CO(2-1), which traces the cold gas in the nuclei of these galaxies while for IRAS F01364–1042 Medling et al. (2015) modeled the warm-gas tracer Pa α . Given the indication of outflows present in IRAS F01364–1042, Pa α may be an unreliable tracer of the bulk motion of the gas (e.g. in Davies et al. 2024). In III Zw 035, although Medling et al. (2015) derived their masses from stars, which should not be impacted by outflows, the resolution of our cold gas dynamics is higher than obtained with Keck/OSIRIS. The CO beam sizes are 1.5-2 times smaller than the Keck/OSIRIS PSF. This means that we are physically probing kinematics closer to the black hole, thus presumably including less mass other than the black hole (stars, dust, gas) in the process.

The enclosed masses presented in this work have the benefits of using a tracer of the dynamically cold gas and physically probing closer to the SMBH than the measurements of Medling et al. (2015). Like the Medling et al. (2015) warm gas and stellar measurements though, for the purpose of comparison to scaling relations

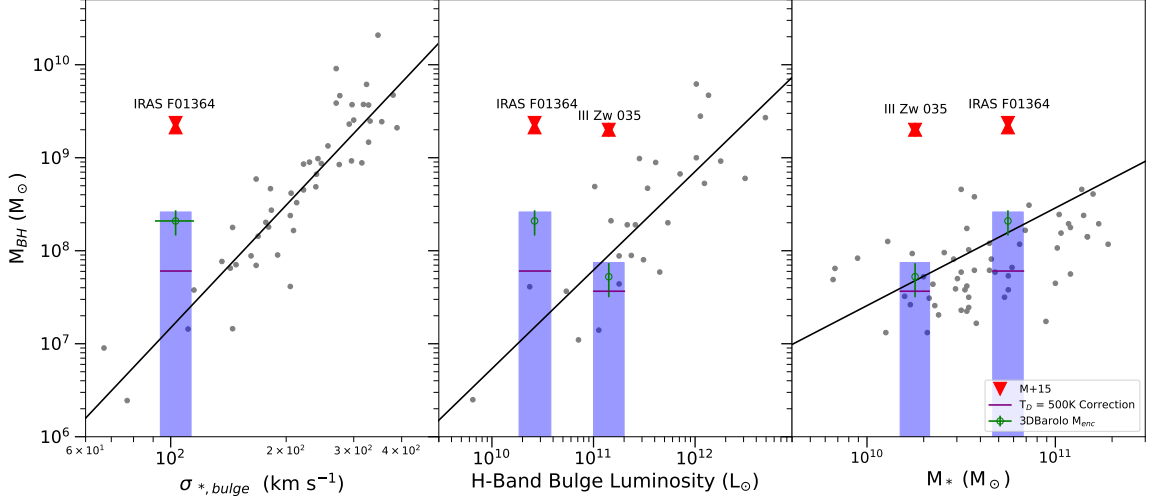


Figure 2-6 Medling et al. (2015) (red) and Section 2.5 (green) enclosed masses plotted on black hole scaling relations: M_{BH} vs. σ_* (left), bulge luminosity L_{bulge} (middle), and total stellar mass M_* (right). Grey points and line fits are based on various literature measurements, see Section 2.6.1 for details. Blue shaded regions represent the widest range of molecular gas-corrected black hole masses ($M_{\text{enc}} - M_{\text{gas}}$) where M_{enc} is the value computed in this work (see Section 2.5). Both the CO-derived gas value and the $T_D = 100\text{-}500$ K continuum methods are included in this range. The purple horizontal lines are the continuum corrected values with $T_D = 500\text{K}$. In all cases, the enclosed gas mass corrects the total enclosed mass measured in this work down to scaling relations.

we remove the, these are still measurements of enclosed mass (from which we can subtract gas mass) rather than black hole mass.

2.6 Discussion

2.6.1 Black hole masses in context

Figure 2-6 shows the black hole masses with our calculated nuclear gas contaminations removed on three scaling relations: M_{BH} vs. σ_* , bulge luminosity L_{bulge} , and total stellar mass M_* . For M_{BH} vs. σ_* we use dynamical data on elliptical and classical bulge galaxies compiled in Kormendy & Ho (2013) with their equation 7 for the best fit line. For M_{BH} vs. L_{bulge} we use luminosities from Marconi & Hunt (2003) and updated black hole masses from McConnell & Ma (2013a) with an updated fit used in Medling et al. (2019). For M_{BH} vs. total stellar mass M_* we use data from Bennert et al. (2011) and Cisternas et al. (2011a), along with a best fit line from McConnell & Ma (2013a).

Results depend on the initial enclosed mass value used for these two nuclei. If we assume that the Medling et al. (2015) enclosed mass (at coarser resolution) is realistic, then the only case where we find enough molecular gas mass to shift either nucleus' dynamically-derived black hole mass down to scaling relations is where III Zw 035's continuum-derived gas mass is below ~ 175 K.

On the other hand, if we assume the dynamical modeling from Section 2.5 is better constrained, we find nearly the opposite. In all cases, subtracting the central molecular gas from the dynamical enclosed mass causes these black holes to fall on to scaling relations.

This dramatic distinction between the two methods could be caused by several factors. As is posited in Medling et al. (2015), non-circular motion could have an impact on those original BH mass measurements. Warm gas is more likely to trace the turbulent outflow than cold gas, which may have driven the M_{enc} from the warm gas up. Conversely, the M_{enc} derived in this work from the cold gas could lead to an underestimate due to dynamically cold gas disks being less susceptible to pressure

support coming from turbulent motions (Barth et al. 2001; Walsh et al. 2013). We find evidence for outflowing components along the minor axis in III Zw 035 and IRAS F01364–1042 in CO(2-1) at these small spatial scales. We also find evidence for mild disk warping in both III Zw 035 and IRAS F01364–1042 in CO(2-1) moment maps, although primarily beyond the radius used to calculate M_{enc} . The disk warping properties on the smallest scales remain unknown, and incorporating corrections for these kinematic deviations – especially for strong central inclination angle shifts – could revise both of the enclosed mass measurements. Future work focused on these galaxies will provide additional information on the magnitude of the non-circular motions caused by the outflows, which we can use to constrain their impact on these enclosed mass measurements (Song et al. in prep for IRAS F01364–1042).

2.6.2 Uncertain Dust Temperature

For our two galaxies, as with the gas, we do not have an accurate estimate for the dust temperature on the scales studied in this work. Our analysis uses the empirical calibration for dust temperature in ULIRGs from Scoville et al. (2016) in which gas mass scales inversely with temperature. Scoville et al. (2016) advocates for a mass-weighted T_D of 25 K based largely on Herschel observations of nearby galaxies (Dunne et al. 2011; Dale et al. 2012; Auld et al. 2013). Other studies in ULIRGs (e.g. Sakamoto et al. 2021 and Walter et al. 2022) have shown that submm luminosity-weighted dust temperatures can exceed 500 K in their nuclei. However, luminosity-weighted dust temperatures are always higher than their mass-weighted counterparts for which the Scoville et al. (2016) relation is calibrated.

This unknown presents a challenge for the results of our continuum-based measurements. As is shown in the bottom panel of Figure 2-3, depending on the temperature assumption, the continuum-estimated molecular gas mass has a \sim 1.5 dex range for each galaxy. At low T_D , at both comparison radii, the corresponding M_{gas} is driven

above even the kinematic measurements from Medling et al. (2015). For III Zw 035 this temperature is \sim 175 K and for IRAS F01364–1042 it is 48 K. If gas is the entirety of the enclosed mass in either case, it leaves no room for a SMBH or stellar component, so we consider these dust temperatures to be firm lower limits. As such, our continuum-based measurements are acting as an upper limit to the molecular gas mass content, and we must wait for more well-constrained dust temperature estimates for these galaxies (perhaps using CO excitation diagrams or RADEX radiative transfer modelling at matched spatial scales, see Viti et al. 2014 for an example in NGC 1068) to better understand the relationship between the two measurement methods.

2.6.3 Implications for physics in nuclei of gas-rich mergers

Whether or not these black holes still remain overmassive with respect to scaling relations depends on which enclosed mass is chosen. As we have discussed, there is reason to believe that because the cold gas measurements are theoretically less impacted by the turbulence caused by outflows, and because these data are at higher resolution, the M_{enc} derived from CO gas-dynamical modeling are more reliable. In this case, the new enclosed masses calculated in Section 2.5 are upper limits on M_{BH} , and both M_{enc} and $M_{\text{enc}} - M_{\text{gas}}$ fall along all scaling relations.

If we adopt values from Medling et al. (2015), those M_{enc} or $M_{\text{enc}} - M_{\text{gas}}$ values all lie significantly above the scaling relations except for III Zw 035 when using a continuum-estimated M_{gas} with $T_D \lesssim 175$ K. As was also found in Medling et al. (2019), kinematically-derived M_{BH} measurements upper limits in ULIRGs may be significantly elevated due to the unresolved (gaseous) mass surrounding SMBH. The impact of cold gas contamination will depend on the nature of each individual system. In the case of the two LIRGs studied here, the fraction of the M_{BH} estimates from Medling et al. (2015) that can be attributed to cold gas could be rather insignificant (2%) to very influential (77% or more depending on dust temperature and comparison

value).

Evolutionarily for III Zw 035, IRAS F01364–1042, and NGC 6240N, overmassive SMBHs would suggest a model where black hole accretion occurs before growth on the larger galaxy scale. Simulations of this growth process suggest the opposite (Hopkins 2012; Cen 2012; Anglés-Alcázar et al. 2017). In merger-driven accretion, material has to travel to the nucleus, losing angular momentum along the way. On this path, there is expected to be a period of mixing and subsequent starburst that could cause global properties like σ_* , L_{bulge} , and M_* to increase before the inflowing gas reaches the nucleus and accretes onto the SMBH. Other than gas accretion, BH-BH mergers can play a part in SMBH mass build-up. These events, however, have uncertain timescales and are not expected to contribute the majority of mass gain for SMBHs like ours (e.g. in Treister et al. 2012; Porras-Valverde et al. 2025). To explain a model where black hole mass can outpace stellar growth in a merger, an angular momentum dissipation mechanism to facilitate rapid accretion of gas needs to be present.

The measurements presented here constrain M_{BH} corrections due to nuclear gas content to a lower limit. The current sample of four total nuclei (NGC6240 N/S, III Zw 035, and IRAS F01364–1042) is limited to these gas-rich mergers and is therefore still not representative or statistically large enough to make corrections to any general sample of SMBHs. In gas-rich LIRG mergers, at least a few to a few tens of percent of the dynamically-measured M_{enc} within a radius of 43–77 pc is gas that could be contaminating the M_{BH} measurements. This gas can be part of the circumnuclear disk, dusty torus, or gaseous flows. Galaxy models should incorporate black hole mass and the full distribution of nuclear gas to properly simulate accretion physics.

Large nuclear gas reservoirs (as are shown to form in gas-rich mergers) are likely to form a viscous accretion disk which transports mass much slower than predicted by Bondi-like accretion models theoretically predicated on free-fall of gas onto the SMBH (Hoyle & Lyttleton 1939, Bondi & Hoyle 1944a, Bondi 1952, Bisnovatyi-Kogan et al.

1979, Mayer et al. 2007, Power et al. 2011). We predict that models of gas-rich mergers that use a Bondi-like accretion prescription are overestimating accretion rates. Gas-rich mergers preferentially form viscous accretion disks, which transfer much less than 1% of their mass onto the SMBH over 5 Myr (Power et al. 2011). Galactic nuclei can coalesce quicker than the larger scale disks, on timescales as short as 10 Myr (Khan et al. 2016). If their central SMBHs are to become overmassive, we hypothesize that SMBH accretion in systems like these should start early on in the merger timeline.

2.7 Conclusions

In this work we used high resolution (sub-30 mas) CO(2-1) and continuum observations of two nearby LIRGs, III Zw 035 and IRAS F01364–1042, to measure molecular gas mass within the central few 10s of pc. Fractionally, we find that between 2 and 77% of the enclosed masses calculated in Medling et al. (2015) from stellar or gas kinematics can be attributed to molecular gas within 10s of parsecs from the central black holes. At higher resolution, the enclosed masses within the inner 40 mas are 91-93% lower than from kinematics taken over a larger region. Molecular gas mass contributes at least 19% of the new enclosed mass.

Because of the higher resolution and less kinematically disturbed nature of cold gas, we expect the new dynamically-derived enclosed masses calculated in Section 2.5 to be closer to the true black hole mass of these merging systems. In all cases, starting from this enclosed mass, III Zw 035 and IRAS F01364–1042 fall on the black hole mass scaling relations shown in Figure 2-6. In most cases this is true even before subtracting the enclosed molecular gas mass. These new measurements are still limited in that they are enclosed masses rather than black hole masses, and our sample size is low. Very high resolution observations of cold gas for the remaining sample of overmassive black holes found in Medling et al. (2015) (IRAS F17207-0014,

NGC 2623, and CGCG 436-030) and independent enclosed mass measurements of NGC 6240’s nuclei would allow us to understand if these nuclei all fall on scaling relations when using cold gas as a tracer.

The accuracy of accretion modeling is directly limited by our understanding of typical nuclear gas masses and distributions. With significant nuclear molecular gas, a viscous accretion disk is likely to form, causing a slower rate of accretion. However, the resulting non-spherical accretion could potentially also circumvent the Eddington limit; if super-Eddington accretion were common, it would have significant implications for the growth of supermassive black holes in the early universe and throughout cosmic time. Additionally, because many cosmological simulations rely on spherically-symmetric black hole accretion rate prescriptions, the presence of nuclear gas disks could limit their predictive power regarding the impacts of black hole growth and subsequent AGN feedback. We need more high resolution datasets like the ones present here to push towards a unified picture of the average gas mass within galactic nuclei. Our current sample of four nuclei (NGC6240 N/S, III Zw 035, and IRAS F01364–1042) is not large enough nor representative of all gas-rich mergers. Regardless, gas should not be left unconsidered when using dynamics to derive black hole masses in gas-rich galaxies.

Chapter 3

Direct Tests of Black Hole Accretion Rate Prescriptions: I. Bondi Accretion at Different Scales

In Chapter 2 we outlined various methods for measuring aperture-integrated molecular gas mass. Accretion rate depends on the amount of gas available for SMBH fueling. In this Chapter we test a sub-grid technique for modeling SMBH accretion rate by measuring the parameters that are input to it, such as molecular gas mass density.

3.1 Introduction

Supermassive black holes (SMBHs), despite their small gravitational radius of the sphere of influence ($1 \sim 100$ pc), are thought to be a key piece of the connection between pc and kpc scales of galaxy evolution. Observations of galaxies with active galactic nuclei (AGN) have shown both directly and indirectly that AGN can inject energy into their surrounding environments, which can ultimately quench or in some cases trigger star formation (see Fabian 2012 for an observational review; Mercedes-Feliz

et al. (2023) for a simulated example).

Active galactic nuclei do not only reside in the central part of galaxies, they may also significantly impact several global properties of galaxies and their surrounding inter-galactic media, allowing us to indirectly infer their influence on those observables. Relationships between black hole mass and global galaxy properties, like the velocity dispersion of stars in the galactic bulge, have been well-calibrated and show tight correlations (see Kormendy & Ho 2013; McConnell & Ma 2013b for reviews). These correlations suggest that AGN radiative feedback, which in part depends on black hole mass, may leave an imprint on bulge stellar velocity dispersion (see Ferrarese & Merritt 2000; Gebhardt et al. 2000 for seminal studies) but fueling regulation (Escala 2007; Chen et al. 2013; Anglés-Alcázar et al. 2013; Anglés-Alcázar et al. 2017) and non-causal mass averaging through mergers (Peng 2007; Hirschmann et al. 2010; Jahnke & Macciò 2011) have also been proposed as plausible drivers of black hole-galaxy scaling relations. Star formation in massive halos at redshift < 3 is suppressed (e.g. in Behroozi et al. 2013; Torrey et al. 2014), which could be caused by heating of the interstellar medium (ISM) from AGN feedback. In the high energy regime, a discrepancy of a factor of 2-3 is found between the observed and expected correlations between X-ray luminosities and temperatures of gas in the intra-cluster medium (called the L_X -T relation, see Mushotzky 1984; Markevitch 1998). The L_X -T relation is predicated on gravitational heating being the only energy source heating the gas (Kaiser 1986; see also Stott et al. 2012) – the observed slope of 2-3 suggests that gas in the intra-cluster medium is heated by non-gravitational effects. This means it evolves differently from dark matter; energetics input by host AGN could be a factor as to why.

Alongside indirect cases of the impact of AGN feedback on galaxy formation histories, the direct effects of AGN on the ISM have been observed for decades. Since more than 100 years ago (M87; Curtis 1918) radio jets powered by a central

SMBH have been seen to extend up to \sim 0.9 Mpc outside from their host galaxies (e.g. Centaurus A; Burns et al. 1983). Outflows driven by these SMBHs have been observed in the process of depleting the ISM at outflow rates of $700 \text{ M}_\odot \text{ yr}^{-1}$ (e.g. in Mrk 231; Feruglio et al. 2010) . NGC 1068, which is the test case in the rest of this Chapter has a complex and well studied AGN-driven outflow that has been observed to impact its ISM on sub-kpc scales (e.g. Wilson & Ulvestad 1983; Müller-Sánchez et al. 2011; García-Burillo et al. 2014; Saito et al. 2022; Hviding et al. 2023; Holden & Tadhunter 2023; Gallimore & Impellizzeri 2023; Mutie et al. 2024; Hagiwara et al. 2024).

The energy output of an AGN is driven by mass accretion onto its accretion disk, fueled by inflows in the nuclei of galaxies. This gas then accelerates to speeds of up to $> 0.1c$ in the accretion disk, and that disk can power radiative outflows. These energetics interact with the ISM, wthe effects of which we call feedback. The direct observational feedback can be classified as two mechanisms: radiative (quasar mode) or kinetic (radio mode) (Fabian 2012). In the quasar mode, occurring when the black hole accretes mass quickly, photons from the accretion disk couple to the ISM, transferring momentum in a powerful jet. In radio mode, accretion onto the disk is slower, and the primary feedback mechanism is in the form of collimated radio jets that typically appear narrower than quasar-mode jets (see Cielo et al. 2018 for a simulated comparison between the feedback of the two modes). Both modes can drive outflows, but the quasar-mode is thought to start the quenching process (the spatial extent of which grows over time) and then the radio-mode maintains that quenched state (see Fabian 2012 and Morganti 2017 for reviews).

As simulations of galaxy evolution have been informed by increasingly detailed observations, theorists have begun to study the physical mechanisms that drive AGN feedback and how that feedback impacts the simulated host galaxies. Dubois et al. (2013a) (see also Dubois et al. 2013b; Taylor & Kobayashi 2015) examined how AGN

jets impact cold gas and transform blue, disk galaxies into red ellipticals. Building on these studies, Rosas-Guevara et al. (2015), who simulated accretion in galaxies of varied halo mass, find that in galaxies with M_{Halo} above $10^{11.5} M_{\odot}$, as was observed in Behroozi et al. (2013), star formation is suppressed by AGN feedback. Valentini et al. (2020) perform a suite of cosmological simulations in which they couple AGN feedback to different phases of the ISM. They find, in part, that energy output from the AGN as feedback must couple with both the cold and hot phases in order to avoid excessive SMBH growth.

As is seen in both observations and simulations, global galaxy properties can be affected by accretion-dependent feedback. Theorists have attempted to model the physical processes causing those properties to change. Williamson et al. (2020) perform radiation hydrodynamics modeling of the 1-100 pc scales in a nuclear region of a simulated AGN host. They demonstrate that increasingly polar winds are produced when anisotropic radiation from the AGN shifts the mass distribution of the outflow originating from the AGN. Meenakshi et al. (2022) simulated the direct interaction between AGN jet-induced outflows on 2 kpc scale and the ISM and found shocked emission fronts in the ISM that could be responsible for stunting star formation. On $r < 1$ pc scale, Wada et al. (2023) were able to induce radiation-driven dusty outflows which impact the ISM as they continue on their outward paths. Tying the small and large scales together has been an ongoing challenge.

Due to computational constraints, large-scale cosmological simulations that can model hundreds of Mpc^3 at a time are not able to directly resolve the physical processes that drive gas accretion at $<<1$ pc scales where accretion takes place, and so sub-grid prescriptions for black hole accretion and its subsequent feedback must be adopted.¹ The ‘sub-grid’ is defined as the region below the gridded resolution of

¹Although there is also much variation in AGN feedback prescriptions, this program will focus on discussing the accretion rate prescriptions, on which all feedback depends.

the simulation. Unfortunately, there is no unified model for these sub-grid physics, and different studies use different accretion prescriptions. The most commonly applied prescription is the one described in Bondi (1952), often referred to as the Bondi accretion prescription. The equation for the mass accretion rate follows the form:

$$\dot{M}_{\text{Bondi}} = \frac{4\pi G^2 M_{\text{BH}}^2 \rho}{(c_s^2 + v_{\text{rel}}^2)^{3/2}} \quad (3.1)$$

where G is the gravitational constant, M_{BH} is the mass of the black hole, ρ is the gas density, c_s is the sound speed, and v_{rel} is the relative velocity of the gas. In the pure Bondi case, the gas is assumed to be stationary relative to the galactic potential, so v_{rel} is zero. This model is theoretically predicated on gas falling directly onto the SMBH once it reaches the Bondi radius, $R_{\text{Bondi}} = 2GM_{\text{BH}}/c_s^2$. The Bondi radius is where the escape velocity of the SMBH (based on its mass) equals the sound speed of the gas in the nuclear region. The physical scale of the Bondi radius is typically of order 0.1-300 pc if we assume c_s of 400 km s⁻¹ and SMBH mass range of $10^6 \sim 10^9 M_\odot$. Some large scale cosmological simulation suites that use a pure Bondi prescription to account for SMBH accretion, including *MassiveBlack-II* (Khandai et al. 2015) and *IllustrisTNG* (Weinberger et al. 2017; Pillepich et al. 2018a).

Physically, the issue with the Bondi accretion formalism is that it ignores both the angular momentum of the gas and interactions due to self-gravity between the gas, stellar, and dark matter components, which is only appropriate in the case of hot, virialized gas (Hobbs et al. 2012; Negri & Volonteri 2017; Anglés-Alcázar et al. 2021). Recent studies have shown that gas and other accreting material still has angular momentum inside what may be the Bondi radius, particularly in gas-rich mergers or galaxies with Seyfert AGN (e.g. in Davies et al. 2004; Hicks et al. 2013; Medling et al. 2014; Lin et al. 2016), and so Bondi accretion timescales may be much shorter than in reality where angular momentum delays accretion. Feedback from the AGN

in such models self-regulates this rapid growth (Anglés-Alcázar et al. 2017).

Because of the M_{BH}^2 dependence of accretion rate in Bondi accretion prescriptions, low mass BH seed growth is suppressed such that BHs do not grow quick enough to match their expected mass at corresponding redshifts. To account for this discrepancy, some large-scale cosmological simulation suites adjust the accretion physics by using modified versions of Bondi accretion. The prescription in the *Illustris* (the predecessor to *IllustrisTNG*; Vogelsberger et al. 2013; Genel et al. 2014) and *Magneticum Pathfinder* hydrodynamical simulation suites (Hirschmann et al. 2014; Bocquet et al. 2016; Dolag et al. 2016) modify Bondi by multiplying Equation 3.1 by a constant (unitless) ‘boost’ factor α (following the prescription of Springel et al. 2005; Di Matteo et al. 2005; Springel & Hernquist 2005). The boost factor is used to account for the volume average of the Bondi-rates for both the cold and hot phases in the simulations and typically has a value = 100. Another large-scale cosmological model, *Horizon-AGN* (Dubois et al. 2016), uses an α similar to *Illustris* and *Magneticum*, but instead of a constant value, their boost factor (following the prescription from Booth & Schaye 2009; see also Dubois et al. 2012) is $\alpha = (\rho/\rho_0)^2$ or $\alpha = 1$ for densities above and below the threshold for star formation respectively. *EAGLE* (Schaye et al. 2015) uses a pure Bondi prescription alongside the heuristic correction from Rosas-Guevara et al. (2015) to account for variable angular momentum of accreting gas. Another approach, used by the large-scale *Romulus* suite (Tremmel et al. 2017) is to adjust the Bondi accretion rate depending on the motion of the simulated gas particles. In *Romulus*, if the smallest relative velocity (which they equate to v_{bulk} , the bulk motion of the gas) of the gas particle closest to the SMBH is faster than the rotational velocity of the gas, they replace the relative velocity of the SMBH (in Equation 3.1) with v_{bulk} and multiply the Bondi rate by a density-dependent boost factor similar to *Horizon-AGN*.

Bondi or Bondi-like accretion prescriptions are the most commonly used, but theo-

rists have also designed accretion prescriptions with very different underlying physics. One large-scale simulation ($[100 h^{-1} \text{ Mpc}]^3$ volume) suite that in part uses one of these prescriptions is *SIMBA* (Davé et al. 2019). In *SIMBA*, pure Bondi accretion is still applied for hot gas accretion where, as we mentioned, it is most appropriate. But, they then apply a torque-limited accretion formalism for the cold gas where instabilities in the disk drive mass inflow (Hopkins & Quataert 2011; Anglés-Alcázar et al. 2017).

Understanding if and in which cases different sub-grid prescriptions are accurately estimating accretion rates onto the black holes of galaxies is critically important to cosmological simulations and conclusions drawn from them. Without an accurate prescription for accretion over time, simulations cannot accurately implement the impact of AGN feedback, and as such may have incorrect outcomes with regards to galaxy formation and evolution. Depending on the assumed accretion prescription, simulations find that BH scaling relations are driven either by feedback efficiency (in Bondi-like models), or accretion efficiency (in a torque-driven model; see Anglés-Alcázar et al. 2021 for further discussion). Theorists’ conclusions on which physics drive the co-evolution between BH mass and global galaxy properties is directly dependent on which accretion model is implemented. Determining which accretion formalism is most appropriate in which circumstances is critical to understanding BH-galaxy co-evolution in our Universe.

Observationally testing how black hole accretion rate prescriptions perform has only become possible in recent times. In this study, in the prototypical Seyfert 2 galaxy NGC 1068, we directly measure the parameters that go into Bondi accretion, ρ_{gas} and c_s , on physical scales ranging from 2-500 pc. To achieve the high resolution required for the measurements we use observations of the cold and warm components of the nuclear gas from ALMA mm interferometry and Keck/OSIRIS NIR integral field spectroscopy (see Section 3.3). We then plug these measured parameters into the

pure Bondi accretion prescription as a function of radius to mimic what a simulation at that resolution would estimate for the black hole accretion rate. Finally, we test these predicted Bondi accretion rates against empirically derived accretion rates using hard (14-195 keV) X-ray data from The Burst Alert Telescope (BAT) AGN Spectroscopic Survey (BASS) (Ricci et al. 2017b). The BAT instrument (Barthelmy et al. 2005; Krimm et al. 2013) on *Swift* (Gehrels et al. 2004) is a hard X-ray detector that surveys the entire sky, reporting X-ray sources to within 1-4 arcmin accuracy. In this work, we use cosmological parameters of $H_0 = 70 \text{ km s}^{-1} \text{ Mpc}^{-1}$, $\Omega_m = 0.28$, and $\Omega_\Lambda = 0.72$ (Hinshaw et al. 2009). To calculate spatial scales and luminosity distance to NGC 1068 we use Ned Wright’s Cosmology Calculator (Wright 2006).

3.2 Nuclear structure of NGC 1068

NGC 1068 is one of the most-studied prototypical Seyfert galaxies, and as such a wealth of information has already been published about its nuclear structure. The studies described here are not an exhaustive list, but are included to provide context relevant to our analysis.

At 2.2 pc resolution, NGC 1068 hosts a water maser that is thought to originate from the accretion disk on much smaller (<0.1 pc) scales. Greenhill et al. (1996) observed the maser with very long baseline interferometry (VLBI) using both the Very Long Baseline Array and Very Large Array to achieve 0.65 pc resolution. They used the velocity gradient of the maser emission to infer a rotational velocity of the gas, and in turn constrain $M_{\text{BH}} \sim 1 \times 10^7 M_\odot$. Kumar (1999) modeled the 0.65-1.1 pc disk from which the maser emission is thought to be ejected from. The clumps in their disk model interact with each other, leading to eventual accretion onto the SMBH.

On slightly larger scales with near and mid infrared interferometry, multiple au-

thors were able to resolve a two-component dusty torus (Jaffe et al. 2004; Raban et al. 2009). One component is smaller and more elongated (1.35×0.45 pc) in size than the other (3×4 pc). In the nucleus of Circinus, another Seyfert 2 AGN, Tristram et al. (2014) also found a two-component dusty torus. Images like these that showed structure inconsistent with the prior, observationally-defined, Type 2 classification of these galaxies (unless foreground extinction was applied) fundamentally challenged the AGN unification model (Antonucci 1993).

Gámez Rosas et al. (2022) used sub-pc resolution observations of NGC 1068 taken with the MATISSE/ESO/VLTI interferometer between 3 and $13\text{ }\mu\text{m}$ to map the dust temperature distribution of the dust observed in the previously mentioned studies. They confirm an optically thick pc scale dusty structure and a second, less optically thick disk that extends to at least 10 pc. García-Burillo et al. (2019) (who in part use the same ALMA data as we describe in Section 3.3.2) find a 14 pc CO(2-1) nuclear disk with a PA ($\sim 110\text{-}140$ deg) aligned with the water maser disk PA (140 deg). Also in García-Burillo et al. (2019), they observe the circumnuclear disk (CND), which as can be seen in Figure 3-1, has a gas deficit inside the CND in its central ~ 130 pc region.

To resolve the kinematics of the 10 pc inner disk (often referred to as the torus) and CND, Imanishi et al. (2020) observe both of these scales using HCN J=(3-2) and HCO⁺ J = (3-2) transitions with ALMA at 1.4 pc resolution. They find that the torus as observed with these dense gas tracers rotates in the opposite direction with respect to the CND and water maser emission. This is particularly surprising because the water maser emission is rotating in the same direction as the CND rather than the torus it is physically closer to (see Figure 1 of Imanishi et al. 2020). In García-Burillo et al. (2019), the authors also find counter-rotation in CO(2-1). They find that a "significant part" of the observed counter-rotation in CO(2-1) can be attributed to a northern AGN-driven wind. To make a more robust determination though, García-

Burillo et al. (2019) say that higher resolution data is required so that the outflowing component can be better disentangled from the rotating component.

Outflows originating from the AGN can serve to regulate black hole accretion, and NGC 1068 hosts a complex outflow in the NE direction, perpendicular to the nuclear disk. The largest outflow component is seen as the radio jet (e.g. in Gallimore et al. 1996). Mutie et al. (2024) present higher resolution (~ 4 pc) *e*-MERLIN 5 GHz data along with archival VLA 10 GHz, and VLA 21 GHz images of the jet. These images together show not only the central jet emission, but also detail in the larger scale bow shock, >200 pc from the SMBH in the same NE direction, which exhibits direct evidence of the AGN’s impact on the ISM. The impact of the jet on the ISM is studied in part in both Hviding et al. (2023) and Holden & Tadhunter (2023), who both show evidence for gas ionization consistent with shock ionization or radiation-bounded AGN-photoionization along the outflow’s path on 160 pc to kpc scale. García-Burillo et al. (2014) show that the CO kinematics on distances 50 to 400 pc are spatially correlated with the radio jet, evidence that the AGN is influencing even the cold ISM. ALMA CO(6-5) observations from Gallimore et al. (2016) show that this molecular outflow originates within 2 pc from the SMBH, and has velocities relative to systemic of about 400 km s^{-1} .

3.3 NGC 1068 observations

For NGC 1068, we made use of <3 pc scale resolution observations both in the near infrared (NIR) with Keck/OSIRIS+AO (adaptive optics; PI Medling), and in the mm with ALMA archival data (PI García-Burillo). High resolution observations like these are critical to radially sampling the predicted Bondi accretion rate in Section 3.4.

3.3.1 Keck/OSIRIS K-band Integral Field Spectroscopy

The first of two sets of data we are using in this project is a set of high resolution integral field unit (IFU) Keck/OSIRIS+AO (OH-Suppressing InfraRed Imaging Spectrograph, Larkin et al. 2006) integrations, for which we mosaic all frames into a single data cube. These observations were taken with the Kbb filter (broad-band K between $1.965 - 2.381 \mu\text{m}$) with the $35 \text{ mas pixel}^{-1}$ plate scale on 2018 December 28th, 2019 January 22nd, and 2019 October 7th for a total exposure time of 6120 seconds (51 frames, 120 seconds each). Weather impacted observations on 2019 October 7th, during which the laser guiding system was also not working. For NGC 1068 we used the galaxy nucleus as the natural guide star in NGS mode, and as the tip/tilt star in LGS mode. AO corrections in those frames without the laser produced larger point spread functions with full-width at half-maximum (FWHM) values between 3 and 5 pixels compared to ~ 2 with the laser on other nights. We reduced the Keck/OSIRIS+AO observations using the OSIRIS Data Reduction Pipeline (OSIRIS-DRP, Lyke et al. 2017; Lockhart et al. 2019) version 4.2.0, which we use to extract a spectrum for each spatial pixel, assemble the spectra into a cube, and mosaic the 51 total frames together to form the final image, which has a $0.17''$ point spread function (PSF) FWHM. Flux calibration was applied for each night before final mosaicking.

The resulting mosaic reveals a strong K-Band continuum (particularly near the AGN) and H₂ 1-0 rovibrational emission (S(0), $\lambda_{\text{rest}} = 2.2235\mu\text{m}$; S(1), $\lambda_{\text{rest}} = 2.1218\mu\text{m}$; S(2)), $\lambda_{\text{rest}} = 2.0338\mu\text{m}$. These line+continuum and continuum-subtracted H₂ 1-0 S(1) maps are shown in the middle and right panels of Figure 3-1 respectively. The line+continuum map was made using the Cube Analysis and Rendering Tool for Astronomy (CARTA, Comrie et al. 2021b) and the continuum subtracted H₂ 1-0 S(1) map was made using QFitsView (Ott 2012). Both images show peaks of emission on or near the position of the central engine, and NGC 1068's circumnuclear disk (CND)

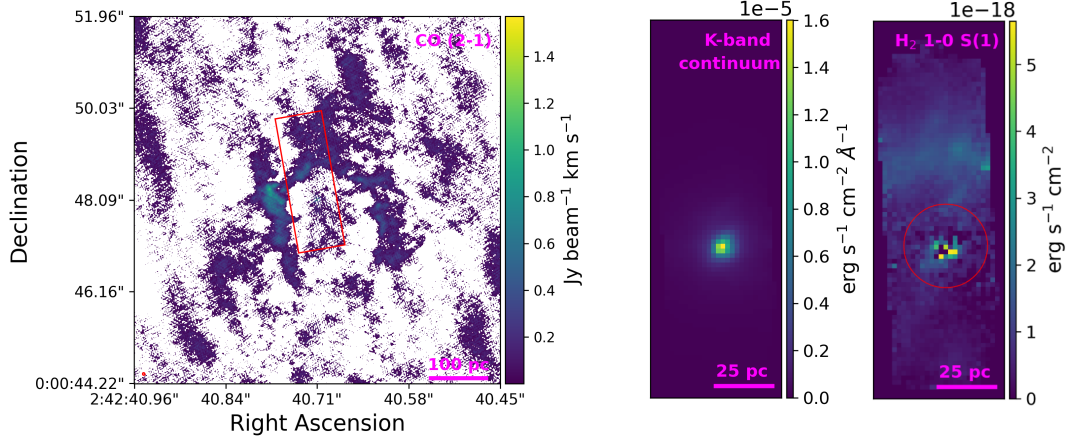


Figure 3-1 Nuclear region of NGC 1068 in the CO(2-1) flux (left, from ALMA), $2.2\mu\text{m}$ continuum (middle), and the continuum subtracted rovibrational H_2 1-0 S(1) transition (right), described in Section 3.3. The CO(2-1) moment 0 map is masked below $3\times\text{rms}$ and the red box in the CO(2-1) moment map represents the field of view of the NIR data. The very small, red ellipse in the bottom left represents the beam size of the ALMA data (41×30 mas). All three images show flux peaks at the AGN's location and both the CO and H_2 maps have enhanced emission in the CND ring. The red circle in the H_2 1-0 S(1) moment map represents the aperture in which T_{kin} is calculated in Figure 3-3.

ring can be seen in the H_2 map.

3.3.2 ALMA Band 6 Long-baseline Interferometry

We chose the highest resolution CO $J = (2-1)$ (hereafter CO(2-1)) available on the ALMA archive that shows strong emission (PI García-Burillo, Project code 2016.1.00232.S; see also García-Burillo et al. 2019). We retrieved the CO(2-1) spectral cube product from the ALMA archive, which has a rms of 0.25 mJy over 20 km s^{-1} , and was imaged using a Briggs (Briggs 1995) robust value of 0, resulting in a beam size of 41×30 mas. We then used this spectral cube with the image cube analysis tools in **CARTA** (Comrie

et al. 2021b) to create a moment 0 (flux) map of the CO(2-1) emission. Figure 3-1 (left) shows this CO(2-1) moment 0 map which is masked below $3 \times \text{rms}$ and is used for our analysis in Section 3.4. Like in the warm H₂ observations, the CND ring is a bright source in CO(2-1).

3.4 Prescription parameters

In this pilot study, we examine the performance of the most commonly used accretion prescription for black hole growth in NGC 1068. The Bondi accretion formalism with a relative velocity of zero (also known as Bondi-Hoyle, or Bondi-Hoyle-Lyttleton e.g. Hoyle & Lyttleton 1939; Bondi & Hoyle 1944b; Bondi 1952) follows the form:

$$\dot{M}_{\text{Bondi}} = 4\pi G^2 M_{\text{BH}}^2 \rho c_s^{-3} \quad (3.2)$$

where G is the gravitational constant, M_{BH} is the mass of the black hole, ρ is the gas density and c_s is the sound speed.

Bondi accretion is predicated on a spherically symmetric, non-self-gravitating gas distribution in which the gas inside the Bondi radius has no angular momentum. While this kind of environment may not be most appropriate for describing all galaxy nuclei (see Section 3.6 for additional information), Bondi accretion is a simple analytical prescription that can be applied inside a sphere of any radius, which makes it convenient as a sub-grid prescription.

In this subsection, we outline the methods for measuring each free parameter in the Bondi prescription using the available high resolution data from Section 3.3.

3.4.1 Parameter 1: black hole mass

Greenhill et al. (1996) imaged NGC 1068's water maser emission at 0.65 pc scales

using very long baseline interferometry. From the rotation curve of the water maser emission, they found the enclosed mass within that radius to be $\sim 1 \times 10^7 M_{\odot}$ (with uncertainty of order unity). Another study by Lodato & Bertin (2003) derive a smaller black hole mass of $\sim 8 \pm 0.3 \times 10^6$ in a self-gravitating accretion disk model that matches the Greenhill et al. (1996) and Greenhill & Gwinn (1997) observations well. The Lodato & Bertin (2003) model corrects for non-Keplerian motion in the velocity profile of the water maser emission, but this could be an over-correction. In fact, other studies have found that the disk rotation may still be dominated by the black hole (Imanishi et al. 2018). Albeit with a worse fit to the velocities from the maser emission, Lodato & Bertin (2003) also fit a Keplerian rotation model, which has a best fit black hole mass of $\sim 1.5 \pm 0.02 \times 10^7 M_{\odot}$. In the absence of clear evidence in favor of one of the newer modeling schemes, we adopt the Greenhill et al. (1996) value of $M_{\text{BH}} = \sim 1 \times 10^7 M_{\odot}$ as an intermediate M_{BH} measurement.

3.4.2 Parameter 2: gas density

3.4.2.1 Choice of volume element

To measure the gas density, we first must define our volume element. In cosmological simulations, typically, a fixed number of gas particles exist inside a spherical region with radius r centered on the location of the SMBH. This volume makes up the black hole kernel, in which the accretion physics are prescribed. Although studies like the ones discussed in Section 3.2 and Vollmer et al. (2022) have shown that the ~ 10 pc cold gas distribution is more disk-like, we opt to use a sphere of volume $V = \frac{4}{3}\pi r^3$ centered on the AGN for which we vary the radius with the goal of mimicking the spherical radial aperture that simulations typically use to evaluate Bondi accretion.

3.4.2.2 Cold gas mass

To measure the cold molecular gas (H_2 and He) mass inside the sphere, we use the CO(2-1) data described in Section 3.3.2. To obtain a molecular gas mass, we utilize the conversion factor α_{CO} . The exact value of α_{CO} depends on several factors including the size scale and environment over which the CO flux is measured. The picture is further complicated by the distinction between $\alpha_{CO(1-0)}$ and $\alpha_{CO(2-1)}$, where the difference is dictated by the ratio between the line luminosity of the two rotational transitions: r_{21} ($r_{21} = L'_{CO(2-1)} / L'_{CO(1-0)}$), which depends on the temperature of the gas. In this work, we follow the same α_{CO} methodology as in García-Burillo et al. (2019) who use the Milky Way $\alpha_{CO(1-0)} = 4.3 \pm 1.29 M_\odot(K \text{ km s}^{-1} \text{ pc}^2)^{-1}$ recommended by Bolatto et al. (2013). We use $\alpha_{CO(1-0)}$ in conjunction with the averaged line intensity ratios for NGC 1068's northern and southern CND regions (because the CND ring contains the majority of the nuclear gas mass): $r_{21} = 2.2 \pm 0.4$, from Viti et al. (2014) to calculate a final

$$\alpha_{CO(2-1)} = \frac{\alpha_{CO(1-0)}}{r_{21}} = \frac{4.3 \pm 1.29}{2.2 \pm 0.4} = 1.95 \pm 0.73 M_\odot(K \text{ km s}^{-1} \text{ pc}^2)^{-1}. \quad (3.3)$$

The outflowing components of NGC 1068 may have a lower $\alpha_{CO(1-0)}$, but we expect the Milky Way value to be closer to the average for the purpose of measuring integrated enclosed masses, especially at larger r . The outflow's impact on our gas mass measurement is expected to be small as there is not much CO(2-1) emission between the AGN and CND ring, and the CND ring itself does not visually appear disturbed along the path of the outflow. $\alpha_{CO(2-1)}$ is then multiplied by the luminosity inside a circular aperture of radius r , to match our spherical geometry. The enclosed mass profile is shown alongside a snapshot of the aperture geometry in Figure 3-2.

García-Burillo et al. (2019), who center their $r = 200$ pc aperture measurement on the center of the CND ring, find a molecular ($H_2 +$ helium) gas mass of ≈ 1.4

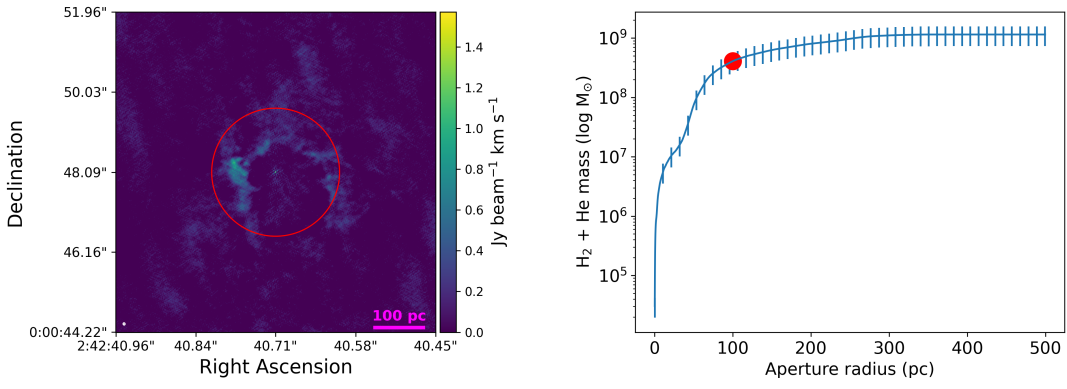


Figure 3-2 *Left*: Moment 0 map of CO(2-1) in NGC 1068, with flux density values masked below $3 \times \text{rms}$. The red circle indicates the location and size of the 100 pc aperture (centered on the AGN) corresponding to the red dot in the right panel, which has $M_{\text{enc}, \text{H}_2 + \text{He}} = 4.09 \pm 1.49 \times 10^8 \text{ M}_{\odot}$. The small, white ellipse in the bottom left represents the beam size of the ALMA data (41×30 mas). *Right*: Integrated mass profile inside the radial aperture. Details on the conversion to molecular gas mass can be found in Section 3.4.2.

$\times 10^8 M_{\odot}$. We measure molecular gas mass within the same aperture (using CARTA to measure flux) and find $1.3 \pm 0.5 \times 10^8 M_{\odot}$ ($1.4 \pm 0.5 \times 10^8 M_{\odot}$ if centered on the AGN), both of which are consistent with the García-Burillo et al. (2019) measurement. For comparison to another nearby Seyfert 2, in the nuclear region of Circinus, using the warm gas tracer H₂ 1-0 S(1), Müller Sánchez et al. (2006) (based on the correlation between L_{IR} and L_{CO}; see Young & Scoville 1991 for a review) find the total cold molecular gas mass to be $1.7 \times 10^7 M_{\odot}$ within 0.8'' (52pc). Integrated inside the same physical distance from the SMBH in NGC 1068, we find a molecular gas mass of $8.8 \pm 3.2 \times 10^7 M_{\odot}$, higher by almost 1 dex.

To convert enclosed mass to density we divide by the volume of the sphere with radius r (see Section 3.4.2.1) with r defined by our circular aperture size used for measuring mass. In this sphere with r = 100 pc centered on the AGN as shown in Figure 3-2 (left), we find a molecular gas mass density of $93.3 \pm 71.1 M_{\odot} pc^{-3}$.

3.4.2.3 Warm H₂ gas mass

We also calculate an enclosed mass using the warm H₂ gas measured from the NIR data, following Equation 6 of Storchi-Bergmann et al. (2009), which uses the line flux of the H₂ 1-0 S(1) rovibrational transition at $\lambda_{rest} = 2.1218 \mu m$. Martins et al. (2010) used the NASA 3-m Infrared Telescope Facility (IRTF) to observe NGC 1068 and found a nuclear (slit 1''x 2'') extinction E(B-V) of 1.13 (from their Table 4). Assuming the standard extinction law of Cardelli et al. (1989) with R_v = 3.1, the extinction A_v ($A_v = R_v \times E(B-V)$) is ~ 3.5 . Based on $A_k \sim A_v / 10$ (Howarth 1983), we measure the H₂ 1-0 S(1) extinction-corrected intrinsic flux ($F_{intrinsic} = F_{observed} \times 10^{(0.4A_k)}$) and directly convert it to the warm H₂ gas mass. The extinction-corrected H₂ gas mass inside r < 1.7'' (111 pc) is $\sim 68 M_{\odot}$, about 1.38 times the (uncorrected) observed value. Due to the rectangular FOV, only an aperture radius of < 0.3'' is fully contained within the OSIRIS FOV, suggesting that H₂ emission at radii > 0.3'' is incomplete.

Regardless, the warm H₂ mass is inconsequential compared to the CO-derived value of $4.08 \pm 1.49 \times 10^8 M_{\odot}$ in the same region.

Other than the field of view, a primary reason that the warm gas measurement in this region may be so small is due to the radiative environment in NGC 1068's nucleus. Under local thermal equilibrium (LTE, where the energy distribution can be described by a single number locally) conditions, the H₂ emission can be excited by the equilibrium value for temperatures $T \approx 1000$ K (Davies et al. 2005). To reach such high excitation temperatures in NGC 1068, H₂ emission lines can be excited through several mechanisms, as described below:

(1) *UV fluorescence*: This excitation mechanism dominates in photodissociation regions (PDRs). Far-ultraviolet (FUV, $\lambda > 912$ Å) radiation pumps the molecule into electronically excited states, leading to subsequent cascades that emit fluorescent emission (Wakelam et al. 2017). This mechanism is dominant in Seyfert 1 galaxies (Davies et al. 2005). Although NGC 1068 is classified as a Seyfert 2 galaxy and is expected to have less FUV radiation, the HST/FOC UV image shows a bright nucleus with polarization (Barnouin et al. 2023) within our OSIRIS field of view (FOV).

(2) *Shocks and outflows*: Veilleux et al. (1997) suggest that shocks associated with nuclear outflows are a likely heating source for H₂ in many Seyfert 2 galaxies. May & Steiner (2017) analyzed VLT/SINFONI and Gemini/NIFS data with a larger FOV covering the entire CND and proposed that the CND could be an expanding bubble.

(3) *X-ray heating from the AGN*: X-ray emission can penetrate deeply into regions that are opaque to UV photons and influence H₂ excitation (Matt et al. 1997). All of these mechanisms can contribute to H₂ emission.

3.4.3 Parameter 3: sound speed of the gas

The final parameter required in the Bondi accretion formalism is the sound speed of the gas. The sound speed for an ideal gas is:

$$c_s = \sqrt{\frac{\gamma k_B T_K}{\mu m_p}} \quad (3.4)$$

where γ is the adiabatic index (1, as the gas is assumed to be isothermal in each sub-region), k_B is the Boltzmann constant 1.381×10^{-16} erg $^{-1}$ K $^{-1}$, T_K is the temperature of the gas (K), and μ is the mean molecular weight of the gas, which is 2.7 since we assume the molecular gas is H₂, 10% helium, and trace metals, and m_p is the mass of a proton (kg). All but the temperature in this case are constants.

For the temperature of the molecular gas, we use two methods: one using CO rotation diagrams (cold gas), and another using an excitation diagram for the molecular H₂ (warm gas) from our Keck/OSIRIS+AO NIR data.

3.4.3.1 CO-derived c_s

For a temperature from CO transitions we refer to the work of Viti et al. (2014) who infer the temperature of the gas in the CND of NGC 1068 by using CO rotation diagrams. This method assumes that the gas is in LTE, and that the observations are mostly in the Rayleigh-Jeans regime where the intensity of the radiation is proportional to the temperature. This temperature is also known as the ‘rotational temperature’ and is equal to the kinetic temperature if all CO levels are thermalized (Goldsmith & Langer 1999). Because of these assumptions, this temperature should be considered a lower limit, which translates to an upper limit on our final accretion rate because $\dot{M}_{\text{Bondi}} \propto c_s^{-3}$. For the central region of NGC 1068, Viti et al. (2014) find a temperature of 50 ± 5 -7 K via the CO rotation diagram method (see Section 3.1.1. of their work for more details). Plugging that and the other constants into

Equation 3.4, we find that the speed of sound in the cold molecular gas phase is 391.0 \pm 135.4 m s⁻¹.

3.4.3.2 H₂-derived c_s

As shown in Section 3.4.2.3, warm H₂ is also present in NGC 1068's nuclear regions, so we also consider the sound speed for this component of the ISM. To measure the temperature which we then use in the c_s calculation, we use the H₂ 1-0 S(0), S(1), and S(2) rovibrational line fluxes in the Keck/OSIRIS NIR data described in Section 3.3.1. Assuming the H₂ gas is in LTE, the H₂ excitation temperature is equal to the kinetic temperature. Figure 3-3(a) shows the H₂ excitation diagram, which is the column density in the upper level of each transition normalized by its statistical weight (N_u/g_u) as a function of energy of the level as a temperature (E_u). The best-fit slope of this relationship is related to T_K as $\frac{N_u}{g_u} \propto e^{(-\frac{\hbar\nu}{kT_K})}$ in the LTE description of energy level populations (see pages 322, 327 of Wilson et al. 2013). Solving for T_K then yields $-\frac{1}{T_K} \propto \frac{\ln \frac{N_u}{g_u}}{\frac{E_u}{k}}$. Because we have spatially resolved data for these H₂ lines, we can derive kinetic temperatures from 12-111 pc and apply them at the matched distances in the accretion rate prediction. While the Keck/OSIRIS+AO data has a higher resolution than 6 pc, the H₂ 1-0 S(1) and S(2) lines are not detected in a $r \leq 6$ pc (0.1") aperture. Fluxes of the lines are measured using the line fitting tool in **QFitsView** (Ott 2012), which we use to fit the continuum and one Gaussian component to the integrated (within a region circular region with radius r) spectrum. Figure 3-3(b) shows the range of excitation temperatures as a function of radius. T_{kin} ranges from 678-2261 K, and peaks at $r \leq 85$ pc where $T_{kin} = 2261^{+3683}_{-1631}$ K. High temperatures may be caused by the influence of the PDR (Section 3.4.2.2 describes observations of this for NGC 1068), which is found to increase the H₂ 1-0 S(1) emission by up to 70% in the some luminous infrared galaxies (Davies et al. 2000; Davies et al. 2003). Using Equation 3.4 (with a mean molecular weight of H₂ only) results in warm

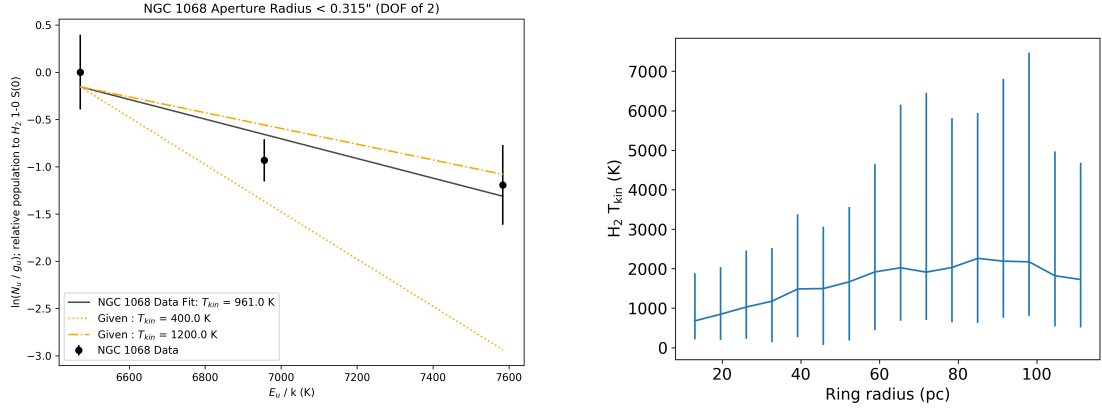


Figure 3-3 (*Left:*) Column density in the upper level of each H_2 1-0 S(0), S(1), and S(2) transition as a function of energy level of that transition as a temperature (K) inside a $r = 21$ pc circular aperture centered on the AGN as shown in Figure 3-1. The best fit slope (using linear regression), as described in Section 3.4.3.2, is the temperature of the gas in that region if we assume LTE. (*Right:*) T_{kin} estimated as in the excitation diagram on the left but instead inside circular apertures matching the methods of Section 3.4.2 from $0.2''$ to $1.7''$ in steps of $0.1''$. The mean of the derived temperatures is 1612^{+2840}_{-1216} K.

H_2 sound speeds between 1440-2629 m s $^{-1}$, peaking at $r = 85$ pc.

3.5 Results: \dot{M}_{Bondi} vs. $\dot{M}_{\text{X-ray}}$

3.5.1 Calculating \dot{M}_{Bondi}

Now that we have calculated each parameter for the Bondi accretion prescription in Section 3.4, we are ready to estimate a Bondi accretion rate. Because our parameters are spatially resolved, we calculate accretion rate as a function of radial distance r representing a simulated resolution:

$$\dot{M}_{\text{Bondi}}(r) = 4\pi G^2 M_{\text{BH}}^2 \rho(\leq r) c_s(\leq r)^{-3}. \quad (3.5)$$

Figure 3-4 shows the Bondi accretion rate for the cold derived case as a function of radius, the means of which range between about 10^2 and $10^{-3} M_{\odot} \text{ yr}^{-1}$. As the enclosed mass found in Section 3.4.2 for the warm H_2 gas component in $r < 170$ pc is small ($68 M_{\odot}$), and the temperature gradient is high (678-2261 K, see Section 3.4.3.2) relative to the values found for the cold CO gas component, the resulting Bondi accretion rates are much smaller (between about 10^{-10} and $10^{-7} M_{\odot} \text{ yr}^{-1}$) for the warm gas. These results suggest that the cold gas is the dominant carrier of mass accretion on $r < 170$ pc scales. Table 3.1 shows a range of precise values for both the cold and hot Bondi accretion rates.

3.5.2 Calculating X-ray accretion rates

To understand how well the Bondi accretion formalism compares to the real accretion rate, we compare it to the X-ray derived accretion rate. To calculate an accretion rate from X-ray measurements, we use *Swift*/BAT data from the BAT AGN Spectroscopic Survey (BASS, Ricci et al. 2017b). They present intrinsic luminosities in the

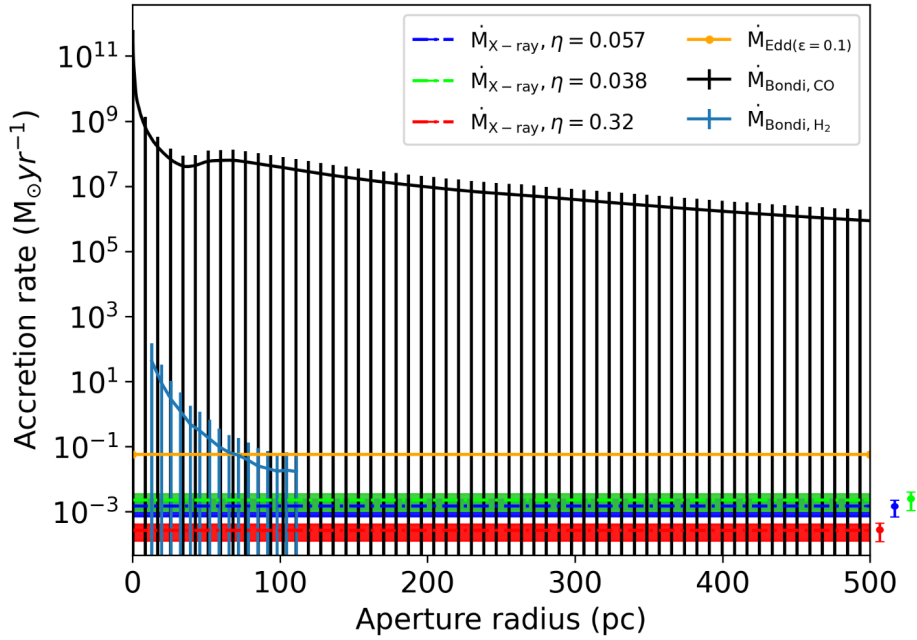


Figure 3-4 X-ray and (Cold-derived) Bondi accretion rates as a function of radius over which nuclear parameters are measured. Color bars and ranges displayed to the right denote uncertainties on each X-ray measurement. Regardless of which gas component is used to estimate \dot{M}_{Bondi} , the Bondi prescription overestimates \dot{M}_{BH} by orders of magnitude, and is above the Eddington rate (orange line, with radiative efficiency $\epsilon = 0.1$). For the cold gas case, which represents the majority of gas available for accretion in NGC 1068, Bondi overpredicts the accretion rate by between 9 and 13 orders of magnitude.

14-195 keV band, which we use alongside the bolometric correction, Equation 17 in Gupta et al. (2024):

$$\log(\kappa_{14-195}) = (0.13 \pm 0.04) \times \log(\lambda_{\text{Edd}}) + (1.04 \pm 0.05) \quad (3.6)$$

to calculate bolometric luminosity. Because Ricci et al. (2017b) measure a neutral column density of $\log N_{\text{H}} = 25.0 \text{ cm}^{-2}$ in NGC 1068 and the X-ray continuum might not be well estimated when the emission is dominated by reprocessed radiation in environments like this, we conservatively estimate uncertainty on the input intrinsic 14-195 keV luminosity to be ± 0.4 dex. We then use that bolometric luminosity in the equation from Netzer & Trakhtenbrot (2014), $L_{\text{bol}} = \eta \dot{M} c^2$, solving for \dot{M} where η is the unitless mass-to-radiation conversion efficiency that depends on the spin of the black hole. For stationary, retrograde disk, and maximally rotating SMBHs respectively, the values for η are 0.057, 0.038, and 0.32 (Netzer & Trakhtenbrot 2014). For NGC 1068, we find $\dot{M}_{\text{X-ray}}$ values equal to $1.51 \pm 0.81 \times 10^{-3} M_{\odot} \text{yr}^{-1}$ (stationary SMBH), $2.26 \pm 1.21 \times 10^{-3} M_{\odot} \text{yr}^{-1}$ (retrograde accretion disk), and $2.69 \pm 1.43 \times 10^{-4} M_{\odot} \text{yr}^{-1}$ (maximally spinning SMBH). As shown in Figure 3-4 and Table 3.1, \dot{M}_{Bondi} overestimates the accretion rate by several orders of magnitude in the warm gas case to up to 13 orders of magnitude in the cold gas case in small aperture radii. In Section 3.6 we discuss the implications of such a discrepancy with respect to cosmological simulations.

Vollmer et al. (2022) used the IR-derived bolometric luminosity for the AGN in NGC 1068 from Vollmer et al. (2018) to calculate $\dot{M}_{\text{BH}} \sim L_{\text{bol}} / (0.1c^2) \sim 0.05 M_{\odot} \text{yr}^{-1}$. They calculate a mass accretion rate onto their modeled accretion disk for NGC 1068 to be $2 \times 10^{-3} M_{\odot} \text{yr}^{-1}$ ($\eta = 0.1$), which is in agreement with our $\dot{M}_{\text{X-ray}}$ values.

Method	Accretion rate ($M_{\odot} \text{ yr}^{-1}$)						
X-rays ($\epsilon = 0.038$)							$2.26 \pm 1.21 \times 10^{-3}$
X-rays ($\epsilon = 0.057$)							$1.51 \pm 0.81 \times 10^{-3}$
X-rays ($\epsilon = 0.32$)							$2.69 \pm 1.43 \times 10^{-4}$
Bondi ($< r$)	5 pc	10 pc	25 pc	50 pc	100 pc	200 pc	500 pc
($T_{\text{Kin}} = 50 \text{ K}$)	$1.86 \pm 2.05 \times 10^9$	$4.87 \pm 5.37 \times 10^8$	$7.16 \pm 7.89 \times 10^7$	$5.69 \pm 6.27 \times 10^7$	$3.87 \pm 4.27 \times 10^7$	$0.95 \pm 1.05 \times 10^6$	$8.75 \pm 9.64 \times 10^6$
($T_{\text{Kin}} = 678\text{-}2261 \text{ K}$)	*	*	$2.85^{+10.07}_{-7.54}$	$1.73^{+5.53}_{-4.89}$	$1.76^{+8.23}_{-4.18} \times 10^{-1}$	*	*

Table 3.1 Accretion rate measurements and estimates for rates derived from X-ray luminosities and the pure Bondi accretion prescription inside various radii. In NGC 1068, where the cold gas phase makes up the bulk of the gas mass in the nucleus, the cold gas derived Bondi accretion estimate outpaces the X-ray derived accretion rates by between 2 and 4 orders of magnitude. *H₂ 1-0 S(1) and S(2) lines required to calculate temperature for the Bondi calculation are not detected in this aperture.

3.6 Discussion: results in the context of simulations

To inform theorists on which accretion prescriptions in their simulations are best to use and when, we have designed our measurements to fit in the practical context of those simulations. Large scale cosmological simulations must use sub-grid physics for accretion because of computing constraints. As mentioned earlier, some examples of hydrodynamical galaxy evolution simulations that use spherically symmetric, Bondi or Bondi-like black hole accretion formalisms are *Illustris/IllustrisTNG* (Genel et al. 2014; Vogelsberger et al. 2014; Pillepich et al. 2018b), *Magneticum Pathfinder* (Hirschmann et al. 2014; Bocquet et al. 2016; Dolag et al. 2016), *MassiveBlack-II* (Khandai et al. 2015), *Eagle* (Schaye et al. 2015), *Horizon-AGN* (Dubois et al. 2016), *Romulus* (Tremmel et al. 2017), and *SIMBA* (Davé et al. 2019, uses Bondi for hot

gas only). The resolution of the hydrodynamical gas cells in which these sub-grid physics is typically close to 1 kpc. In the highest resolution zoom-in simulations, the spherical radius in which particle calculations are made is approximately 10 pc (Wetzel et al. 2023). Hyper-refinement simulations (e.g. Anglés-Alcázar et al. 2021; Hopkins et al. 2024), where gas resolution elements are dynamically split to reach high resolution can reach spatial scales smaller than 10 pc, but these simulations can only be practically run for short periods of cosmic time due to computing constraints.

Because we have spatially-resolved measurements, we are able to examine the performance of Bondi accretion at a range of spatial scales. For the Bondi accretion rate derived from warm gas we are limited by the field of view of OSIRIS ($0.56 \times 2.24''$ with our observational setup), but the ALMA data extends to over 500 pc away from the SMBH.

Table 3.1 shows the Bondi accretion rates estimated at radii between 5-500 pc as calculated in Section 3.5, and the X-ray accretion rates as calculated in Section 3.5.2, which are all plotted together in Figure 3-4. At all aperture radii, regardless of whether we are estimating \dot{M}_{Bondi} using the cold or warm gas component, the parameterized Bondi accretion rate exceeds the X-ray derived accretion rate (by 1 or more dex in the warm gas case and by 10 or more dex in the cold gas case).

This is, perhaps, not a surprising result. Past studies have hinted towards Bondi accretion overestimating the real accretion rate. Di Matteo et al. (2000) found that luminosities calculated using estimated Bondi accretion rates for six black holes with masses of $0.22\text{-}5.2 \times 10^9 M_{\odot}$ determined in Magorrian et al. (1998) were 4-6 orders of magnitude higher than the real luminosities of the galaxy nuclei. Hopkins et al. (2016) model SMBH accretion in a gas-rich nuclear disk in a massive simulated galaxy with 0.1 pc resolution. In their study, applying a pure Bondi accretion formalism resulted in an accretion rate $\sim 10^8$ times higher than the luminosity-derived accretion rate native to their simulation. That accretion rate ($\sim 10^7 M_{\odot}$), agrees with our cold-gas

derived Bondi accretion rate between approximately 25 and 200 pc in NGC 1068. Near the SMBH, pure Bondi accretion ignores the possibility that gas particles may have angular momentum. The gas in the simulation used in Hopkins et al. (2016) is primarily cold and is supported by angular momentum rather than radiation pressure. Observations show that especially in gas-rich galaxies that naturally host molecular torii, the $r < 100$ pc cold gas reservoir is large, has significant angular momentum, and is the primary candidate for black hole accretion fueling (Davies et al. 2004; Hicks et al. 2013; Medling et al. 2014; Lin et al. 2016; Gaspari et al. 2015). Ignoring the angular momentum of the cold gas is likely the primary cause of the overestimate that Bondi accretion makes in Di Matteo et al. (2000), Hopkins et al. (2016), and in this work.

If NGC 1068 is typical, these results suggest that the usage of pure Bondi accretion is likely to struggle to accurately predict black hole accretion rates. From our example, in the cold gas estimate which represents the majority of the mass available for accretion, the pure Bondi accretion prediction dramatically (by up to 13 orders of magnitude) overpredicts the true accretion rate. Understanding the physical mechanisms that drive accretion on the sub-grid scales in galactic nuclei can inform the future development of accretion prescriptions. The Bondi prescription allows particles to fall directly onto the BH inside the Bondi radius, but our results suggest that angular momentum plays an important role in some nuclei.

3.7 Conclusions

In this study we estimate a Bondi accretion rate as a function of radius for NGC 1068 using two different molecular gas tracers, and compare the result to the direct accretion rate derived from hard X-ray luminosity of the AGN. Compared to warm H₂ gas, CO gas is the dominant mass carrier close to the SMBH. Following this, the

cold gas derived Bondi accretion rate estimate outpaces the X-ray derived value by more than 9 orders of magnitude at all aperture sizes.

The work described in this Chapter is a pilot for a wider study of AGN and accretion prescriptions. Direct probes of sub-grid accretion prescriptions may, as our sample expands, help identify which physical processes dominate accretion on a variety of spatial scales, and in turn provide recommendations for appropriate sub-grid prescriptions to describe them. The results in this work support previous evidence that in high resolution cosmological simulations, applying a Bondi accretion prescription can lead to large overestimates of \dot{M}_{BH} and therefore large overestimates of AGN feedback, which in turn impacts the global galaxy evolutionary track. We note that this is a test for a specific Seyfert 2 AGN. To make more robust recommendations about the application of the Bondi accretion prescription for sub-grid accretion physics we must directly test Bondi on more galaxies.

Chapter 4

Summary & Future Expansion of Tests of Black Hole Accretion Rate Prescriptions

In this Chapter I summarize how the projects herein have impacted our understanding of the connection between nuclear gas and SMBH accretion physics. I also outline how the framework from Chapters 2 and 3 can be used for future tests of black hole accretion rate prescriptions.

4.1 Nuclear Molecular Gas Content in LIRGs

In Chapter 2, I shared our work where we examined the nuclear molecular gas mass inside two LIRGs, with the goal of understanding whether molecular gas could explain the overmassive nature of the SMBHs (enclosed masses) in their centers found in Medling et al. (2015). First, we measured the molecular gas mass inside a square aperture ($r < 77$ mas) as a function of radius using two different mass conversions for III Zw 035 and IRAS F01364–1042. We find that between $\sim 5\text{--}75\%$ of the Medling et al. (2015) enclosed mass can be attributed to molecular gas rather than the SMBH.

Next, we perform an independent measurement of enclosed mass using the high resolution CO data used throughout Chapter 2. Using CO kinematics modeled with ^{3D}Barolo find enclosed masses ~ 1 dex lower than the Medling et al. (2015) enclosed masses (inside a smaller radial distance from the SMBH). If we attribute the new enclosed mass to the SMBH and correct for gas mass, both III Zw 035 and IRAS F01364–1042 fall on scaling relations.

4.2 Direct Tests of Black Hole Accretion Rate Prescriptions

In Chapter 3 we directly test the performance of the most commonly used black hole accretion rate prescription, Bondi, against the X-ray derived accretion rate for NGC 1068 as a function of radius. Carefully considering how accretion is modeled is critical because accretion drives feedback, which impacts galaxy evolution. We described methods of measuring the parameters that go into the Bondi prescription – specifically sound speed and molecular gas mass density. We then input those parameters as a function of radius and compared the result to an accretion rate derived using hard X-ray data. The primary result for NGC 1068 is that Bondi accretion overestimates the black hole accretion rate by orders of magnitude at all radii, overestimating by up to 13 orders of magnitude on the smallest scales. This result matches with previous studies that have shown that the primary fuel for SMBH accretion, cold gas, has angular momentum, a fact that the Bondi formalism ignores.

4.3 Future Expansion of Direct Tests of Black Hole Accretion Rate Prescriptions

The work described in Chapter 3 is a pilot for a wider study of AGN and accretion prescriptions. In Chapter 3 we tested the most frequently prescribed accretion formalism, Bondi. We created a framework for measuring properties like gas mass density and sound speed within a radially growing aperture centered on the AGN, so that we could make recommendations for simulation suites of varied resolution. But, this work was done for one prescription, and for one galaxy. This Section will outline the options for expansion of tests on SMBH accretion prescriptions, both with regards to different prescriptions and expanding the galaxy sample size.

As discussed in Section 3.1, different large scale cosmological simulations use different accretion prescriptions. Simulation suites like *Illustris* (Vogelsberger et al. 2013; Genel et al. 2014), *Magneticum Pathfinder* (Hirschmann et al. 2014; Bocquet et al. 2016; Dolag et al. 2016), *Horizon-AGN* (Dubois et al. 2016), and *Romulus* suite (Tremmel et al. 2017) use modified versions of the Bondi accretion formalism in which they use various methods to attempt to account for the phase (hot or cold) of the gas particles. Testing modified Bondi would be a natural first step in the progression towards a more completely sampled field of accretion prescriptions.

As samples of high resolution observations of nuclear molecular gas (the primary carrier of mass in SMBH accretion) have continued to grow, the application of simplified Bondi-like accretion has become less physically motivated. So, it might be expected that more and more theorists designing large scale cosmological simulations will use prescriptions that are described by the new observations. In fact, as mentioned in Section 3.1, *SIMBA* (Davé et al. 2019) is already doing so – they apply a torque-limited accretion formalism for the cold gas (Hopkins & Quataert 2011; Anglés-Alcázar et al. 2017). While it is immediately important to test accretion prescriptions

already used in large scale cosmological simulations, testing theorized prescriptions that may be candidates for the next generation of simulations to provide preemptive recommendations for theorists may be even more productive. Constraining how well prescriptions like torque-limited (Hopkins & Quataert 2011; Anglés-Alcázar et al. 2017), turbulent viscosity (Kawakatu & Wada 2008), and ballistic (Hobbs et al. 2012) accretion perform (using observed input parameters) against observed X-ray accretion rates is key to the interpreting the accuracy of the affect of AGN feedback on galaxy evolution in future large-scale cosmological simulations.

Other than testing more prescriptions, it is also very important to expand the galaxy sample in which they are tested. Chapter 3 uses observations of NGC 1068. While it is one of the most well-studied AGNs, it is not representative of a wide variety of AGN types or nuclear environments. The parameters measured in Section 3.4 are derived using previously observed warm gas with Keck/OSIRIS and archival observations of cold gas with ALMA. These observatories provide the unique qualities of being able to observe the tracers important to measuring parameters (like H₂ 1-0 and CO for Bondi accretion) at high (<50 mas) spatial resolution. Obtaining the very high resolution data should be a priority as the gridded resolution of simulations in the future may become finer. More targets with similar observations are already currently available, and testing accretion rate prescriptions in them is a logical next step.

References

- Abbott, B. P., Abbott, R., Abbott, T. D., et al. 2016, , 116, 061102, doi: 10.1103/PhysRevLett.116.061102
- Anglés-Alcázar, D., Faucher-Giguère, C.-A., Quataert, E., et al. 2017, , 472, L109, doi: 10.1093/mnrasl/slx161
- Anglés-Alcázar, D., Özel, F., & Davé, R. 2013, , 770, 5, doi: 10.1088/0004-637X/770/1/5
- Anglés-Alcázar, D., Quataert, E., Hopkins, P. F., et al. 2021, , 917, 53, doi: 10.3847/1538-4357/ac09e8
- Antonucci, R. 1993, , 31, 473, doi: 10.1146/annurev.aa.31.090193.002353
- Armus, L., Mazzarella, J. M., Evans, A. S., et al. 2009, , 121, 559, doi: 10.1086/600092
- Auld, R., Bianchi, S., Smith, M. W. L., et al. 2013, , 428, 1880, doi: 10.1093/mnras/sts125
- Barcos-Muñoz, L., Leroy, A. K., Evans, A. S., et al. 2017, , 843, 117, doi: 10.3847/1538-4357/aa789a
- Barnouin, T., Marin, F., Lopez-Rodriguez, E., Huber, L., & Kishimoto, M. 2023, , 678, A143, doi: 10.1051/0004-6361/202347336
- Baron, D., Netzer, H., Prochaska, J. X., et al. 2018, , 480, 3993, doi: 10.1093/mnras/sty2113

- Barth, A. J., Sarzi, M., Rix, H.-W., et al. 2001, , 555, 685, doi: 10.1086/321523
- Barth, A. J., Strigari, L. E., Bentz, M. C., Greene, J. E., & Ho, L. C. 2009, , 690, 1031, doi: 10.1088/0004-637X/690/1/1031
- Barthelmy, S. D., Barbier, L. M., Cummings, J. R., et al. 2005, , 120, 143, doi: 10.1007/s11214-005-5096-3
- Behroozi, P. S., Wechsler, R. H., & Conroy, C. 2013, , 770, 57, doi: 10.1088/0004-637X/770/1/57
- Beifiori, A., Courteau, S., Corsini, E. M., & Zhu, Y. 2012, , 419, 2497, doi: 10.1111/j.1365-2966.2011.19903.x
- Bell Burnell, J. 1969, doi: 10.17863/CAM.4926
- Bennert, V. N., Auger, M. W., Treu, T., Woo, J.-H., & Malkan, M. A. 2011, , 742, 107, doi: 10.1088/0004-637X/742/2/107
- Bennert, V. N., Treu, T., Ding, X., et al. 2021, , 921, 36, doi: 10.3847/1538-4357/ac151a
- Bentz, M. C., Denney, K. D., Grier, C. J., et al. 2013, , 767, 149, doi: 10.1088/0004-637X/767/2/149
- Bisnovatyi-Kogan, G. S., Kazhdan, Y. M., Klypin, A. A., Lutskii, A. E., & Shakura, N. I. 1979, , 23, 201
- Bocquet, S., Saro, A., Dolag, K., & Mohr, J. J. 2016, , 456, 2361, doi: 10.1093/mnras/stv2657
- Bolatto, A. D., Wolfire, M., & Leroy, A. K. 2013, , 51, 207, doi: 10.1146/annurev-astro-082812-140944

- Bondi, H. 1952, , 112, 195, doi: 10.1093/mnras/112.2.195
- Bondi, H., & Hoyle, F. 1944a, , 104, 273, doi: 10.1093/mnras/104.5.273
- . 1944b, , 104, 273, doi: 10.1093/mnras/104.5.273
- Booth, C. M., & Schaye, J. 2009, , 398, 53, doi: 10.1111/j.1365-2966.2009.15043.x
- Briggs, D. S. 1995, in American Astronomical Society Meeting Abstracts, Vol. 187, American Astronomical Society Meeting Abstracts, 112.02
- Burns, J. O., Feigelson, E. D., & Schreier, E. J. 1983, , 273, 128, doi: 10.1086/161353
- Burton, W. B., Gordon, M. A., Bania, T. M., & Lockman, F. J. 1975, , 202, 30, doi: 10.1086/153950
- Cackett, E. M., Bentz, M. C., & Kara, E. 2021, iScience, 24, 102557, doi: 10.1016/j.isci.2021.102557
- Cappellari, M. 2008, , 390, 71, doi: 10.1111/j.1365-2966.2008.13754.x
- Cardelli, J. A., Clayton, G. C., & Mathis, J. S. 1989, , 345, 245, doi: 10.1086/167900
- CASA Team, Bean, B., Bhatnagar, S., et al. 2022, , 134, 114501, doi: 10.1088/1538-3873/ac9642
- Cen, R. 2012, , 755, 28, doi: 10.1088/0004-637X/755/1/28
- Chandrasekhar, S. 1931, , 74, 81, doi: 10.1086/143324
- Chen, C.-T. J., Hickox, R. C., Alberts, S., et al. 2013, , 773, 3, doi: 10.1088/0004-637X/773/1/3
- Cheung, E., Bundy, K., Cappellari, M., et al. 2016, , 533, 504, doi: 10.1038/nature18006

Cicone, C., Maiolino, R., Sturm, E., et al. 2014, , 562, A21, doi: 10.1051/0004-6361/201322464

Cicone, C., Severgnini, P., Papadopoulos, P. P., et al. 2018, , 863, 143, doi: 10.3847/1538-4357/aad32a

Cielo, S., Bieri, R., Volonteri, M., Wagner, A. Y., & Dubois, Y. 2018, , 477, 1336, doi: 10.1093/mnras/sty708

Cisternas, M., Jahnke, K., Bongiorno, A., et al. 2011a, , 741, L11, doi: 10.1088/2041-8205/741/1/L11

Cisternas, M., Jahnke, K., Inskip, K. J., et al. 2011b, , 726, 57, doi: 10.1088/0004-637X/726/2/57

Clavel, J., Reichert, G. A., Alloin, D., et al. 1991, , 366, 64, doi: 10.1086/169540

Combes, F. 1991, , 29, 195, doi: 10.1146/annurev.aa.29.090191.001211

Comerford, J. M., Pooley, D., Barrows, R. S., et al. 2015, , 806, 219, doi: 10.1088/0004-637X/806/2/219

Comrie, A., Wang, K.-S., Hsu, S.-C., et al. 2021a, CARTA: The Cube Analysis and Rendering Tool for Astronomy, 2.0.0, Zenodo, doi: 10.5281/zenodo.4905459

—. 2021b, CARTA: The Cube Analysis and Rendering Tool for Astronomy, 2.0.0, Zenodo, doi: 10.5281/zenodo.3377984

Condon, J. J., & Ransom, S. M. 2016, Essential Radio Astronomy

Cortes, P. A., Vlahakis, C., Hales, A., et al. 2023, ALMA Cycle 10 Technical Handbook (Cycle 10; Doc. 10.3; version 1.1), Zenodo. <https://doi.org/10.5281/zenodo.7822943>, doi: 10.5281/zenodo.7822943

Cretton, N., de Zeeuw, P. T., van der Marel, R. P., & Rix, H.-W. 1999, , 124, 383, doi: 10.1086/313264

Curtis, H. D. 1918, Publications of Lick Observatory, 13, 9

Dale, D. A., Aniano, G., Engelbracht, C. W., et al. 2012, , 745, 95, doi: 10.1088/0004-637X/745/1/95

Davé, R., Anglés-Alcázar, D., Narayanan, D., et al. 2019, , 486, 2827, doi: 10.1093/mnras/stz937

Davies, R., Ward, M., & Sugai, H. 2000, , 535, 735, doi: 10.1086/308890

Davies, R., Shimizu, T., Pereira-Santaella, M., et al. 2024, , 689, A263, doi: 10.1051/0004-6361/202449875

Davies, R. I., Sternberg, A., Lehnert, M., & Tacconi-Garman, L. E. 2003, , 597, 907, doi: 10.1086/378634

Davies, R. I., Sternberg, A., Lehnert, M. D., & Tacconi-Garman, L. E. 2005, , 633, 105, doi: 10.1086/444495

Davies, R. I., Tacconi, L. J., & Genzel, R. 2004, , 613, 781, doi: 10.1086/423315

Davis, B. L., Graham, A. W., & Cameron, E. 2018, , 869, 113, doi: 10.3847/1538-4357/aae820

—. 2019, , 873, 85, doi: 10.3847/1538-4357/aaf3b8

Di Matteo, T., Quataert, E., Allen, S. W., Narayan, R., & Fabian, A. C. 2000, , 311, 507, doi: 10.1046/j.1365-8711.2000.03134.x

Di Matteo, T., Springel, V., & Hernquist, L. 2005, , 433, 604, doi: 10.1038/nature03335

Di Teodoro, E. M., & Fraternali, F. 2015, , 451, 3021, doi: 10.1093/mnras/stv1213

Diaz Trigo, M., Carpenter, J., Maude, L., Miura, R., & Plunkett, A. 2019, ALMA Cycle 7 Proposer's Guide, 2019, ALMA Cycle 7 Proposer's Guide, ALMA Doc. 7.2 v1.0 : Proposer's guide for the Atacama Large Millimeter/Submillimeter Array (ALMA) Cycle 7, Doc. 7.2, ver. 1.0, 2019, doi: 10.5281/zenodo.4511962

Dickman, R. L. 1978, , 37, 407, doi: 10.1086/190535

Do, T., Wright, S. A., Barth, A. J., et al. 2014, , 147, 93, doi: 10.1088/0004-6256/147/4/93

Dolag, K., Komatsu, E., & Sunyaev, R. 2016, , 463, 1797, doi: 10.1093/mnras/stw2035

Dubois, Y., Devriendt, J., Slyz, A., & Teyssier, R. 2012, , 420, 2662, doi: 10.1111/j.1365-2966.2011.20236.x

Dubois, Y., Gavazzi, R., Peirani, S., & Silk, J. 2013a, , 433, 3297, doi: 10.1093/mnras/stt997

Dubois, Y., Peirani, S., Pichon, C., et al. 2016, , 463, 3948, doi: 10.1093/mnras/stw2265

Dubois, Y., Pichon, C., Devriendt, J., et al. 2013b, , 428, 2885, doi: 10.1093/mnras/sts224

Dunne, L., Gomez, H. L., da Cunha, E., et al. 2011, , 417, 1510, doi: 10.1111/j.1365-2966.2011.19363.x

Eckart, A., Genzel, R., Ott, T., & Schödel, R. 2002, , 331, 917, doi: 10.1046/j.1365-8711.2002.05237.x

Einstein, A. 1916, Annalen der Physik, 354, 769, doi: 10.1002/andp.19163540702

Ellison, S. L., Patton, D. R., Mendel, J. T., & Scudder, J. M. 2011, , 418, 2043, doi: 10.1111/j.1365-2966.2011.19624.x

Ellison, S. L., Viswanathan, A., Patton, D. R., et al. 2019, , 487, 2491, doi: 10.1093/mnras/stz1431

Escala, A. 2007, , 671, 1264, doi: 10.1086/523092

Event Horizon Telescope Collaboration, Akiyama, K., Alberdi, A., et al. 2019, , 875, L1, doi: 10.3847/2041-8213/ab0ec7

—. 2022, , 930, L12, doi: 10.3847/2041-8213/ac6674

Faber, S. M., & Jackson, R. E. 1976, , 204, 668, doi: 10.1086/154215

Fabian, A. C. 2012, , 50, 455, doi: 10.1146/annurev-astro-081811-125521

Ferrarese, L., & Merritt, D. 2000, , 539, L9, doi: 10.1086/312838

Feruglio, C., Maiolino, R., Piconcelli, E., et al. 2010, , 518, L155, doi: 10.1051/0004-6361/201015164

Finkelstein, D. 1958, Physical Review, 110, 965, doi: 10.1103/PhysRev.110.965

Fluetsch, A., Maiolino, R., Carniani, S., et al. 2019, , 483, 4586, doi: 10.1093/mnras/sty3449

Gallimore, J. F., Baum, S. A., O'Dea, C. P., & Pedlar, A. 1996, , 458, 136, doi: 10.1086/176798

Gallimore, J. F., & Impellizzeri, C. M. V. 2023, , 951, 109, doi: 10.3847/1538-4357/acd846

Gallimore, J. F., Elitzur, M., Maiolino, R., et al. 2016, , 829, L7, doi: 10.3847/2041-8205/829/1/L7

Gámez Rosas, V., Isbell, J. W., Jaffe, W., et al. 2022, , 602, 403, doi: 10.1038/s41586-021-04311-7

García-Burillo, S., Combes, F., Usero, A., et al. 2014, , 567, A125, doi: 10.1051/0004-6361/201423843

García-Burillo, S., Combes, F., Ramos Almeida, C., et al. 2019, , 632, A61, doi: 10.1051/0004-6361/201936606

García-Burillo, S., Alonso-Herrero, A., Ramos Almeida, C., et al. 2021, , 652, A98, doi: 10.1051/0004-6361/202141075

Gaspari, M., Brighenti, F., & Temi, P. 2015, , 579, A62, doi: 10.1051/0004-6361/201526151

Gebhardt, K., Bender, R., Bower, G., et al. 2000, , 539, L13, doi: 10.1086/312840

Gehrels, N., Chincarini, G., Giommi, P., et al. 2004, , 611, 1005, doi: 10.1086/422091

Genel, S., Vogelsberger, M., Springel, V., et al. 2014, , 445, 175, doi: 10.1093/mnras/stu1654

Genzel, R., Eisenhauer, F., & Gillessen, S. 2010, Reviews of Modern Physics, 82, 3121, doi: 10.1103/RevModPhys.82.3121

Ghez, A. M., Morris, M., Becklin, E. E., Tanner, A., & Kremenek, T. 2000, , 407, 349, doi: 10.1038/35030032

Ghez, A. M., Duchêne, G., Matthews, K., et al. 2003, , 586, L127, doi: 10.1086/374804

Ghez, A. M., Salim, S., Weinberg, N. N., et al. 2008, , 689, 1044, doi: 10.1086/592738

Gillessen, S., Eisenhauer, F., Trippe, S., et al. 2009, , 692, 1075, doi: 10.1088/0004-637X/692/2/1075

- Goldsmith, P. F., & Langer, W. D. 1999, , 517, 209, doi: 10.1086/307195
- Goulding, A. D., Greene, J. E., Bezanson, R., et al. 2018, , 70, S37, doi: 10.1093/pasj/psx135
- Greenhill, L. J., & Gwinn, C. R. 1997, , 248, 261, doi: 10.1023/A:1000554317683
- Greenhill, L. J., Gwinn, C. R., Antonucci, R., & Barvainis, R. 1996, , 472, L21, doi: 10.1086/310346
- Greenstein, J. L., & Schmidt, M. 1964, , 140, 1, doi: 10.1086/147889
- Gültekin, K., Richstone, D. O., Gebhardt, K., et al. 2009, , 698, 198, doi: 10.1088/0004-637X/698/1/198
- Gupta, K. K., Ricci, C., Temple, M. J., et al. 2024, , 691, A203, doi: 10.1051/0004-6361/202450567
- Hagiwara, Y., Baan, W. A., Imanishi, M., & Diamond, P. 2024, , 528, 3668, doi: 10.1093/mnras/stae075
- Häring, N., & Rix, H.-W. 2004, , 604, L89, doi: 10.1086/383567
- Heckman, T. M., & Best, P. N. 2014, , 52, 589, doi: 10.1146/annurev-astro-081913-035722
- Herrero-Illana, R., Privon, G. C., Evans, A. S., et al. 2019, , 628, A71, doi: 10.1051/0004-6361/201834088
- Hicks, E. K. S., Davies, R. I., Maciejewski, W., et al. 2013, , 768, 107, doi: 10.1088/0004-637X/768/2/107
- Hinshaw, G., Weiland, J. L., Hill, R. S., et al. 2009, , 180, 225, doi: 10.1088/0067-0049/180/2/225

Hirschmann, M., Dolag, K., Saro, A., et al. 2014, , 442, 2304, doi: 10.1093/mnras/stu1023

Hirschmann, M., Khochfar, S., Burkert, A., et al. 2010, , 407, 1016, doi: 10.1111/j.1365-2966.2010.17006.x

Ho, L. 1999, in Astrophysics and Space Science Library, Vol. 234, Observational Evidence for the Black Holes in the Universe, ed. S. K. Chakrabarti, 157, doi: 10.1007/978-94-011-4750-7_11

Hobbs, A., Power, C., Nayakshin, S., & King, A. R. 2012, , 421, 3443, doi: 10.1111/j.1365-2966.2012.20563.x

Holden, L. R., & Tadhunter, C. N. 2023, , 524, 886, doi: 10.1093/mnras/stad1677

Hopkins, P. F. 2012, , 420, L8, doi: 10.1111/j.1745-3933.2011.01179.x

Hopkins, P. F., Cox, T. J., Kereš, D., & Hernquist, L. 2008a, , 175, 390, doi: 10.1086/524363

Hopkins, P. F., Hernquist, L., Cox, T. J., et al. 2006, , 163, 1, doi: 10.1086/499298

Hopkins, P. F., Hernquist, L., Cox, T. J., & Kereš, D. 2008b, , 175, 356, doi: 10.1086/524362

Hopkins, P. F., & Quataert, E. 2010, , 407, 1529, doi: 10.1111/j.1365-2966.2010.17064.x

—. 2011, , 415, 1027, doi: 10.1111/j.1365-2966.2011.18542.x

Hopkins, P. F., Torrey, P., Faucher-Giguère, C.-A., Quataert, E., & Murray, N. 2016, , 458, 816, doi: 10.1093/mnras/stw289

Hopkins, P. F., Grudic, M. Y., Su, K.-Y., et al. 2024, The Open Journal of Astrophysics, 7, 18, doi: 10.21105/astro.2309.13115

Horne, K., Peterson, B. M., Collier, S. J., & Netzer, H. 2004, , 116, 465, doi: 10.1086/420755

Howarth, I. D. 1983, , 203, 301, doi: 10.1093/mnras/203.2.301

Hoyle, F., & Lyttleton, R. A. 1939, Proceedings of the Cambridge Philosophical Society, 35, 405, doi: 10.1017/S0305004100021150

Hubble, E. P. 1926, , 64, 321, doi: 10.1086/143018

—. 1929, , 69, 103, doi: 10.1086/143167

Hviding, R. E., Hickox, R. C., Väisänen, P., Ramphul, R., & Hainline, K. N. 2023, , 166, 111, doi: 10.3847/1538-3881/ace718

Imanishi, M., Nakanishi, K., Izumi, T., & Wada, K. 2018, , 853, L25, doi: 10.3847/2041-8213/aaa8df

Imanishi, M., Nguyen, D. D., Wada, K., et al. 2020, , 902, 99, doi: 10.3847/1538-4357/abaf50

Jaffe, W., Meisenheimer, K., Röttgering, H. J. A., et al. 2004, , 429, 47, doi: 10.1086/nature02531

Jahnke, K., & Macciò, A. V. 2011, , 734, 92, doi: 10.1088/0004-637X/734/2/92

Kaiser, N. 1986, , 222, 323, doi: 10.1093/mnras/222.2.323

Kawakatu, N., & Wada, K. 2008, , 681, 73, doi: 10.1086/588574

Khan, F. M., Fiacconi, D., Mayer, L., Berczik, P., & Just, A. 2016, , 828, 73, doi: 10.3847/0004-637X/828/2/73

Khandai, N., Di Matteo, T., Croft, R., et al. 2015, , 450, 1349, doi: 10.1093/mnras/stv627

Kocevski, D. D., Faber, S. M., Mozena, M., et al. 2012, , 744, 148, doi: 10.1088/0004-637X/744/2/148

Kormendy, J. 1993, in The Nearest Active Galaxies, ed. J. Beckman, L. Colina, & H. Netzer, 197–218

Kormendy, J., & Gebhardt, K. 2001, in American Institute of Physics Conference Series, Vol. 586, 20th Texas Symposium on relativistic astrophysics, ed. J. C. Wheeler & H. Martel, 363–381, doi: 10.1063/1.1419581

Kormendy, J., & Ho, L. C. 2013, , 51, 511, doi: 10.1146/annurev-astro-082708-101811

Kormendy, J., Bender, R., Magorrian, J., et al. 1997, , 482, L139, doi: 10.1086/310720

Koss, M., Mushotzky, R., Veilleux, S., & Winter, L. 2010, , 716, L125, doi: 10.1088/2041-8205/716/2/L125

Krimm, H. A., Holland, S. T., Corbet, R. H. D., et al. 2013, , 209, 14, doi: 10.1088/0067-0049/209/1/14

Kumar, P. 1999, , 519, 599, doi: 10.1086/307375

Larkin, J., Barczys, M., Krabbe, A., et al. 2006, in Society of Photo-Optical Instrumentation Engineers (SPIE) Conference Series, Vol. 6269, Ground-based and Airborne Instrumentation for Astronomy, ed. I. S. McLean & M. Iye, 62691A, doi: 10.1117/12.672061

Lauer, T. R., Ajhar, E. A., Byun, Y. I., et al. 1995, , 110, 2622, doi: 10.1086/117719

Lin, M.-Y., Davies, R. I., Burtscher, L., et al. 2016, , 458, 1375, doi: 10.1093/mnras/stw401

Lockhart, K. E., Do, T., Larkin, J. E., et al. 2019, , 157, 75, doi: 10.3847/1538-3881/aaf64e

Lodato, G., & Bertin, G. 2003, , 398, 517, doi: 10.1051/0004-6361:20021672

Lutz, D., Sturm, E., Janssen, A., et al. 2020, , 633, A134, doi: 10.1051/0004-6361/201936803

Lyke, J., Do, T., Boehle, A., et al. 2017, OSIRIS Toolbox: OH-Suppressing InfraRed Imaging Spectrograph pipeline, Astrophysics Source Code Library, record ascl:1710.021

Magorrian, J., Tremaine, S., Richstone, D., et al. 1998, , 115, 2285, doi: 10.1086/300353

Marconi, A., & Hunt, L. K. 2003, , 589, L21, doi: 10.1086/375804

Markevitch, M. 1998, , 504, 27, doi: 10.1086/306080

Martins, L. P., Rodríguez-Ardila, A., de Souza, R., & Gruenwald, R. 2010, , 406, 2168, doi: 10.1111/j.1365-2966.2010.17042.x

Matt, G., Guainazzi, M., Frontera, F., et al. 1997, , 325, L13, doi: 10.48550/arXiv.astro-ph/9707065

May, D., & Steiner, J. E. 2017, , 469, 994, doi: 10.1093/mnras/stx886

Mayer, L., Kazantzidis, S., Madau, P., et al. 2007, Science, 316, 1874, doi: 10.1126/science.1141858

McConnell, N. J., & Ma, C.-P. 2013a, , 764, 184, doi: 10.1088/0004-637X/764/2/184

—. 2013b, , 764, 184, doi: 10.1088/0004-637X/764/2/184

McLure, R. J., & Dunlop, J. S. 2002, , 331, 795, doi: 10.1046/j.1365-8711.2002.05236.x

Medling, A. M., Ammons, S. M., Max, C. E., et al. 2011, , 743, 32, doi: 10.1088/0004-637X/743/1/32

Medling, A. M., U, V., Guedes, J., et al. 2014, , 784, 70, doi: 10.1088/0004-637X/784/1/70

Medling, A. M., U, V., Max, C. E., et al. 2015, , 803, 61, doi: 10.1088/0004-637X/803/2/61

Medling, A. M., Privon, G. C., Barcos-Muñoz, L., et al. 2019, , 885, L21, doi: 10.3847/2041-8213/ab4db7

Meenakshi, M., Mukherjee, D., Wagner, A. Y., et al. 2022, , 516, 766, doi: 10.1093/mnras/stac2251

Mercedes-Feliz, J., Anglés-Alcázar, D., Hayward, C. C., et al. 2023, , 524, 3446, doi: 10.1093/mnras/stad2079

Merritt, D., & Ferrarese, L. 2001, , 320, L30, doi: 10.1046/j.1365-8711.2001.04165.x

Mirabel, I. F., & Sanders, D. B. 1988, , 335, 104, doi: 10.1086/166909

Montoya Arroyave, I., Cicone, C., Makroleivaditi, E., et al. 2023, , 673, A13, doi: 10.1051/0004-6361/202245046

Morgan, C. W., Kochanek, C. S., Morgan, N. D., & Falco, E. E. 2010, , 712, 1129, doi: 10.1088/0004-637X/712/2/1129

Morganti, R. 2017, Frontiers in Astronomy and Space Sciences, 4, 42, doi: 10.3389/fspas.2017.00042

Müller Sánchez, F., Davies, R. I., Eisenhauer, F., et al. 2006, , 454, 481, doi: 10.1051/0004-6361:20054387

Müller-Sánchez, F., Prieto, M. A., Hicks, E. K. S., et al. 2011, , 739, 69, doi: 10.1088/0004-637X/739/2/69

Mushotzky, R. F. 1984, Physica Scripta Volume T, 7, 157, doi: 10.1088/0031-8949/1984/T7/036

Mutie, I. M., Williams-Baldwin, D., Beswick, R. J., et al. 2024, , 527, 11756, doi: 10.1093/mnras/stad3864

Negri, A., & Volonteri, M. 2017, , 467, 3475, doi: 10.1093/mnras/stx362

Netzer, H., & Trakhtenbrot, B. 2014, , 438, 672, doi: 10.1093/mnras/stt2238

Ott, T. 2012, QFitsView: FITS file viewer, Astrophysics Source Code Library, record ascl:1210.019

Peng, C. Y. 2007, , 671, 1098, doi: 10.1086/522774

Pihlström, Y. M., Conway, J. E., Booth, R. S., Diamond, P. J., & Polatidis, A. G. 2001, , 377, 413, doi: 10.1051/0004-6361:20011107

Pillepich, A., Springel, V., Nelson, D., et al. 2018a, , 473, 4077, doi: 10.1093/mnras/stx2656

—. 2018b, , 473, 4077, doi: 10.1093/mnras/stx2656

Planck Collaboration, Adam, R., Ade, P. A. R., et al. 2016, , 596, A104, doi: 10.1051/0004-6361/201628522

Porras-Valverde, A. J., Ricarte, A., Natarajan, P., et al. 2025, arXiv e-prints, arXiv:2504.11566, doi: 10.48550/arXiv.2504.11566

Power, C., Nayakshin, S., & King, A. 2011, , 412, 269, doi: 10.1111/j.1365-2966.2010.17901.x

Raban, D., Jaffe, W., Röttgering, H., Meisenheimer, K., & Tristram, K. R. W. 2009, , 394, 1325, doi: 10.1111/j.1365-2966.2009.14439.x

Ricci, C., Bauer, F. E., Treister, E., et al. 2017a, , 468, 1273, doi: 10.1093/mnras/stx173

Ricci, C., Trakhtenbrot, B., Koss, M. J., et al. 2017b, , 233, 17, doi: 10.3847/1538-4365/aa96ad

Rosas-Guevara, Y. M., Bower, R. G., Schaye, J., et al. 2015, , 454, 1038, doi: 10.1093/mnras/stv2056

Rubin, V. C., & Ford, Jr., W. K. 1970, , 159, 379, doi: 10.1086/150317

Saito, T., Takano, S., Harada, N., et al. 2022, , 935, 155, doi: 10.3847/1538-4357/ac80ff

Sakamoto, K., Martín, S., Wilner, D. J., et al. 2021, , 923, 240, doi: 10.3847/1538-4357/ac29bf

Sanders, D. B., & Mirabel, I. F. 1996, , 34, 749, doi: 10.1146/annurev.astro.34.1.749

Sandstrom, K. M., Leroy, A. K., Walter, F., et al. 2013, , 777, 5, doi: 10.1088/0004-637X/777/1/5

Sargent, W. L. W., Young, P. J., Boksenberg, A., et al. 1978, , 221, 731, doi: 10.1086/156077

Schawinski, K., Simmons, B. D., Urry, C. M., Treister, E., & Glikman, E. 2012, , 425, L61, doi: 10.1111/j.1745-3933.2012.01302.x

Schaye, J., Crain, R. A., Bower, R. G., et al. 2015, , 446, 521, doi: 10.1093/mnras/stu2058

Schödel, R., Ott, T., Genzel, R., et al. 2002, , 419, 694, doi: 10.1038/nature01121

Schwarzschild, K. 1916, Abh. Konigl. Preuss. Akad. Wissenschaften Jahre 1906, 92, Berlin, 1907, 1916, 189

Schwarzschild, M. 1979, , 232, 236, doi: 10.1086/157282

Scoville, N., Sheth, K., Walter, F., et al. 2015, , 800, 70, doi: 10.1088/0004-637X/800/1/70

Scoville, N., Sheth, K., Aussel, H., et al. 2016, , 820, 83, doi: 10.3847/0004-637X/820/2/83

Scoville, N. Z., & Solomon, P. M. 1975, , 199, L105, doi: 10.1086/181859

Silk, J. 2013, , 772, 112, doi: 10.1088/0004-637X/772/2/112

Silk, J., & Rees, M. J. 1998, , 331, L1, doi: 10.48550/arXiv.astro-ph/9801013

Solomon, P. M., Scoville, N. Z., Penzias, A. A., Wilson, R. W., & Jefferts, K. B. 1972, , 178, 125, doi: 10.1086/151772

Solomon, P. M., & Vanden Bout, P. A. 2005, , 43, 677, doi: 10.1146/annurev.astro.43.051804.102221

Springel, V., Di Matteo, T., & Hernquist, L. 2005, , 361, 776, doi: 10.1111/j.1365-2966.2005.09238.x

Springel, V., & Hernquist, L. 2005, , 622, L9, doi: 10.1086/429486

Stierwalt, S., Armus, L., Surace, J. A., et al. 2013, , 206, 1, doi: 10.1088/0067-0049/206/1/1

Storchi-Bergmann, T., McGregor, P. J., Riffel, R. A., et al. 2009, , 394, 1148, doi: 10.1111/j.1365-2966.2009.14388.x

Stott, J. P., Hickox, R. C., Edge, A. C., et al. 2012, , 422, 2213, doi: 10.1111/j.1365-2966.2012.20764.x

Taylor, P., & Kobayashi, C. 2015, , 448, 1835, doi: 10.1093/mnras/stv139

Teng, Y.-H., Sandstrom, K. M., Sun, J., et al. 2022, , 925, 72, doi: 10.3847/1538-4357/ac382f

Torrey, P., Vogelsberger, M., Genel, S., et al. 2014, , 438, 1985, doi: 10.1093/mnras/stt2295

Treister, E., Schawinski, K., Urry, C. M., & Simmons, B. D. 2012, , 758, L39, doi: 10.1088/2041-8205/758/2/L39

Tremaine, S., Gebhardt, K., Bender, R., et al. 2002, , 574, 740, doi: 10.1086/341002

Tremmel, M., Karcher, M., Governato, F., et al. 2017, , 470, 1121, doi: 10.1093/mnras/stx1160

Tristram, K. R. W., Burtscher, L., Jaffe, W., et al. 2014, , 563, A82, doi: 10.1051/0004-6361/201322698

U, V., Sanders, D. B., Mazzarella, J. M., et al. 2012, , 203, 9, doi: 10.1088/0067-0049/203/1/9

U, V., Medling, A., Sanders, D., et al. 2013, , 775, 115, doi: 10.1088/0004-637X/775/2/115

U, V., Medling, A. M., Inami, H., et al. 2019, , 871, 166, doi: 10.3847/1538-4357/aaf1c2

U, V., Barth, A. J., Vogler, H. A., et al. 2022, , 925, 52, doi: 10.3847/1538-4357/ac3d26

Valentini, M., Murante, G., Borgani, S., et al. 2020, , 491, 2779, doi: 10.1093/mnras/stz3131

van den Bosch, R. C. E., van de Ven, G., Verolme, E. K., Cappellari, M., & de Zeeuw, P. T. 2008, , 385, 647, doi: 10.1111/j.1365-2966.2008.12874.x

Veilleux, S., Goodrich, R. W., & Hill, G. J. 1997, , 477, 631, doi: 10.1086/303735

Veilleux, S., Meléndez, M., Sturm, E., et al. 2013, , 776, 27, doi: 10.1088/0004-637X/776/1/27

Vestergaard, M., & Peterson, B. M. 2006a, , 641, 689, doi: 10.1086/500572

—. 2006b, , 641, 689, doi: 10.1086/500572

Villforth, C., Hamann, F., Rosario, D. J., et al. 2014, , 439, 3342, doi: 10.1093/mnras/stu173

Viti, S., García-Burillo, S., Fuente, A., et al. 2014, , 570, A28, doi: 10.1051/0004-6361/201424116

Vogelsberger, M., Genel, S., Sijacki, D., et al. 2013, , 436, 3031, doi: 10.1093/mnras/stt1789

Vogelsberger, M., Genel, S., Springel, V., et al. 2014, , 444, 1518, doi: 10.1093/mnras/stu1536

Vollmer, B., Schartmann, M., Burtscher, L., et al. 2018, , 615, A164, doi: 10.1051/0004-6361/201731133

Vollmer, B., Davies, R. I., Gratier, P., et al. 2022, , 665, A102, doi: 10.1051/0004-6361/202141684

Wada, K., Kudoh, Y., & Nagao, T. 2023, , 526, 2717, doi: 10.1093/mnras/stad2918

Wakelam, V., Bron, E., Cazaux, S., et al. 2017, Molecular Astrophysics, 9, 1, doi: 10.1016/j.molap.2017.11.001

Walsh, J. L., Barth, A. J., Ho, L. C., & Sarzi, M. 2013, , 770, 86, doi: 10.1088/0004-637X/770/2/86

Walsh, J. L., van den Bosch, R. C. E., Barth, A. J., & Sarzi, M. 2012, , 753, 79, doi: 10.1088/0004-637X/753/1/79

Walter, F., Neeleman, M., Decarli, R., et al. 2022, , 927, 21, doi: 10.3847/1538-4357/ac49e8

Wang, J., Zhang, Z., & Shi, Y. 2011, , 416, L21, doi: 10.1111/j.1745-3933.2011.01090.x

Weinberger, R., Springel, V., Hernquist, L., et al. 2017, , 465, 3291, doi: 10.1093/mnras/stw2944

Weinberger, R., Springel, V., Pakmor, R., et al. 2018, , 479, 4056, doi: 10.1093/mnras/sty1733

Wetzel, A., Hayward, C. C., Sanderson, R. E., et al. 2023, , 265, 44, doi: 10.3847/1538-4365/acb99a

Williamson, D., Höning, S., & Venanzi, M. 2020, , 897, 26, doi: 10.3847/1538-4357/ab989e

Wilson, A. S., & Ulvestad, J. S. 1983, , 275, 8, doi: 10.1086/161507

Wilson, T. L., Rohlf, K., & Hüttemeister, S. 2013, Tools of Radio Astronomy, doi: 10.1007/978-3-642-39950-3

Wilson, W. J., Schwartz, P. R., Epstein, E. E., et al. 1974, , 191, 357, doi: 10.1086/152974

Wright, E. L. 2006, , 118, 1711, doi: 10.1086/510102

Yoon, I. 2017, , 466, 1987, doi: 10.1093/mnras/stw3171

Young, J. S., & Scoville, N. Z. 1991, , 29, 581, doi: 10.1146/annurev.aa.29.090191.

003053

Appendix A

Considerations for radio imaging

In this appendix, we describe a more detailed version of the decisions made in the imaging process of Chapter 2. Imaging with ALMA data involves converting measurement sets into images by reconstructing a sky model from the visibilities. While the ALMA pipeline typically delivers a well-balanced, coherent image for each measurement set, it creates those images in a manner not necessarily optimal for every observer’s science goal. IRAS F01364–1042 and III Zw 035 together are no exception to this. In this appendix we aim to provide a case study to researchers who may need to consider their own imaging strategies.

This appendix focuses on the usage of the **tclean**, a task in *CASA* (Common Astronomy Software Applications). This task is the workhorse for converting visibilities into usable images. In **tclean**, there is a parameter called *weighting* which when defined as “Briggs” (Briggs 1995) invokes a second parameter, **robust**. In short, adjusting the value of **robust** changes how the baselines in each visibility are weighed inside **tclean**. The effects of changing **robust** on the final image can be significant and somewhat predictable, but each object has its own distribution of gas and thus reacts differently to this change.

In this work presented in Chapter 2, we explore **robust** values from -0.5 to 2 . Generally, the tradeoffs are as follows:

- a) A smaller **robust** value weighs the long baselines higher than the short baselines. This yields a tighter PSF (therefore a higher resolution) image. This approach is best used for studies attempting to probe the smallest of scales with the highest resolution. The downside to this is that sensitivity to diffuse and/or extended emission can be lost.
- b) A larger **robust** value weighs the short baselines higher than the long baselines. This favors high sensitivity, targeting diffuse emission particularly in outer regions of the central source. In doing so, the beam can lose uniformity which increases its FWHM, decreasing the resolution of the image. This approach is best used for studies attempting to detect as much diffuse/extended emission as possible.

Many studies appropriately choose to strike a balance at the default value of 0.5, as the ALMA pipeline provides. Here we outline the impact of changing the **robust** parameter for III Zw 035 and IRAS F01364–1042 and how that impacts our results if using only the TM1 (highest resolution) data for both galaxies. See Section 2.2 for the final observing strategy for IRAS F01364–1042 where we instead combine two measurement sets, which results in a $\sim\sqrt{2}$ lower rms and improves our signal by approximately the same value.

Figure A-1 displays both galaxies imaged with three different **robust** parameters: -0.5 , 0.5 , and 2 . III Zw 035 has a more compact emission profile than IRAS F01364–1042, and so the change between parameter choices is visually less dramatic. When calculating gas mass from CO(2-1) in both of these galaxies, we find results that follow the visual inspection. III Zw 035 ranges from 4.1 to 4.8% (average fraction attributed to gas mass) from -0.5 to 2 . In contrast, IRAS F01364–1042 measures to be from 2.0% to 4.2% over the same range (using TM1 only). The percentage change in gas content is much more dramatic in IRAS F01364–1042 than III Zw 035. As is described in Section 2.3, we concluded that -0.5 was most appropriate for Chapter 2’s analysis. The goal of the study in Chapter 2 is to quantify the amount of

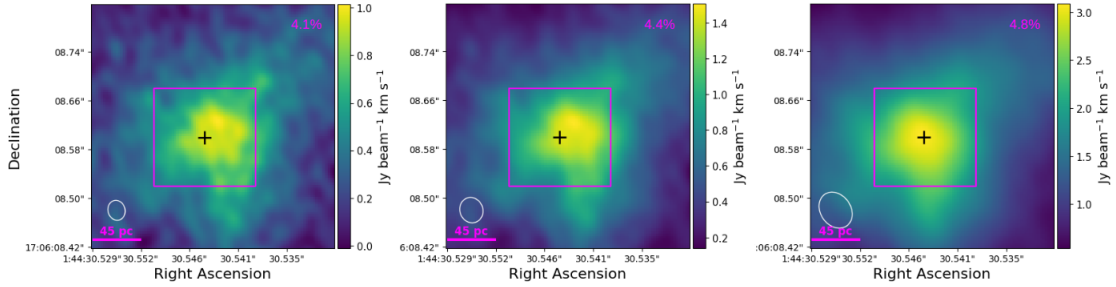


Figure A-1 III Zw 035 CO(2-1) flux as `robust` changes. From left to right these values are -0.5 , 0.5 , and 2 with magenta boxes indicating the Keck resolution-matched apertures used for analysis and magenta numbers describing the % gas mass contribution derived from CO(2-1). We show the respective flux density and mass profiles in Section 2-3. In Chapter 2 we use a `robust` value of -0.5 to minimize contamination from unwanted emission and to maximize resolution. This method results in a lower bound for our estimated gas contribution fractions.

molecular gas mass under the resolution limit of Keck/OSIRIS. Obtaining the highest resolution imaging is key to that. This choice means that diffuse emission in the foreground may be below our detection limits.

Changing the `robust` parameter sometimes has a significant impact on results of data imaged through this process. Therefore we urge future authors to explore different imaging strategies based on their own science goals.

Appendix B

Kinematic Modeling

This section of the Appendix describes additional detail about the ${}^3\text{D}\text{Barolo}$ tilted ring modeling used in this work to calculate enclosed masses from the cold CO gas. ${}^3\text{D}\text{Barolo}$ is a tilted-ring modeling algorithm with a task called **3DFIT**. This algorithm takes in data with kinematic information, and derives rotational velocities for tilted rings spaced at intervals specified by the user. For our purposes with the high resolution CO(2-1) cubes, we use **3DFIT** in two-stage mode. In two-stage mode **3DFIT** regularizes the input parameters, then enters a second fitting phase (Di Teodoro & Fraternali 2015).

We tested different methods of building the **3DFIT** mask (used by the program to determine where there is genuine emission), using both **SEARCH** and **SMOOTH&SEARCH**, and we tested different input parameters (e.g. PA, inclination, redshift, and systemic velocity). In testing, as is suggested by the authors of ${}^3\text{D}\text{Barolo}$, we judge model goodness by examining the line intensity maps and PV plots (as in Figure 2-5). Models and residuals produced in this way are shown in Appendix B, and output tilted ring parameters can be found in Table B.1. In the **3DFIT** task, ${}^3\text{D}\text{Barolo}$ breaks the degeneracy between rotational velocity and velocity dispersion during its spatial convolution step (see Section 2.2 of Di Teodoro & Fraternali 2015). We use the resulting rotational velocities in Section 2.5 to calculate enclosed masses.

Galaxy	R (arcsec)	v _{rot} (km s ⁻¹)	σ_v (km s ⁻¹)
III Zw 035	0.010	117.299 $^{+15.688}_{-16.559}$	12.962 $^{+13.157}_{-13.157}$
	0.030	116.632 $^{+24.541}_{-23.268}$	70.446 $^{+13.758}_{-13.758}$
	0.050	127.537 $^{+17.974}_{-15.995}$	71.341 $^{+13.321}_{-11.454}$
	0.070	138.887 $^{+14.576}_{-13.268}$	64.466 $^{+11.887}_{-9.568}$
	0.090	155.569 $^{+13.731}_{-15.584}$	66.102 $^{+11.342}_{-12.737}$
	0.110	174.523 $^{+20.043}_{-21.25}$	67.762 $^{+14.458}_{-14.458}$
	0.130	184.272 $^{+19.313}_{-19.348}$	58.828 $^{+12.395}_{-12.395}$
	0.150	195.405 $^{+21.794}_{-22.034}$	60.046 $^{+12.700}_{-12.700}$
	0.170	206.447 $^{+24.747}_{-26.912}$	56.457 $^{+12.373}_{-13.456}$
	0.190	210.448 $^{+28.939}_{-26.236}$	44.030 $^{+14.469}_{-13.118}$
IRAS F01364–1042	0.013	158.335 $^{+21.370}_{-17.959}$	30.945 $^{+11.350}_{-11.103}$
	0.039	150.972 $^{+18.810}_{-22.804}$	65.695 $^{+14.215}_{-14.215}$
	0.065	162.998 $^{+13.971}_{-14.571}$	61.799 $^{+9.680}_{-9.638}$
	0.091	173.123 $^{+13.000}_{-12.731}$	62.743 $^{+8.393}_{-8.159}$
	0.117	182.589 $^{+11.929}_{-13.586}$	63.689 $^{+8.303}_{-9.952}$
	0.143	180.143 $^{+15.618}_{-15.427}$	64.256 $^{+10.198}_{-10.775}$
	0.169	168.557 $^{+18.185}_{-18.222}$	61.354 $^{+10.996}_{-11.841}$
	0.195	152.269 $^{+22.261}_{-20.124}$	57.424 $^{+12.634}_{-13.882}$
	0.221	133.305 $^{+23.109}_{-22.004}$	53.216 $^{+11.214}_{-11.214}$
	0.247	137.034 $^{+23.665}_{-26.155}$	45.981 $^{+12.003}_{-12.003}$

Table B.1 ^{3D}Barolo phase two best fit tilted ring model parameters for III Zw 035 and IRAS F01364–1042. The velocity dispersion modeling (column 4) should be taken with caution because of the likely dominance of it by the outflows in these galactic nuclei. The second and third columns, tilted ring radius and rotational velocity, are used to compute enclosed masses as found in Section 2.5.

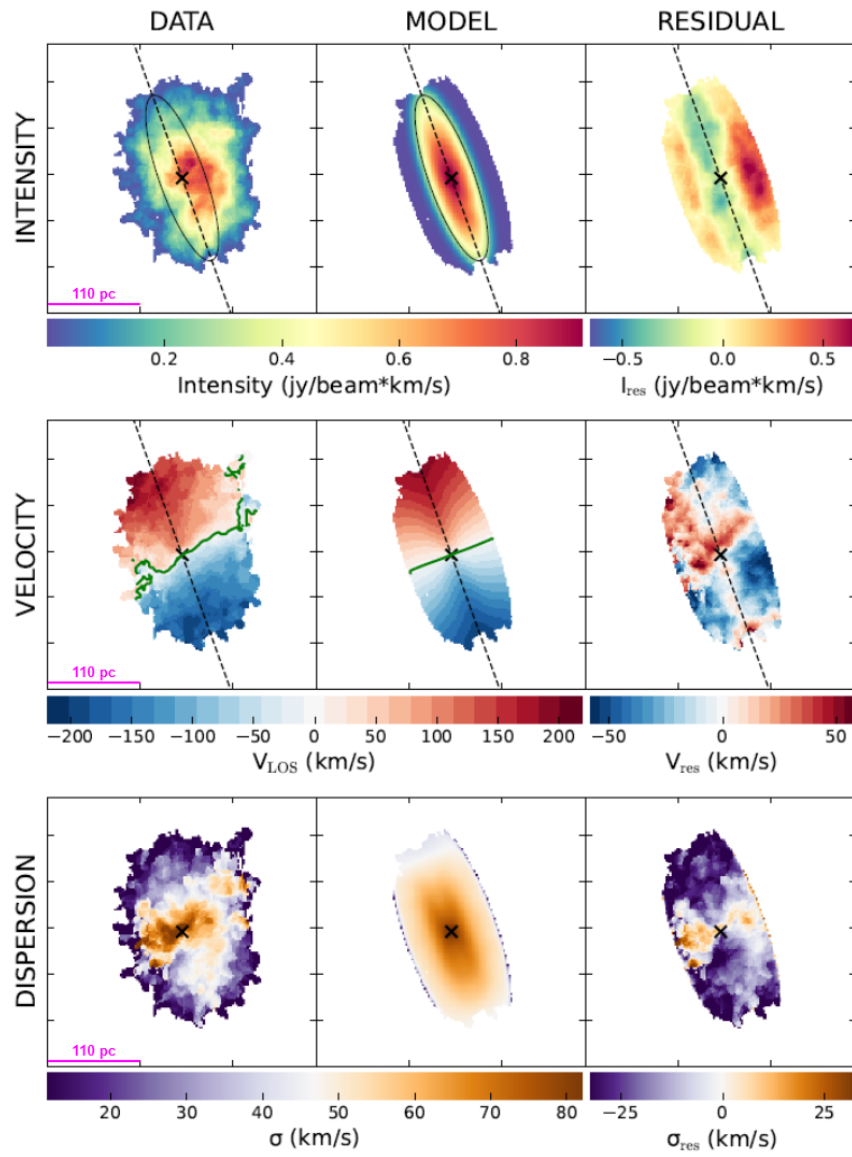


Figure B-1 III Zw 035 ring models produced by ^{3D}Barolo, used to calculate enclosed masses in Section 2.5. Input CO(2-1) images are the same as presented in Figure 2-2 (33 x 28 mas beam size), and input parameters include PA, inclination, redshift, and systemic velocity. Green lines in the first two velocity panels indicate 0 km s^{-1} , which indicate potential disk-warping. III Zw 035's velocity dispersion component is likely dominated by the outflow.

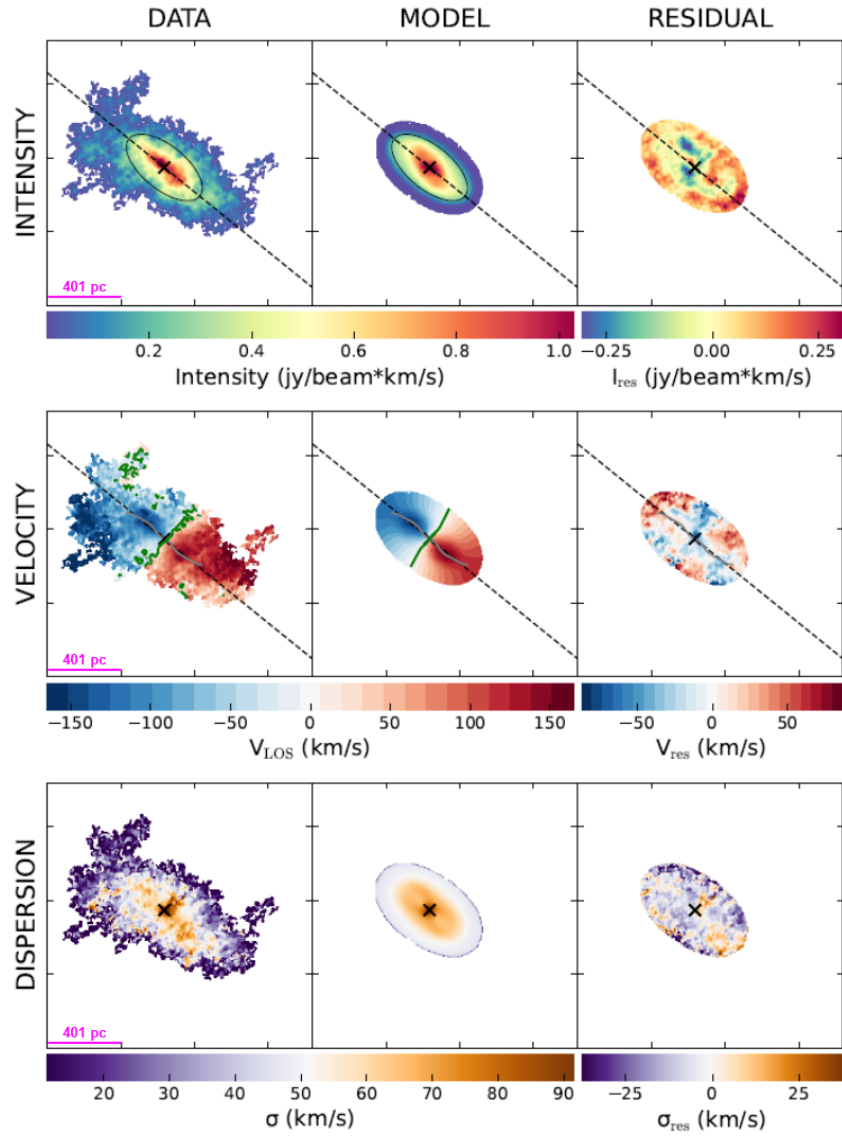


Figure B-2 IRAS F01364–1042 ring models produced by ^{3D}Barolo, used to calculate enclosed masses in Section 2.5. Input CO(2-1) images are the same as presented in Figure 2-2 (42 x 39 mas beam size), and input parameters include PA, inclination, redshift, and systemic velocity. Green lines in the first two velocity panels indicate 0 km s^{-1} . IRAS F01364–1042 is particularly well-defined by a rotating disk, although residuals show some evidence of outflows along the minor axis in velocity space.